ADVANCED PLASMONIC NANOSENSORS FOR THE SERS ULTRADETECTION OF NON-CONVENTIONAL ANALYTES

Tolga Zorlu

UNIVERSITAT ROVIRA i VIRGILI

Advanced Plasmonic Nanosensors for the SERS Ultradetection of Non-Conventional Analytes

TOLGA ZORLU

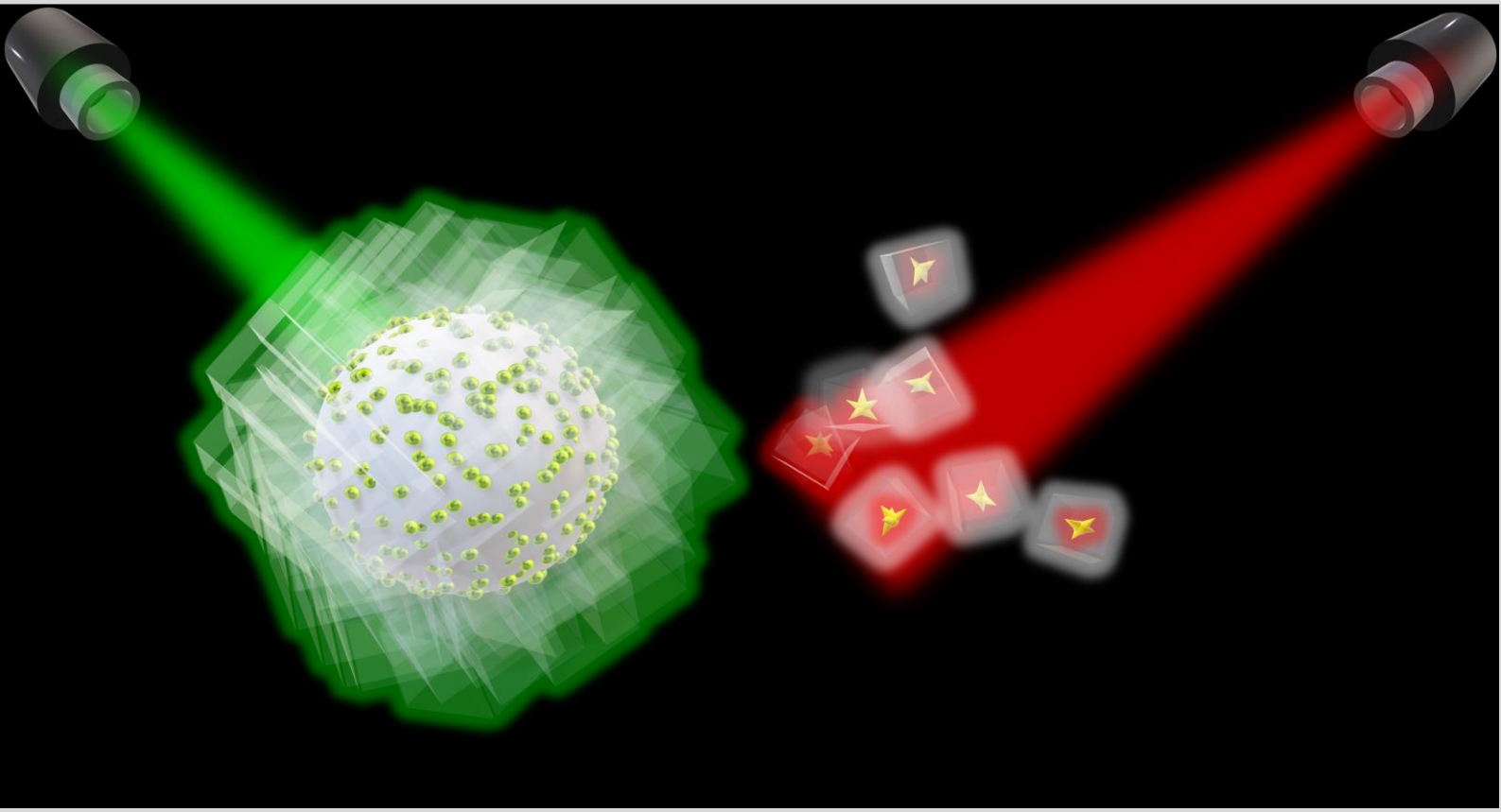

DOCTORAL THESIS
2023

UNIVERSITAT
ROVIRA i VIRGILI

Tolga Zorlu

Advanced Plasmonic Nanosensors for the SERS Ultradetection of Non-Conventional Analytes

Doctoral Thesis

Supervised by

Prof. Ramon Angel Alvarez Puebla

Prof. Miguel Ángel Correa Duarte

Faculty of Chemistry

Department of Physical and Inorganic Chemistry

Tarragona, 2023

UNIVERSITAT
ROVIRA i VIRGILI

FAIG CONSTAR que aquest treball, titulat "ADVANCED PLASMONIC NANOSENSORS FOR THE SERS ULTRADETECTION OF NON-CONVENTIONAL ANALYTES", que presenta Tolga Zorlu per a l'obtenció del títol de Doctor, ha estat realitzat sota la meva direcció al Departament de Química Física i Inorgànica d'aquesta universitat.

HAGO CONSTAR que el presente trabajo, titulado "ADVANCED PLASMONIC NANOSENSORS FOR THE SERS ULTRADETECTION OF NON-CONVENTIONAL ANALYTES", que presenta Tolga Zorlu para la obtención del título de Doctor, ha sido realizado bajo mi dirección en el Departamento Química Física e Inorgánica de esta universidad.

I STATE that the present study, entitled "ADVANCED PLASMONIC NANOSENSORS FOR THE SERS ULTRADETECTION OF NON-CONVENTIONAL ANALYTES", presented by Tolga Zorlu for the award of the degree of Doctor, has been carried out under my supervision at the Department of Physical and Inorganic Chemistry of this university.

Tarragona, 31 de marzo de 2023

El/s director/s de la tesi doctoral
El/los director/es de la tesis doctoral
Doctoral Thesis Supervisor/s

Ramon

Firmado digitalmente por Ramon
Nombre de reconocimiento (DN): cn=Ramon, o=URV, ou, email=ramon.alvarez@urv.cat, c=ES
Fecha: 2023.03.31 11:58:10 +02'00'

Ramon A. Alvarez Puebla

CORREA DUARTE MIGUEL ANGEL - 36103913P

Firmado digitalmente por CORREA DUARTE MIGUEL ANGEL - 36103913P
Fecha: 2023.04.03 22:12:31 +02'00'

Miguel A. Correa Duarte

"God made the bulk; the surface was invented by the devil."

Wolfgang Pauli

Acknowledgements

As I finish this thesis, I would like to thank the people who have always supported me throughout this process. First of all, I would like to thank my thesis advisors Prof. Ramon A. Alvarez-Puebla and Prof. Miguel A. Correa-Duarte for giving me the opportunity to work in their laboratory, trusting me and enabling me to improve myself in the field of plasmonics.

I would like to thank Dr. Nicolas C. Pazos-Perez, Mariacristina, Irene and Brian, dear members of the Zeptonic research group, of which I am proud to be a member, for their sincere friendship and support throughout my doctoral process. I would like to thank Anita, Mai, Andrea, Yoel, Miguel, Lucia, Lucas, Begoña and everyone else from the TeamNanoTech group, which I now consider myself a member of and have done some of my thesis work on. It was an honour for me to be in the same group and work with you. I would also like to thank Prof Verónica Salgueiriño Maceira, the group leader of the Magnetic Materials Group, and her graduate student, Julia for their support. You are not only good scientists, but also great people!

I would like to express my gratitude to Dr. Yasemin Budama-Kılınç and her team at Yıldız Technical University in Turkey, who encouraged and supported me to come to Spain from Turkey, and to my dear friends Dr. Burak Özdemir and Dr. Ahmet Çetinkaya, whose support I felt not only throughout my doctoral process but always.

My dear family. I was separated from you for a while, but thanks to this, I developed myself to the extent I imagined. I apologize to my mother Serap, my father Ahmet, my brother Tayfun and my grandmother Ayten for this price, and I thank them for their endless love and support.

Here, I would like to thank my dear girlfriend, friend, family member and colleague Dr Ecem Tiryaki, who is of great value to me and deserves a special paragraph, for changing my life, beautifying it and making me a better person and scientist. I love you.

Table of Contents

Chapter Three

Chapter Four

LIST OF ABBREVATIONS

Å: Angstrom

^{o}C: Celsius

µg: Microgram

µL: Microliter

1-NAT: 1-Naphthalenethiol

2-MHQ: 2-Methoxyhydroquinone

4-MBT: 4-Methylbenzenethiol

ABT: 4-Aminobenzenethiol

ADI: Adiponitrile

$AgNO_3$: Silver nitrate

AgCl: Silver chloride

$AuCl_3$: Gold(III) chloride

B3LYP: 3-Parameter hybrid Becke exchange/ Lee–Yang–Parr correlation functional

BDAC: Benzyldimethylhexadecylammonium chloride

BET: Brunauer-Emmett-Teller

BEM: Boundary element method

BJH: Barrett-Joyner-Halenda

BT: Benzenethiol

CD44: Cell surface adhesion receptor

CEES: 2-Chloroethyl ethyl sulfide

CTAB: Cetyltrimethylammonium bromide

CTAC: Cetyltrimethylammonium chloride

CV: Crystal violate

DBTDT: Dibenzo[*d*,*d*']thieno[3,2-*b*;4,5-*b'*]dithio-phene

DDT: Dichlorodiphenyltrichloroethane

DEHP: Di-(2-ethylhexyl) phthalate

DFT: Density functional theory

DMAB: 4,4-Dimercaptoazobenzene

DMEM: Dulbecco's modified eagle medium

DMF: Dimethylformamide

DMMP: Dimethyl methylphosphonate

DMSO: Dimethyl sulfoxide

DOX: Doxorubicin

EDX: Energy dispersive x-ray analysis

EGFR: Epidermal growth factor receptor

FAAS: Flame Atomic Absorption Spectrometry

FDTD: Finite difference time domain method

Fe_2O_3: Ferric oxide

Fe_3O_4: Iron oxide

FTO: Fluorine-doped Tin Oxide

GLU: Glutaronitrile

GPa: Gigapascal

H_2O_2: Hydrogen peroxide

H_4TBAPy: 1,3,5,8-(*p*-benzoate)pyrene

$HAuCl_4$: Chloroauric acid

HCH: Hexachlorocyclohexane

HMDA: Hexamethylene-1,6-diamine

HOMO: Highest occupied molecular orbital

HRTEM: High-resolution transmission electron microscopy

IMDM: Iscove's modified Dulbecco's medium

ICP: Inductively Coupled Plasma

ICP-MS: Inductively Coupled Plasma Mass Spectrometry

IUPAC: International union of pure and applied chemistry

KCl: Potassium chloride

L-15: Leibovitz's L-15 Medium

LUMO: Lowest unoccupied molecular orbital

MBA: 4-Mercaptobenzoic acid

MeIQ: 2-Amino-3,4-dimethyl-3H-imidazolequinoline

MEM: Minimal essential medium

MG: Malachite green

$MgSO_4$: Magnesium sulphate

MUTAB: 11-mercaptoundecyltrimethylammonium bromide

Na_2HPO_4: Sodium phosphate dibasic

NaBr: Sodium bromide

NaCl: Sodium chloride

NaH_2PO_4: Sodium phosphate monobasic

NaOH: Sodium hydroxide

NAT: 2-Naphthalenethiol

NC: Nanocube

ng: Nanogram

$Ni(CN_4)$: Tetracyanidonickelate

NR: Nanorod

NS: Nanostar

NW: Nanowire

PAH: Poly(allylamine hydrochloride)

PANI: Polyaniline

PDDA: Poly(diallyldimethylammonium chloride)

PEG: Polyethylene glycol

PEI: Polyethyleneimine

PLL: Poly(*L*-lysine)

PMAA: Poly(methacrylic acid)

ppb: Parts per billion

ppm: Parts per million

PS: Polystyrene

PSS: Poly(sodium sulfonate)

PVP: Polyvinylpyrrolidone

PXRD: Powder X-Ray Diffraction

RPMI-1640: Roswell Park Memorial Institute-1640

QD: Quantum dot

R6G: Rhodamine 6G

RhB: Rhodamine B

SDS: Sodium dodecyl sulfate

SEM: Scanning electron microscopy

SERES: Surface-enhanced Raman excitation spectroscopy

STAC: Trimethylstearylammonium chloride

SUC: Succinonitrile

TEA: Triethanolamine

TEM: Transmission electron microscopy

TGA: Thermogravimetric analysis

TiO_2: Titanium dioxide

TPABr: Tetrapropyl-ammonium bromide

TRIS: Tris(hydroxymethyl)aminomethane

TTC: Tetracycline

UV: Ultraviolet

XRD: X-Ray Diffraction

Thesis Scope

Plasmonic nanoparticles such as gold and silver have found a place in many different application areas due to their unique physical and electrical properties. The most well-known of these areas is surface-enhanced Raman spectroscopy (SERS), which allows detection at the single-molecule level.

SERS is a spectroscopy technique, basically, based on the observations of Raman and Krishnan nearly a century ago and derived from the phenomena they presented. In its simplest form, it aims to use of plasmonic materials such as gold and silver, and increase the Raman signals or with another word, their molecular fingerprints, which are formed because of photons scattering inelastically as a result of the interaction of molecules with light. In this way, the technique has gained a popularity in different fields from environmental monitoring to sensing of biological molecules or metal ions. The raw material of SERS is the SERS substrates specially produced for this technique. These substrates can be composed of the simplest spherical plasmonic nanoparticles or one of the most complex cases, plasmonic composites obtained by combining different materials. However, the goal is always the same: to reveal the most powerful and problem-solving substrate for the SERS technique.

Bearing this in mind, the aim of this PhD thesis is to produce strong and functional composite SERS substrates for different purposes. For this, SERS-based functionality of composites resulting from the integration of zeolitic imidazolate frameworks (ZIFs) into plasmonic particles and their plasmonic natures were investigated. ZIFs are typical porous materials and are one of the sub-groups of the metal-organic frameworks (MOFs) that have attracted much attention over the last two decades and are being studied by a new sub-branch called reticular chemistry. Besides, it is one of the ideal MOFs to be easily integrated into composites produced for thesis studies, thereby revealing more sophisticated SERS substrates.

The thesis consists of 4 chapters. Chapter one starts with a brief about the basic nanotechnology concept and continues with information about plasmonic nanoparticles and their nature. In the content of this thesis, gold, and silver nanoparticles are mentioned, and it is shown how they are obtained in different morphologies with the seed-mediated growth approach which is used for the experiments in the thesis. Subsequently, the definition and mechanism of SERS, and the factors affecting SERS signal quality are defined. Then, plasmonic

substrates that can be used for various SERS applications are mentioned. In this context, an overview of MOFs has been taken, and their properties are examined. Among these MOFs, the properties of ZIFs, and the composites arising from their association with Au and Ag NPs which are the subject of the thesis, are specifically mentioned, and with SERS applications of these plasmonic-ZIF-8 nanocomposites are concluded in chapter one.

Chapter two describes a method for the preparation of yolk-shell SERS sensors consisting in a star-shape plasmonic gold nanoparticles coated with ZIF-8. This configuration shows more colloidal stability, can sieve different molecules based on their size or charge, seems to show some interesting synergy with gold for their application in photocatalysis and present strong optical activity to be used as SERS sensors.

Chapter three is design and synthesis of a hybrid material comprising polystyrene sub-microbeads coated with Ag nanospheres. This material provides a dense collection of electromagnetic hotspots upon illumination with visible light. The subsequent coating with a ZIF-8, and the adsorption of bathocuproine on it yields an optical sensor for SERS that can detect specifically Cu(II) in a variety of aqueous samples at the ultra-trace level. Detection limits with this method are superior to those of inducted coupled plasma or atomic absorption and comparable with those obtained with inducted coupled plasma coupled with a mass detector. Finally, Chapter four provides general conclusions about thesis.

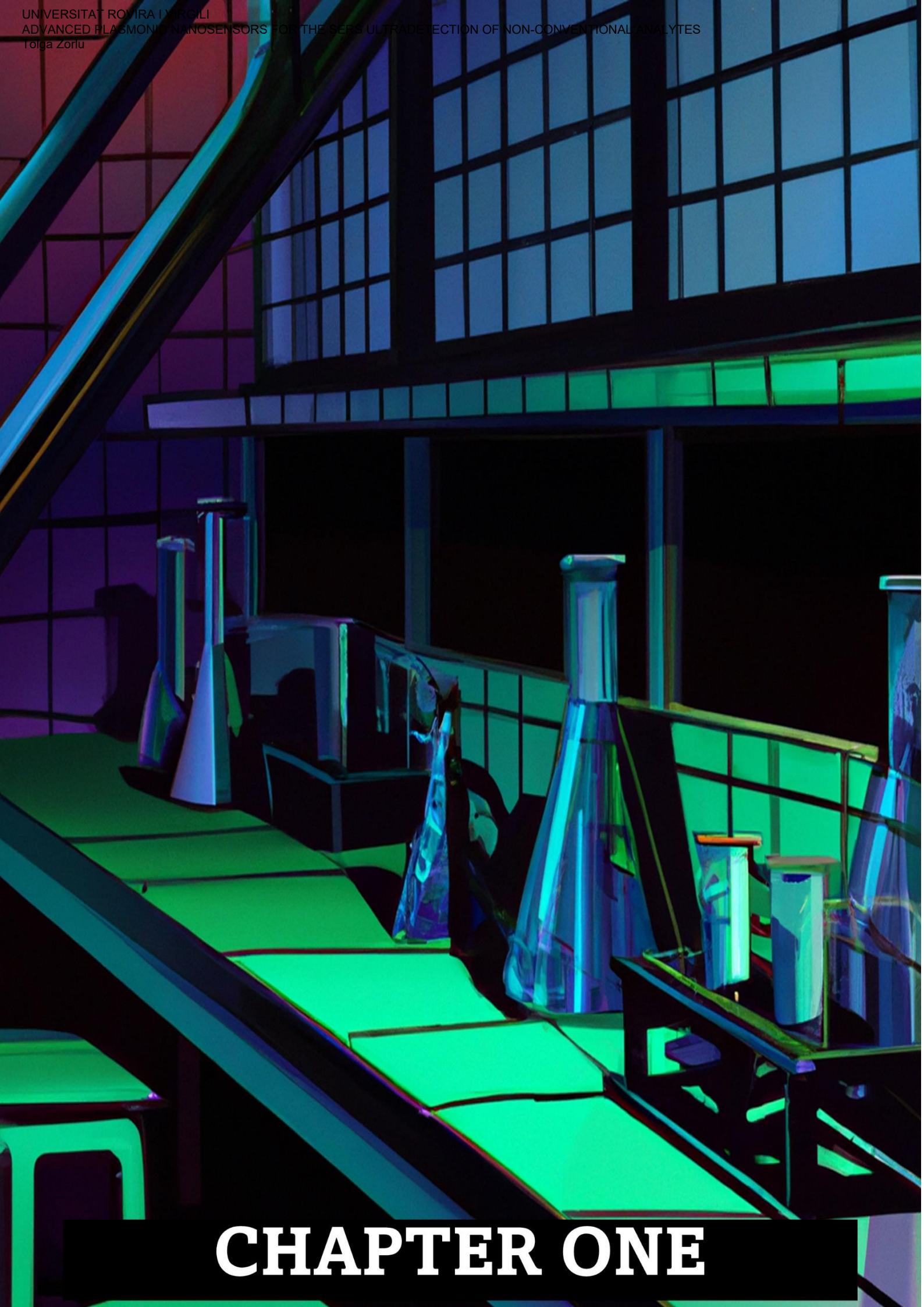

CHAPTER ONE

1.1. Nanotechnology

1.1.1. Definition

Nanotechnology is the branch of science that marked the past century and is one of the biggest building blocks of the incredible technological progress we have today. According to the report published by the European Commission in 2006, nanotechnology is defined as "*the design, characterization, production and application of structures, devices and systems by controlling shape and size at the nanoscale*" [1]. In simpler terms, nanotechnology examines the production and manipulation of any material at the nano-level, and the concept was unofficially emerged in December 1959 with a speech by the famous physicist Richard Feynman at the American Physical Society annual meeting [2]. In the meeting, Feynman asked the participants a question such as "*What would happen if we could arrange each atom individually*" and predicted that the production and manipulation of material at the nano-level would be possible. Although it seemed more like science-fictional at that time, today it has become the reality and ordinary to produce nanotechnological masterpieces that take their power from different backgrounds such as engineering, mathematics, physics, and chemistry, and examined them in many different fields. Thereby, numerous commercial products we use in the market, or their contents consist of organic or inorganic nanotechnological materials [3-5]. Undoubtedly, One of the best examples that can be given in this regard is that most of the nanotechnological devices developed during the 2019 coronavirus disease (COVID-19) pandemic, and the kits produced for easy detection of the virus are based on the concept of nanotechnology [6, 7]. Although one of the frequently used areas of nanotechnology is in medical applications, it has also found a place in different fields such as military technology [8], solutions for environmental pollution [9], and space exploration [10].

The word *nano* is derived from a Greek word "*Nanos*" meaning "*dwarf*". One nanometer is expressed in "*nm*" and is equal to one billionth of a meter (10^{-9} m). The materials with dimensions in this scale are classified as "*nanoparticles (NPs)*". Generally, the materials between 1 and 100 nm are being categorised in this class. On the other hand, the materials which are larger than 100 nm are called "*microparticles (MPs)*" with different expressions. The reason is that the large number of atoms at the edges of the material below 100 nm causes the surface area of NPs to expand compared to MPs. Apart from that, the size also contributes

to changes in the properties of the material, so nano and micro forms of the same material tend to show different properties from each other. Figure 1.1 shows the nano-level, and their comparison of surface/volume ratios with micro or macro materials.

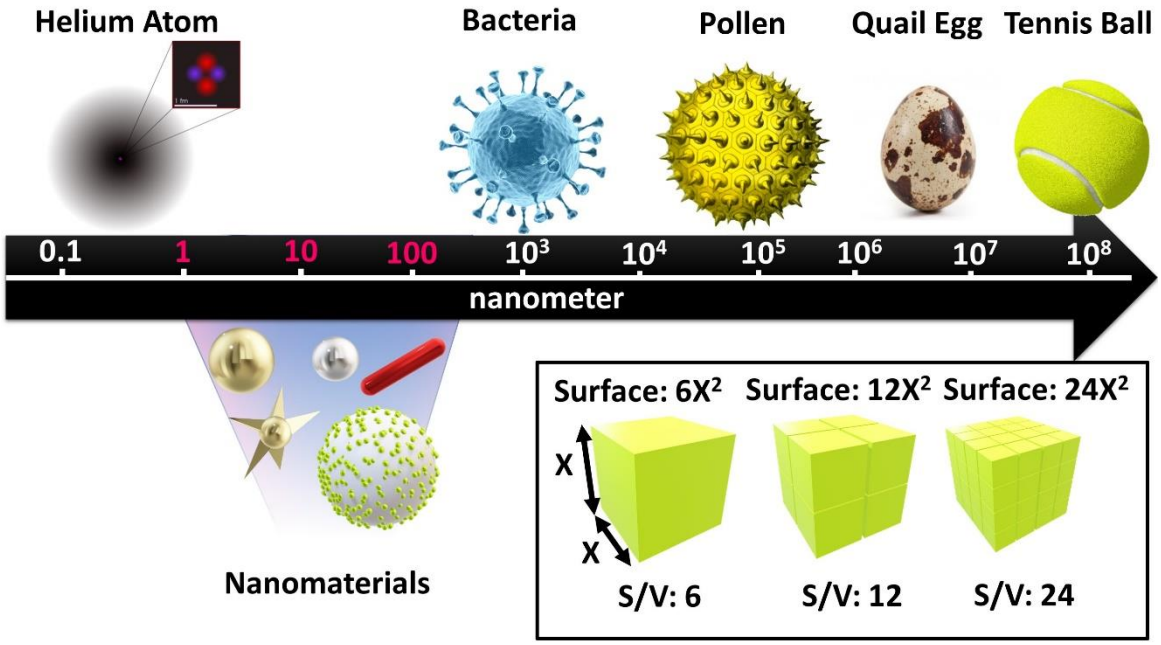

Figure 1.1. *Schematic representation of nano-level and changing of surface/volume parameters from micro to nano dimension.*

The production of materials with such small dimensions is not only very difficult but also requires the collaboration from different branches of science. As a result, the materials of both organic and inorganic origin that serve multidisciplinary purposes have been successfully introduced. When we take a look at the NPs from an organic point of view, we notice to usage of synthetic or natural polymeric NPs, such as liposomes, micelles, dendrimers, etc. These kinds of NPs are generally accepted as *free* of their toxic nature, and more susceptible to medical and pharmaceutical applications such as drug delivery [11-13]. The fact is that these particles are mostly used as coating agents in medical research, their surfaces are easily functionalized, adverse effects of them are very low, or they can be eliminated from the body as desired to make them *ideal carrier* NPs for the most of drug. On the other hand, inorganic NPs are also preferred due to their unique ability to be used in the medical field, as well as their predisposition to more physical and chemical applications. For instance, magnetic materials such as bare Fe_3O_4 and Fe_2O_3 NPs are widely used in different disciplines, from medical to

environmental applications, due to their strong magnetic properties [14, 15]. On the other hand, TiO_2 NPs, one of the another kind of metallic NPs, have been also frequently preferred in antibacterial and paint products, and mainly can be used in catalysis studies [16, 17]. In fact, most metallic elements and some lanthanides in the periodic table can find a place for different applications thanks to their different physical and chemical properties. Moreover, each metallic or organic compound can have stronger properties and wide usage areas not only by itself but also by preparing as metal-metal or metal-organic composites. Among metallic NPs, the ones with noble metal origins such as gold, silver or copper, which are called "*plasmonic NPs*", are very attractive metals for different chemical or biological applications and can be used alone or in composite forms in various studies.

1.1.2. Plasmonic Nanoparticles

Throughout human history, brightly coloured metals have attracted people. For this reason, noble metals such as palladium, silver, platinum, and gold, which are rare in nature, have fascinated people at every moment of history due to their properties since the first age, and that's why, they are still used as both valuable ornaments and universal commercial tools. Among these noble metals, gold has always been regarded as an indicator of power, sovereignty, and wealth. Likewise, it is known that silver, another noble metal, has been used as money from early times. Both types of metals have been deified in ancient and modern cultures for different reasons, such as being easy to be worked with or symbols of power.

Gold is a transition metal which has an atomic number of 79, a melting point of about 1063°C, and a boiling point of about 2855°C. It is represented by the symbol *Au*. In general, it is distributed in rocks throughout a large part of the world but is found in very low concentrations. Therefore, it is a difficult process to find and obtain. Its amount in the earth's crust was estimated to be about from 0.001 to 0.006 ppm [18]. It is mostly found in its natural form, but it can also be in mineral form with elements such as tellurium, silver, lead, sulphur, copper, and bismuth. There are two major oxidation states, +1 and +3. The +1-oxidation state is quite unstable, while the +3 state is stable. For this reason, two basic gold compounds such as $AuCl_3$ or $HAuCl_4$, which have a +3-oxidation state in general, are preferred in chemical studies. Although it is mostly preferred as an ornamental item due to its brightness, it finds a place for itself in different fields from electronics [19] to medical industry [20, 21]. On the other hand, silver is also a precious metal with an atomic number of 47, a melting point of about

1588°C, and a boiling point of about 3740°C. It is denoted by the symbol *Ag*. Just like gold, it is quite shiny and relatively soft. For this reason, silver metal is preferred not only as jewellery and ornaments, but also in mirrors because it reflects light well [22], in various surgical instruments due to its antibacterial properties [23], and in electronic instruments and batteries due to its conductivity [24]. The +1 and +2-oxidation states are most frequently encountered in nature, and argentite is one of the most important mineral forms of silver.

In its shortest definition, plasmonics is a science that study with "*plasmons*" [25]. According to this, a plasmon can be described as collective oscillations of free electrons in metals. When a surface of the metal such as gold or silver, is excited by the light of a certain wavelength, the free electrons on the surface exhibit resonant oscillation. As a result, "*surface plasmons (SPs)*", which are the interaction between free electrons and the electromagnetic field, are observed. These SPs can propagate in a wave-like manner along an interface between a metal and a dielectric. This phenomenon is known as "*surface plasmon polaritons (SPPs)*" [26]. SPPs can continue to propagate across the metal surface until the energy is dissipated into free space by heat loss or radiation. The resonant oscillation of conduction electrons at an interface between the negative and positive permittivity material is called "surface plasmon resonance (SPR)" [27] and according to Drude's model (1900), the equilibrium for plasmon frequency (ωρ) for macroscopic metals is given by the relation:

$$\omega_\rho^2 = {ne^2}/{\varepsilon_0 m} \tag{1.1}$$

Where *n* is the number density of mobile charge carriers, *e* their charge, *m* their mass, and ε_0 the relative permittivity of free space. For most metals, the ω_ρ value is in the UV regime with the Fermi energies within 5-15 eV (5.53 eV for Au, and 5.517 eV for Ag) depending on the metal band structure. It is also important that the collective oscillation of the free electrons is not infinite and has to be relaxed by time. The relaxation time (or collision time) for plasmonic metals (τ) is closely related to the electrical conductivity (σ) of the given metal:

$$\sigma = {ne^2\tau}/{m} \tag{1.2}$$

From this point of view, relaxation time can be calculated as:

$$\tau = {\sigma m}/{ne^2} \tag{1.3}$$

These relaxation times are, generally, equal to 31±12 x 10^{-15} s for Ag and 9.3±0.9 x 10^{-15} s for Au at room temperature [28]. With the relaxation time, it is possible to calculate what frequency (γ) the collective oscillation will be relaxed by electronic collision ($1/\tau$):

$$\gamma = 1/\tau \tag{1.4}$$

Here, according to the theory, γ is accepted as the parameter from a single source. However, in reality, the electronic collision that defines the γ parameter is known to come from three different main sources. Accordingly, it may be rewritten **eq. 1.4** as follows:

$$1/\tau = 1/\tau_{ee} + 1/\tau_{ep} + 1/\tau_{i} \tag{1.5}$$

Where $1/\tau_{ee}$ is collisions between electrons, $1/\tau_{ep}$ is collisions between electrons and phonons, and $1/\tau_{i}$ is collisions between electrons and impurities.

Another parameter, Drude's relaxation rate (Γ), for macroscopic plasmonic materials can be calculated as:

$$\Gamma = h\tau^{-1} \tag{1.6}$$

Where h is Planck's constant and τ is the specific relaxation time for the given material. Although Ag has a lower electron relaxation rate than Au, Au is widely used in many optical applications due to the poor long-term stability and oxidation problem of Ag [29].

For the plasmonic NPs, their optical properties have been well-studied in many different studies because of the interesting characteristics which are different from their bulk counterparts, and specific application areas [30-32]. Generally, nanoparticular forms of spherical Au and Ag are responsible for emerging red and yellow colours, respectively. Their bright colours and optical properties have been of interest for centuries, and today, we know that scientific studies of plasmonic NPs date back to the experiments of Michael Faraday [33].

Au NPs and Ag NPs are defined as "*plasmonic NPs*" due to these materials having very special SPs called "*localized surface plasmons (LSPs)*". In the case of plasmonic NPs, LSPs are not-propagating excitations, and because of this reason, plasmon oscillation is distributed over the whole particle volume [34]. If the size of macroscopic plasmonic materials is reduced to nanoscale form, when the light hits the surface of these NPs, a high electromagnetic field which is called "*localized surface plasmon resonance (LSPR)*" is observed near and in certain regions

of the surface [35]. In this case, while the electrons on the surface of a plasmonic NP are freely moving, they are forced to be oriented and periodically displaced due to the electric field of an external light stimulus. The displacement event results in charges at opposite sides of the particle. As a result, LSPs appear, the frequency of which is determined by the restoring force and the mass of the electron [36]. The key difference between SPR and LSPR is in the length scale for the plasmonic materials [37]. LSPR can be considered as a particular type of SPR, and dimensions of plasmonic NPs are significantly smaller than wavelength of light (Figure 1.2).

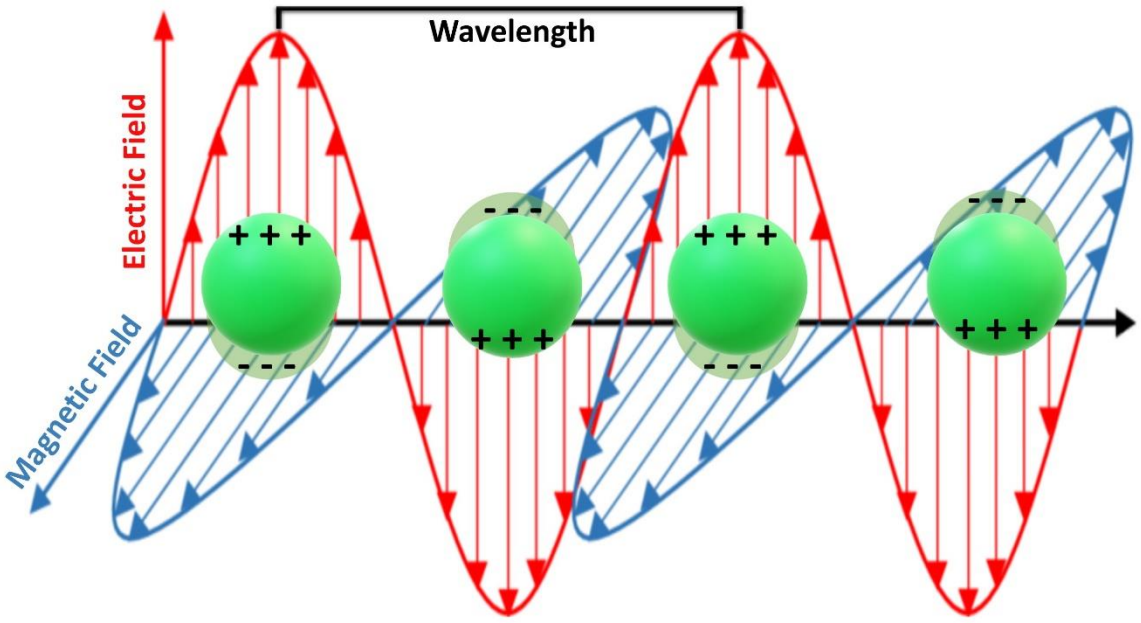

Figure 1.2. *Schematic illustration of the interaction of electromagnetic radiation with a spherical plasmonic NP.*

Collective oscillation of the electrons in plasmonic NPs causes to appear optical extinction cross-sections (σ_{ext}):

$$\sigma_{ext} = \sigma_{scat} + \sigma_{abs} \tag{1.7}$$

Here, when the light comes to the surface of a plasmonic NP, the material scatters it in different directions but at the same frequency as it came from. This situation is defined as scattering cross-section (σ_{scat})[38]. On the other hand, oscillating electrons lose some of their energy as a form of heat because of the fact that plasmonic NPs are not perfect conductors [39], and absorption cross-section (σ_{abs}) has to be put into the equation above. In this way, σ_{ext} of plasmonic NPs can be calculated with contributions of both σ_{scat} and σ_{abs}. The concept of σ_{ext}

is strongly dependent on the dipole which is resulting from electron oscillations of plasmonic NPs. On the other hand, the dipole is controlled by different factors such as the size, shape, or composition of the NPs. Consequently, different extinction spectra can be observed (Figure 1.3).

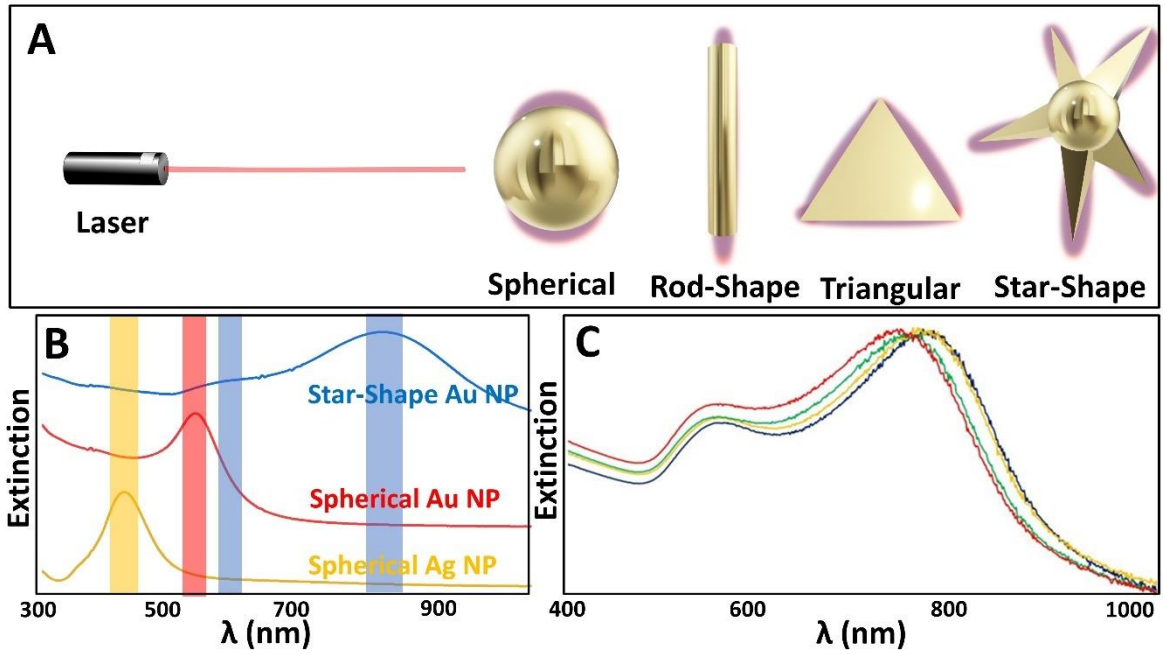

Figure 1.3. *Representation of changing of LSPR position on plasmonic NPs. (**A**) When plasmonic NPs have different morphologies are excited with a focused laser, different plasmon modes can be occurred. (**B**) LSPR band position may vary in NPs of the same composition but different morphology, or NPs with the same morphology but different composition. (**C**) Even little changings in the morphology cause huge alterations in LSPR position. In here, the changes in LSPR position are given for star-shape Au NPs with different tip lengths.*

The Refractive index of a plasmonic nanomaterial is an essential parameter to determine the properties of given material [40] and is directly related to the permittivity of the material (ε) which is given by the relation:

$$\varepsilon(\boldsymbol{K},\omega) = 1 + {}^{i\sigma(\boldsymbol{K},\omega)}/_{\varepsilon_0\omega} \qquad (1.8)$$

Where $\boldsymbol{K}$ is the wave vector and, ω is *the* radial frequency of incident light. Because the dimensions of plasmonic NPs are smaller than the wavelength of the incident light, $\boldsymbol{K}$ may describe as $\mathbf{0}$, and dielectric function (DF) can be simplified as $\varepsilon(\mathbf{K} = \mathbf{0}, \omega) = \varepsilon(\omega)$. In this way,

for non-transparent materials such as metals, DF is a complex-valued function of ω and can be given by the relation:

$$\varepsilon(\omega) = \varepsilon_1(\omega) + i\varepsilon_2(\omega) \quad (1.9)$$

Here, the function has real and imaginary parts as $\varepsilon_1(\omega)$ and $\varepsilon_2(\omega)$, respectively. In addition, where *i* is described as an imaginary constant and given by √(-1). The real part of the function is related to polarization and the imaginary part of the function, on the other hand, determines the amount of absorption inside the medium [41].

Gustav Mie was the first scientist to calculate the concept of the optical cross-section for plasmonic NPs with spherical morphology in the early 1900s. The theory, known today as the "*Mie theory*", was put forward based on Maxwell's equations of electromagnetism, the permittivity of NPs and their surrounding medium:

$$\sigma_{ext} = {}^{2\pi}/_{|\boldsymbol{K}|^2} \sum_{l=1}^{\infty} (2l+1)(a_l + b_l) \quad (1.10)$$

$$\sigma_{scat} = {}^{2\pi}/_{|\boldsymbol{K}|^2} \sum_{l=1}^{\infty} (2l+1)(|a_l|^2 + |b_l|^2) \quad (1.11)$$

Here, $\boldsymbol{K}$ is the wave vector and *l* is a number and is associated with dipole (*l* = 1), quadrupole (*l* = 2), octupole (*l* = 3), and so on. a_l and b_l are the part which includes Bessel and Hankel functions, the radius of the given plasmonic NP, and the permittivity of the given NP. According to the dipolar estimates σ_{scat} and σ_{abs} can be given as:

$$\sigma_{scat} = {}^{32\pi^4 R^6 \varepsilon_m^2}/_{\lambda^4} \left| {}^{\varepsilon - \varepsilon_m}/_{\varepsilon + 2\varepsilon_m} \right|^2 \quad (1.12)$$

$$\sigma_{abs} = {}^{24\pi^2 R^3 \varepsilon_m^{3/2}}/_{\lambda} \; {}^{\varepsilon_i}/_{|\varepsilon + 2\varepsilon_m|^2} \quad (1.13)$$

Where *R* is the radius of the given NP, and ε_m is the permittivity of the surrounding medium. For plasmonic NPs with very small dimensions, extinction equals absorption and therefore, scattering can be neglected. On the other hand, as the composition or size of the spherical NPs changes, the resulting σ_{abs} and σ_{scat} will also differ from each other (Figure 1.4).

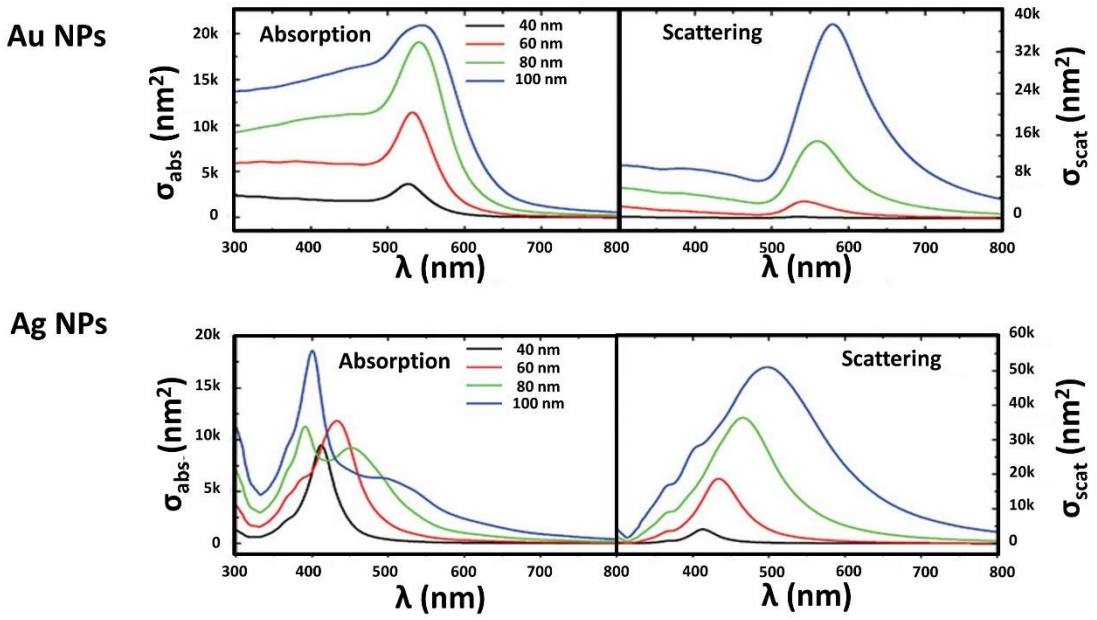

Figure 1.4. Absorption and scattering cross sections of Au and Ag NPs in water with diameter of 40, 60, 80, and 100 nm. Adapted with permission from ref. [39]. Copyright 2020, John Wiley and Sons.

1.1.3. Synthesis of Plasmonic Nanoparticles

All changes in the size, morphology, or composition of plasmonic NPs cause differences in the optical properties of these materials as described above. In this way, plasmonic nanomaterials which are specific to different applications can be designed. For instance, in a plasmonic NP of the same composition but different sizes the position of the LSPR band will be differed. Likewise, different LSPR widths or positioning due to morphology will also be observed even if the composition and size are the same. This is a very important factor for some applications, especially for surface-enhanced spectroscopy techniques [42]. Today, although various synthesis approaches such as laser ablation, ultrasound- and microwave-assisted, or biological approaches have been developed for plasmonic NPs of different morphologies and compositions, synthesis and size growth approaches can be grouped into three basic categories: **(1)** wet chemistry, **(2)** LaMer growth [43], and **(3)** aggregative growth [44].

Wet chemistry is the most general method in NP synthesis. Accordingly, the metal precursors are reduced in the presence of a reducing agent in the solution, and the particle nucleation stage begins. The size of the particles can be controlled by various stabilizing agents,

also called *surfactants*. These formed NPs can also be used as *seeds* to obtain NPs with different morphologies in the next stages. In the LaMer growth approach, a heterogeneous nucleation process is observed on the seed surface. In this way, in addition to size, morphological diversification of NPs can be achieved through various shape-directing agents. On the other hand, in the aggregative growth approach, the seeds formed as a result of nucleation *fuse* with each other to reach NPs of larger sizes. If this fusion process can be implemented in a controlled manner, monodisperse NP assemblies can be obtained.

When we look the scientific publications up in which Au NPs were produced synthetically for the first time, we come across Michael Faraday's publication in 1857 [33]. In this work, which examines the relationship between light and matter, Faraday was trying to make Au sheets close to transparent. For this, he was performing to turn the golden leaves into thin sheets by hammering. However, because he thought that the thicknesses of the sheets were not enough, he decided to try a chemical treatment with a phosphorus-based reducing agent. In this way, he saw that the fluid obtained was of ruby red colour, and after continuing to use this fluid in his studies, he noted that "*illuminated particles were identified in this fluid*". These colloids produced by Faraday are still optically active today, and thanks to his work, Faraday is known as the first researcher to make discoveries in the field of nanoscience and nanotechnology. On the other hand, Ag NPs were first synthesized by Mathew Carey Lea in 1889 [45]. In his study, Lea used the citrate-reduction method, which is one of the simplest Ag NP synthesis methods, and obtained highly concentrated Ag hydrosols at room temperature. After these primitive synthesis approaches about 150 years ago, the studies in which the modern synthesis of NPs were reported with different methods [45-51].

Seed-mediated growth approaches are often preferred to be controlled the shape of metallic NPs. The NPs obtained with this approach can be oriented to the desired morphology and are showing unique properties for various applications. Simply, the synthesis procedure is based on the elimination of unwanted and spontaneous nucleation during the growth of crystals of different morphologies, and the final product strongly depends on the quality of the initial seeds. Besides, it is possible to calculate the size of the final product. This expected size can be calculated from a theoretical equation [52]:

$$r = r_{seed}\{([M_{added}] + [M_{seed}])/[M_{seed}]\}^{1/3} \quad (1.14)$$

Here, r is the radius of the final and larger particle, r_{seed} is the radius of the seed NP, $[M_{added}]$ is the concentration of added metal in growth solutions, and $[M_{seed}]$ is the concentration of metal in seed NPs.

A typical seed-mediated growth procedure consists of two steps: (1) synthesis of the seed NP and (2) incorporation of these seeds into a growth solution containing the metal precursor, reducing, and shape-directing agent [53]. The activation energy required for a metal reduction on seeds is lower than the energy required for homogeneous nucleation of seeds in solution. In this way, the seeds added to the solution allow the autocatalytic growth of metal atoms on them [54]. Besides, with the presence of seeds in the solution, the formation of randomly formed polydisperse particles can be prevented and monodisperse NPs with desired morphologies can be obtained.

Recent developments in the seed-mediated growth of Plasmonic Au and Ag NPs with different morphologies and sizes have opened up the new opportunities in the usage of these materials for different purposes (Figure 1.5). Thanks to the advantages of these materials in the last two-decades, they have been integrated into different spectroscopy techniques such as surface-enhanced Raman spectroscopy (SERS), surface-enhanced fluorescence (SEF), surface-enhanced infrared absorption (SEIRA). Table 1.1 and 1.2 shows to common seed-mediated synthesis conditions of Au and Ag NPs, respectively.

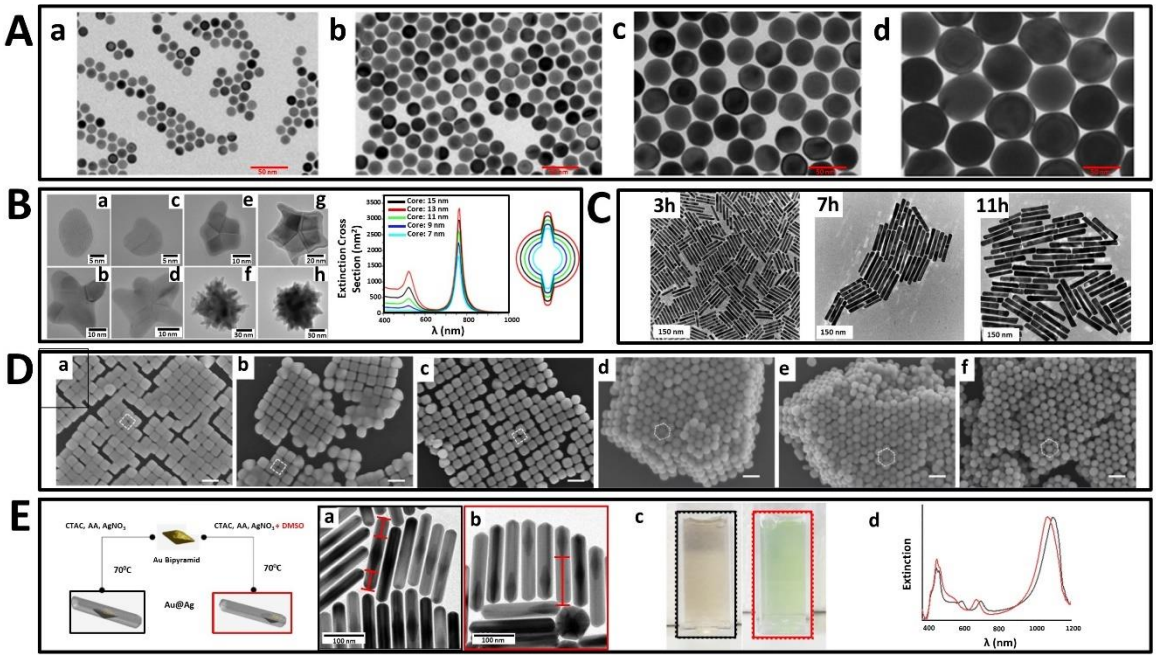

Figure 1.5. *Examples of the anisotropic NPs produced by seed-mediated growth approaches under different experimental conditions.* ***(A)*** *TEM images of spherical Au NPs with different diameters: a) 15 nm, b) 23 nm, c) 46 nm, and d) 80 nm. The NPs were obtained using different seed (10 nm) solution volume of 300 µL, 100 µL, 10 µL, and 5 µL, respectively. Adapted with permission from ref. [55]. Copyright 2013, John Wiley and Sons.* ***(B)*** *HRTEM images of Au NSs obtained from different kinds of seeds: a-b) 2 nm of Pt, c-d) 2.3 nm Au, e-f) 15 nm Au, and g-h) 30 nm Au seed. The NSs were obtained from [$HAuCl_4$]/[seed] ratios of 45, 675, 67.5, 880, 1.5, 90, 1.5 and 11.5 from a to h, respectively. i) Calculated extinction cross section for Au NSs with different sizes of the seeds using BEM. Adapted with permission from ref. [56]. Copyright 2010, American Chemical Society.* ***(C)*** *TEM images of evolution of Au NRs after different periods. Growth of NRs was halted by addition of MUTAB. Adapted with permission from ref. [57]. Copyright 2013, American Chemical Society.* ***(D)*** *SEM images of Ag NCs obtained using 1-5 nm of Ag seed, and transformation of the NCs to spherical Ag NPs after different chemical etching time: a) 0 min, b) 105 min, c) 120 min, d) 135 min, e) 150 min, and f) 165 min. Adapted with permission from ref. [58]. Copyright 2018, American Chemical Society.* ***(E)*** *Growth of Ag on bipyramidal Au NPs: a) TEM images of symmetric and b) asymmetric growth of Ag on bipyramidal Au NPs absence and presence of DMSO, respectively. c) and d) optical properties of Ag NRs prepared with and without DMSO. Adapted with permission from ref. [59]. Copyright 2021, American Chemical Society.*

Table 1.1. Summary of different seed-mediated growth methodologies for Au NPs

Shape	Reducing Agent	Stabilizing Agent	$Size_{Seed}$ (nm)	$Size_{Final}$ (nm)	Ref.
Bipyramid	Ascorbic acid	CTAB	6.1 ± 0.2	44 ± 1.6 to 585.9 ± 29.7	[60]
Cube	Ascorbic acid	CTAB	3.5	25 – 50	[61]
Prism	Ascorbic acid	-	5.2 ± 0.6	From 148 ± 13.5 to 220 ± 13.6	[62]
Rod	Ascorbic acid	CTAB	<4	7 – 12*	[63]
	Hydroquinone	CTAB	3 – 4	6 – 8*	[57]
Sphere	Hydroquinone	Citric acid	15	From 65.6 ± 5 to 92.2 ± 4	[64]
	Ascorbic acid	PEI	6±2	From 37 ± 3 to 108 ± 20	[65]
	Ascorbic acid	CTAC	From 10 to 46	From 15 to 150	[55]
Star	Ascorbic acid	CTAB	11.4 ± 0.9	82.6 ± 4.9**	[66]
	DMF	PVP	From 2 to 30	From 45 to 100**	[56]
Triangle	3-Butenoic acid	BDAC	54.8 ± 4	From 86.3 ± 4 to 173.7 ± 7.1	[67]
	Ascorbic acid	CTAC	From <2 to 10	From 40 to 150	[68]
Wire	Citric acid	-	13 ± 2	Various lengths	[69]
	Ascorbic acid	CTAB	2 – 3	From 700 to 4450	[70]

(*) Aspect ratio according to the Length per diameter of Au nanorods, and (**) The Size from length-to-length

Table 1.2. Summary of different seed-mediated growth methodologies for Ag NPs.

Shape	Reducing Agent	Stabilizing Agent	$Size_{Seed}$ (nm)	$Size_{Final}$ (nm)	Ref.
Bipyramid	Ascorbic acid	CTAB	2 – 5	87 ± 3*	[71]
	NaBr, Ethylene glycol	PVP	25	From 75 to 150	[72]
Cube	Ascorbic acid	CTAC	1 – 5	From 23 to 60	[73]
Plate	Ascorbic acid	CTAB	14 ± 4, 31 ± 8	67 ± 9*	[74]
Prism	Ascorbic acid, Citric acid	-	Various size	From 52 ± 6 to 1050 ± 31*	[75]
Rod**	Ascorbic acid	CTAC	From 69 ± 3 to 76 ± 5*	From 100 to 350*	[59]
Sphere	Citric acid	-	4	From 20 to 74	[76]
	Citric acid, Tannic acid	-	Various sizes	From 10 to 200	[77]
	Ascorbic acid	-	23	From 40 to 300	[78]
Triangle	Ascorbic acid	CTAB	3.4	46	[79]
	Ascorbic acid	-	5.6 and 10.8	From 17.5 to 78.7	[80]

(*) Edge length and (**) Au seeds were used

1.2. Surface-Enhanced Raman Spectroscopy

1.2.1. Definition

Undoubtedly, SERS is an advance spectroscopy technique in which the nature of plasmonic NPs is the best reflected. The technique takes advantage of plasmonic NPs concentrating electromagnetic energy via LSPR. In this way, it is aimed to greatly enhance the Raman signals of molecules adsorbed on the plasmonic surface by employing inelastic light scattering. These enhancement factors can be 10^8 or more, and in some cases, allow for single-molecule detection as well [81].

SERS is based on the logic of amplifying the signals of molecules from Raman scattering through plasmonic NPs. In terms of SERS, the first appearance of the technique took place almost fifty years after the concept of "*Raman scattering*" was introduced to the literature, and as a result of an *accident*. In 1974, Fleischmann et. al reported that an unexpected Raman signal enhancement from pyridine adsorbed on a roughened Ag electrode [82]. However, in reporting these findings, it was suggested that the increase in Raman signal was due to the surface area of the Ag electrode used, and thus the presence of much more pyridine adsorbed to the surface area. The real reason was revealed by Albrecht and Creighton, who repeated the same experiment three years after Fleischmann and his co-workers, and observed a 10^5-fold increase in the pyridine Raman signal with the help of Ag electrode, and accordingly, they suggested that this phenomenon may be due to the SPR effect of plasmonic Ag surface [83]. In 1978, Moskovits correctly predicted that in addition to roughened metal electrodes, Raman signal enhancement could also occur for colloidal metal particles [84]. Creighton et al. (1979) confirmed this prediction in their work with Ag and Au hydrosols [85]. Thanks to these discoveries, the SERS technique has become an important tool for analytical purposes to overcome the low efficiency of Raman scattering processes.

1.2.2. Raman Scattering

Raman scattering of a molecule is the inelastic scattering produces when the molecule interacts with a light. When this phenomenon was proved by the experiments of Raman and Krishnan almost a century ago, it began to be called Raman scattering [86].

When molecules interact with a monochromatic beam of light, a scattering process is observed. During the process, if the frequency of the incident photon ($\omega_{incident}$) is equal to the frequency of the emitted photon ($\omega_{emitted}$), a type of elastic scattering called "*Rayleigh scattering"* occurs. On the other hand, there is a small probability of energy exchange between $\omega_{incident}$ and $\omega_{emitted}$, and this kind of exchange gives us the "*spectroscopic fingerprint*" of the molecule of interest. This new type of scattering, which is different from Rayleigh scattering because of energy exchange, is called Raman scattering. In Raman scattering, the frequency of the incident photon can be greater or less than the frequency of the emitted photon. In this case, "*Stokes"* ($\omega_{incident} > \omega_{emitted}$) and "*anti-Stokes"* scattering ($\omega_{emitted} > \omega_{incident}$) are detected. Rayleigh scattering is 104-105 times more intense than Raman scattering. The energy generated by anti-Stokes scattering is considerably lower than the energy produced by Stokes scattering. For this reason, the energy generated by anti-Stokes scattering is often ignored (Figure 1.6).

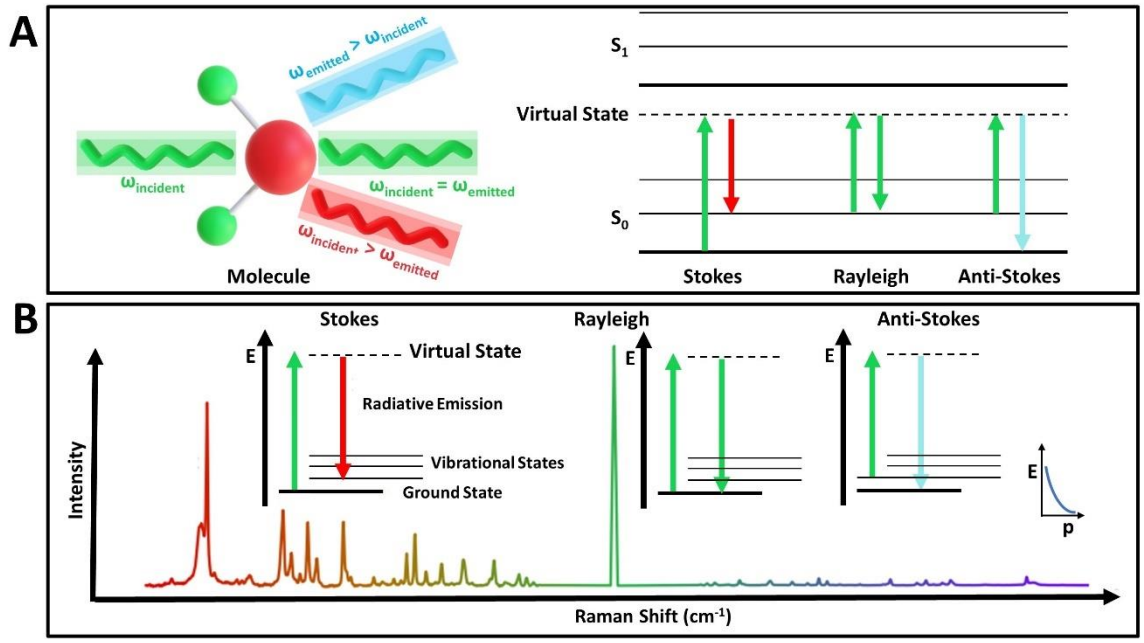

Figure 1.6. (A) *Schematic representation of the three possible scattering phenomena via Raman active molecule. Jablonski diagram also shows the electronic transitions involved with the different scattering observed.* ***(B)*** *The Raman spectrum of one of the model molecule, aspirin, and visualization of Stokes, Rayleigh, and anti-Stokes scattering in the spectra. Boltzmann energy distribution also indicates that occurring of anti-Stokes scattering is less probable than Stokes scattering. Where E and p relates with energy and population density, respectively. Adapted from ref. [87].*

There are some fundamental differences that distinguish Raman spectroscopy from widely used analytical spectroscopy methods such as infrared (IR). First, Raman spectroscopy is the measurement of inelastic scattering produced by vibrating molecules. IR spectroscopy, on the other hand, measures the light absorbed by these molecules. Another important difference is that for these vibrations to become Raman active, there must be changes in their polarizability. In contrast, in the IR active state, there must be changes in the dipole moment. This takes us to the "*mutual exclusion principle*". According to this principle, a molecule with central symmetry such as CO_2, has polarization or dipole moment properties because the bonds between atoms of the molecule can exhibit symmetrical or asymmetric vibrations. Therefore, the CO_2 molecule cannot be Raman or IR active at the same time (Figure 1.7A). Instead, complex molecules are excluded from this principle because they do not have central symmetry. For instance, H_2O does not have any molecular symmetry, so both Raman and IR can be active at the same time (Figure 1.7B). Other differences between Raman and IR spectroscopy are that water does not block the Raman spectra. Solid, liquid and gas forms of different samples can be used in Raman spectroscopy whereas gaseous samples are generally not preferred in IR spectroscopy.

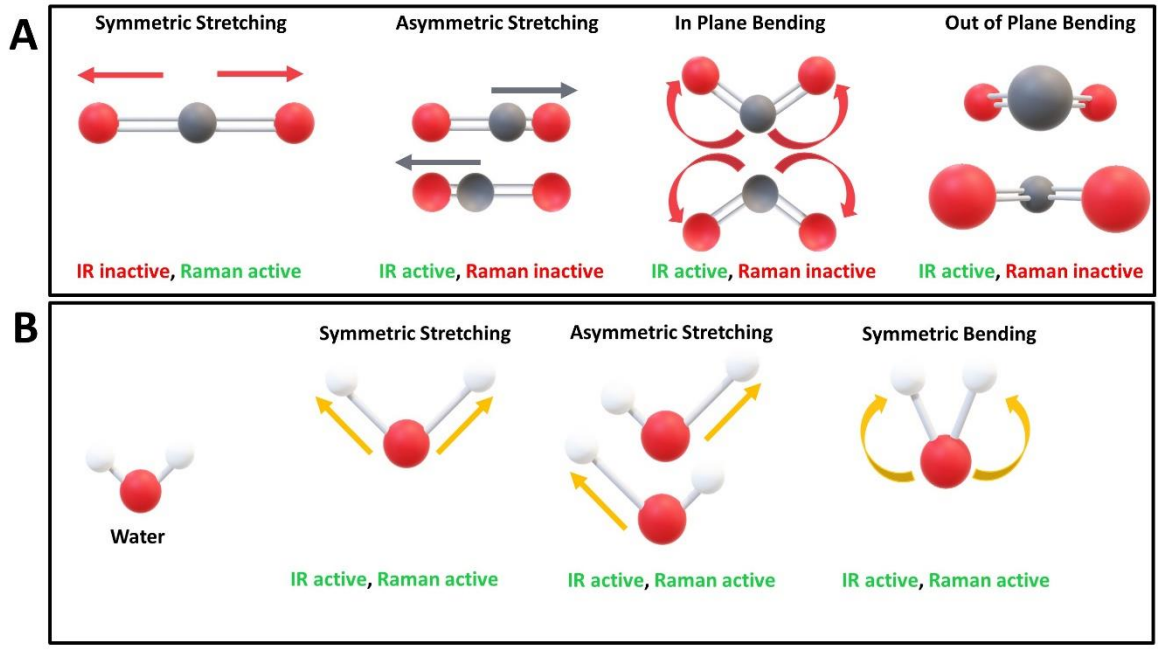

Figure 1.7. *Schematic representation of mutual exclusion principle.* ***(A)*** *a molecule with central symmetry such as CO_2 has polarization and dipole moment properties. For this reason, it cannot be IR and Raman active at the same time.* ***(B)*** *On the other hand, water molecule can be both IR and Raman active at the same time because of it has not any central symmetry.*

When we look at Raman spectra of a molecule of interest, Rayleigh scattering gives a single and very intense peak and does not give us any information about the vibrational transitions of the molecule. Contrary, in this spectroscopy method, the differences in the wavelength of inelastically scattered light are measured according to the wavelength of the light interacting with the molecule. These differences are called "*Raman shifts*" and it is referred to as cm^{-1}. Raman shift values are negative for anti-Stokes scattering and positive for Stokes scattering due to energy loss and gain. The equilibrium for Raman shift is given by the relation:

$$cm^{-1} = {}^{1}/_{\lambda_{incident}} - {}^{1}/_{\lambda_{emitted}} = {}^{h(\omega_{incident} - \omega_{emitted})}/_{c} \qquad (1.15)$$

Where $\lambda_{incident}$ is the incident radiation wavelength, $\lambda_{emitted}$ is the scattered photon radiation wavelength, and c is de velocity of light.

In the data obtained from Raman spectroscopy, apart from the Raman shift, the intensities of the peaks are also very important to understand how much the examined sample is present in the environment. This is also known as the "*intensity of Raman scattering (I_{RS})*" and is the number of photons scattering over all molecular directions over the mean time unit:

$$I_{RS} = \sigma_{RS} I_0 \qquad (1.16)$$

Where σ_{RS} is the Raman cross-section and I_0 is the incoming flux of photons.

1.2.3. Mechanism of SERS Enhancement

The biggest feature of the SERS technique is that it increases ordinary Raman intensities to gigantic levels. In classical Raman spectroscopy, the interaction occurs between the incident light and the molecule of interest; In addition, interactions with plasmonic NPs are also involved in SERS. In performing this enhancement, the technique uses two different generally accepted mechanisms: **(1)** electromagnetic, and **(2)** chemical enhancement mechanisms (Figure 1.8).

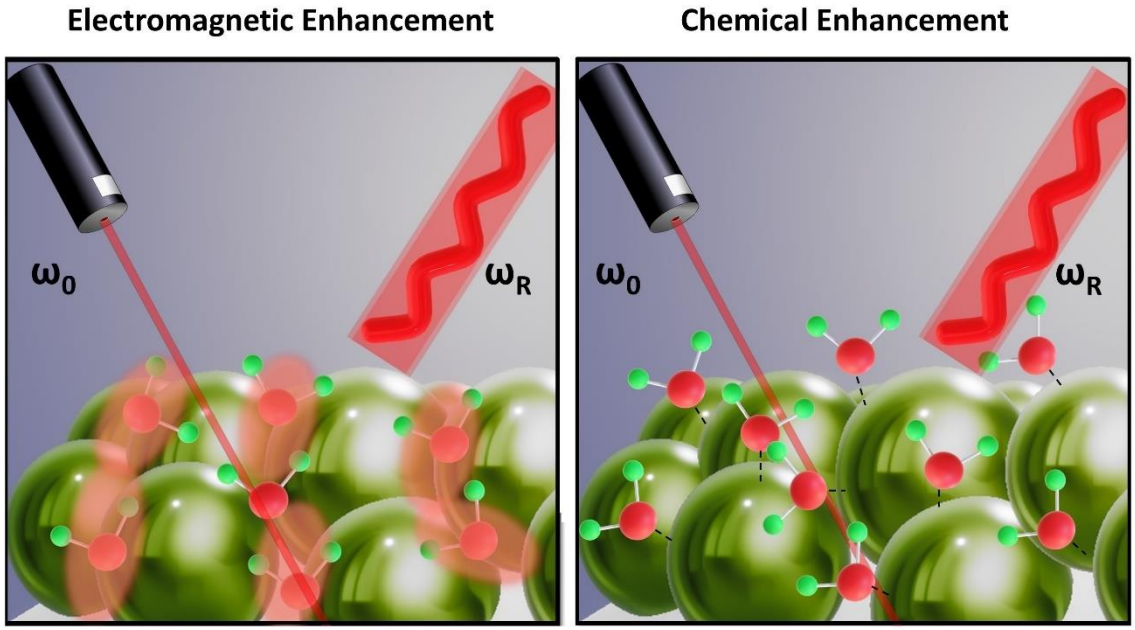

Figure 1.8. *Illustration of SERS enhancement mechanisms. In electromagnetic enhancement, SERS signal of the molecule of interest can be greatly enhanced mainly because of "hotspots" contribution. On the other hand, chemical enhancement mechanism is about some physicochemical properties such as electron transfer and modification of polarizability of the molecule which is adsorbed on the plasmonic surface.*

In the electromagnetic enhancement (EME) mechanism, one of the dominant contributions to SERS, dramatic enhancement is seen in SERS signals, approximately 10^{10}-10^{11} [88]. EME is based on LSPRs, and large local field enhancements are applied to molecules adsorbed on or near these NPs [89]. Because of LSPR, the nature of EME is tightly dependent on different factors such as the type, morphology, size, and dielectric properties of plasmonic NPs [90]. By EME, local field enhancements on the surface of plasmonic NPs can be considered to occur in two successive steps, both by incident light and Raman scattering. The first is the enhancement of a local field near the plasmonic NPs at the resonant incident frequency, and the other one is the further enhancement of Raman scattering, which occurs when Raman frequency and plasmon resonance overlap [91]. If the frequencies of the incident light and the Stokes scattering of the molecule of interest are similar, then the magnitude of the signal intensity enhancement is approximately proportional to the fourth power of the field amplitude [92]:

$$I_M = {|E_{loc}(\omega_0)|^2|E_{loc}(\omega_R)|^2}\Big/{|E_0(\omega_0)|^2|E_0(\omega_R)|^2} \approx {|E_{loc}(\omega_R)|^4}\Big/{|E_0(\omega_0)|^4} \quad (1.17)$$

Here, I_M is the magnitude of the signal intensity enhancement, E_0 and E_{loc} the incident field on plasmonic NP and local field at the molecule of interest, respectively, ω_0 is the incident frequency of light and, ω_R is Raman frequency of scattered light.

Moreover, depending on their distance, very strong electromagnetic and inhomogeneous enhanced electromagnetic fields are formed between more than one plasmonic NP. These areas, called "*hotspots*", are the result of interparticle interactions and are generally quite strong within sub-10 nm gaps [93]. If the molecule of interest is smaller than the size of these gaps and is within the hotspot area, there is a tremendous increase in the Raman frequency of scattered light and thus the SERS intensity of that molecule. The increasing also depends on factors such as the radius of the NP and the distance of the molecule from the plasmonic surface.

On the other hand, the chemical enhancement (CE) mechanism is based on the change in the Raman polarizability tensor of the molecule-surface complex formed as a result of the molecule chemically adsorbed on the plasmonic surface [89]. It can be considered as a charge transfer from the adsorbed molecule of interest to the plasmonic metal or from this molecule to the metal. When compared to EME, CE mechanism provides a relatively less overall enhancement for SERS, approximately 10^1-10^2, and is entirely related to changes in the polarizability of the surface adsorbed molecule.

1.2.4. The Factors Affecting SERS

One of the vital issues for SERS applications is to increase the quality of the signal obtained from the molecule of interest. While doing this, some factors have fundamental importance such as correct estimation of the SERS enhancement factor (EF), instrumental condition, and correct adjustment of the substrate-molecule interaction.

One of the most important features that distinguish SERS from classical Raman spectroscopy is the SERS substrates. By accurately estimating the EFs of these substrates, novel SERS substrates can be revealed, and more illuminating information can be obtained about their analytical performance:

$$EF = {I_{SERS}\, N_{RS}}/{I_{RS}\, N_{SERS}} \quad (1.18)$$

Where I_{SERS} and I_{RS} are collected intensities from SERS and Raman spectroscopy, respectively. On the other hand, N_{SERS} and N_{RS} are the numbers of molecules probed by SERS and Raman spectroscopy, respectively.

Data obtained from Raman intensities might differ according to dry and liquid samples. This causes that N_{RS} to vary according to the physical condition of the analyte. When measuring a dry sample in Raman spectroscopy, N_{RS} is calculated as:

$$N_{RS} = \rho \pi r^2 t \quad (1.19)$$

Here, ρ and t are the density and thickness of the dry sample, respectively, and r is the laser spot radius. When calculating N_{RS} from the liquid samples, the concentration (C_{RS}) and volume (V) of the solution should be well known. N_{RS} from solutions is calculated as [94]:

$$N_{RS} = C_{RS} V \quad (1.20)$$

For this equation, the concept of "*effective volume* (V_{Ef})" was introduced when calculating the N_{RS} from the liquid sample [95]. According to this:

$$V_{Ef} = Al \quad (1.21)$$

Where A is the area of laser spot size and l represents the thickness of an ultrathin film or solution layer near the "*ideal focal plane* (z)". Hence, at the ideal focal plane (z = 0), the I_{RS} is expected to be at its highest for liquid samples. With Raman signals collected from below and above of ideal focal plane, the average signal is integrated with the signals from the different planes and l can be calculated:

$$l = {\int_{-\infty}^{\infty} I(z)dz}/{I_{max}} \quad (1.22)$$

On the other hand, calculating N_{SERS} is simpler than N_{RS} and it is sufficient to know only the geometric surface area of the illuminated spot (S_I) and the area/areas occupied by the molecule of interest (S_M):

$$N_{SERS} = {S_I}/{S_M} \quad (1.23)$$

When all these factors are obtained correctly, EF can be calculated exactly, thus, improved the quality of SERS applications, and better comparing the performances of SERS substrates with each other.

Generally, SERS and therefore the substrates are often criticized for their low reproducibility and unavailability in terms of universal methods. Changing instrumental conditions or sample preparation techniques are negatively influence SERS reproducibility [96]. The improvement of these factors is directly proportional to the increase in SERS performance. Although the equipment of different qualities are used for SERS, basic conditions such as focusing position and laser power are important in terms of reproducibility as they determine how much the SERS signal is dispersed and how much is detected from the analyte [97]. Another important parameter is the excitation wavelength for the molecules of interest. The correct selection of the excitation wavelength in various SERS applications directly affects the fate of the measurement. There are eight different excitation wavelengths used in Raman spectroscopy: **(1)** 244 nm, **(2)** 325 nm, **(3)** 488 nm, **(4)** 514 nm, **(5)** 532 nm, **(6)** 633 nm, **(7)** 785 nm and **(8)** 830 nm. Among them; 244 and 325 nm are used in the electronics and semiconductor industry, while 488, 514, 532 and 633 nm are for general use [98]. On the other hand, 785 and 830 nm find themselves in the SERS applications of sensitive samples such as biological samples. The most common laser sources in SERS are those that remain in the visible (from 488 to 633 nm) and near-infrared lines (785 and 830 nm). The point to be considered when using these excitation wavelengths is that which objective should be used for a SERS application when the signal is taken from the analyte. For instance, reducing the augments of the objective will reduce the energy density of the molecule of interest, and SERS signal quality is negatively-affected even if the same sample and same excitation wavelength are used [98] (Figure 1.9A).

The consensus is that it is ideal to use a wavelength that is slightly red-shifted from the maximum LSPR [99]. However, some studies claim the opposite, and suggest that a wavelength that is slightly blue-shifted from the maximum LSPR should be used [100]. The important point, however, is to establish the LSPR profile before and after the plasmonic surface has been treated with the analyte. In this way, the excitation wavelength to be used can be decided more accurately (Figure 1.9B).

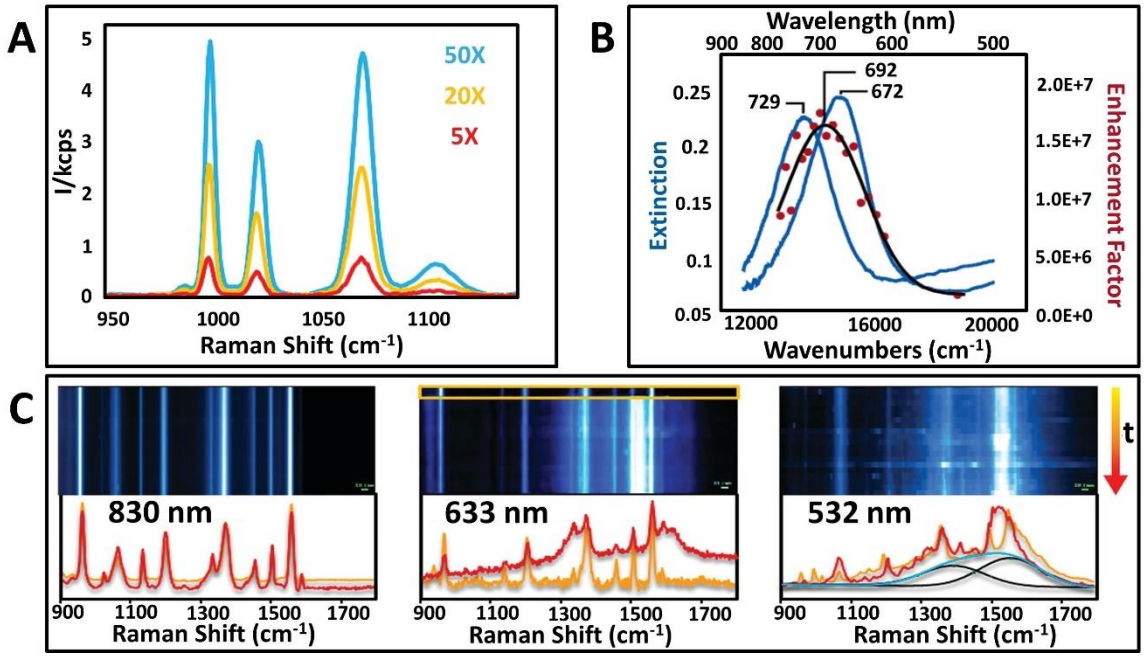

Figure 1.9. (A) SERS spectra of BT adsorbed on Ag NPs upon excitation with a 514 nm laser with the same power at the sample but using different objectives. Adapted with permission from ref. [98]. Copyright 2012, American Chemical Society. (B) LSPR shift and SERES profile of BT. λ_{max}: 672 nm is the LSPR extinction of the NP, λ_{max}: 729 nm is the LSPR extinction of BT adsorbed on the NPs, and $\lambda_{ex,max}$: 692 nm is the best excitation wavelength according to the SERES data points. Adapted with permission from ref. [100]. Copyright 2005, American Chemical Society. (C) Photocombustion of the sample. Blue and black lines show the amorphous carbon background. On the other hand, yellow and red spectra indicate that SERS fingerprint of 1-NAT at time 0 and 1470 s, respectively. Adapted with permission from ref. [98]. Copyright 2012, American Chemical Society.

One of the worst things about the wrong selection of excitation wavelength is that it might cause the sample to *burn* (Figure 1.9C). This is a common problem for SERS known as "*photocombustion*" [101]. One of the most common examples of this phenomenon is the undesired sp^2 stretching observed at 1360-1560 cm^{-1} as a result of graphitic or carbon formations, also known as "*cathedral bands*" [98, 102]. This problem can be avoided by reducing magnifications or the laser power.

The background noises affect the received signal quality during SERS measurements. In particular, these noises are more dominant when the analyte concentration is low. One of the first and perhaps the best interventions to eliminate this problem is to take some steps directly

to improve the signal quality of the analytes. The molecules with functional groups such as –SH, $–NH_2$, $–NH^{4+}$, –COO, –CN, and carbonyl give very high SERS signals due to their strong binding to the plasmonic metal surface [103]. However, not every analyte has such functional groups, and it is, therefore, more appropriate to work towards the development of novel plasmonic substrates rather than molecules.

The simplest improvement that can be made to plasmonic substrates is electrostatic modifications. We can see this in the case of citrate-capped Au or Ag NPs. Thus, these plasmonic NPs with negative surface charge can easily interact with a positively charged analyte, such as RhB, MG, and CV dyes, and a strong SERS signal can be collected [95]. In the cases where it is not sufficient, bimetallic plasmonic nanocomposites can be produced, and stronger SERS performances can be obtained. Another improvement that can increase the interaction of the analyte with the plasmonic surface is the covalent attachment of an analyte-specific molecule to the plasmonic surface. In this method, which is also called the "*in-direct*" SERS method, the molecules that normally give a low signal for SERS are easily captured by the molecule-specific "*bridge molecules*" on the surface, thus increasing SERS signal.

One of the challenging topics to improve substrate-molecule interaction is that being the development of plasmonic nanocomposites and is the introduction of different types of materials as novel SERS substrates [104-106]. Plasmonic NPs with different sizes, morphologies, or compositions, can be used not only alone but also with various polymers, metals that do not have a plasmonic nature, or porous materials such as mesoporous SiO_2 or metal-organic frameworks (MOFs). In this way, application-specific SERS-based analytical detections of the various molecules at very low detection limits can be easily carried out.

1.3. Plasmonic Nanocomposites as SERS Substrates

1.3.1. Definition

Although plasmonic NPs with different sizes or morphologies have unique optical properties, different SERS applications needs many more different types of substrates for reasons such as increasing light-matter interaction, chemical stability, application functionality, and reaching low detection limits for the analytes. It can be easily reached these desired properties via plasmonic *nanocomposites* formed by combining different plasmonic and/or not-plasmonic materials under a single roof.

According to IUPAC recommendation, a nanocomposite is defined as "*composite in which at least one of the phase domains has at least one dimension of the order of nanometres*" [107]. The term nanocomposite is generally used for complex materials in nano-form in which materials with more than one different property are brought together. Although the term seems to have emerged in the last two-decades, the first hybrid nanomaterials were reported in 1957 with magnetic Co@CoO NPs [108].

When it comes to enhancing substrate-analyte interaction and performing lower levels of SERS detection, the questions such as why we need such a complex material can be easily answered, and the advantages of such nanocomposites as SERS substrates can be better understood. The first, the presence of a plasmonic NP as a hybrid with another material can protect it from oxidation or increase its stability throughout the SERS measurements. Hence, the nanocomposite obtained from NPs coated with a second metallic or organic materials can provide this property. The second, plasmonic nanocomposites turn into complex materials with not only a single property, but also different properties. The best examples of this are that magnetoplasmonic materials exhibit both plasmonic and magnetic behavior or that plasmonic NPs that can be integrated into materials with catalytic properties such as TiO_2 and ZnO also act as well-catalysts. The third, a nanocomposite can be gained more affinity to chemical or biological structures for SERS-based applications. This means that molecules that are normally difficult to detect can be detected without any problems. Finally, the optical properties of these kinds of nanocomposites can be easily adjusted according to the type of final product being produced.

Plasmonic nanocomposites can be broadly classified into two main groups: (1) layer-by-layer (LbL) self-assembled plasmonic nanocomposites, and (2) core-shell plasmonic nanocomposites.

1.3.2. Layer-by-Layer Assembled Plasmonic Nanocomposites

The layer-by-layer (LbL) technique can be explained as the sequential and electrostatic adsorption of oppositely charged polymers, or polyelectrolytes (PE), on each other. One of the first studies based on this technique was carried out in 1997 with PEs sequentially adsorbed on a charged planar substrate [109]. Since then, not only charged planes but also different types of particles have been used as templates for the adsorption of these PEs on each other. The LbL technique generally starts with the preparation of a PE solution and the addition of a template material with an opposite charge into this solution. This allows the PE to be adsorbed on the template surface. The obtained PE-coated template is added into another PE solution with an opposite charge to the adsorbed, and this process is continued so that the desired charge remains on the outer surface. Generally, the final surface charge must be greater than +25 mV or lower than -25 mV because of PE adsorption, so that the nanocomposites do not aggregate in the solution. The method serves as a basic technique for obtaining a wide variety of colloidal plasmonic nanocomposites. In this way, different kinds of plasmonic nanocomposites can be easily prepared (Figure 1.10).

One of the biggest advantages of the LbL technique is that it is suitable for almost all colloidal templates, and the templates with different sizes, morphology or composition do not pose a problem for this method. Moreover, a wide variety of PEs such as PSS, PMAA, PAH, PDDA or PLL can be used for this method. On the other hand, there are two main disadvantages of the method. One is that it is very time-consuming due to the steps such as PE coating, purification, and NP deposition, and the other one is that since PEs are adsorbed on the template surface by electrostatic interactions, it can be observed that these PEs are also de-adsorbed from the surface over time. This may cause the nanomaterials deposited on the surface to separate from the template material, and become free in the medium, because of the changing of the final surface charge of the material used for the template.

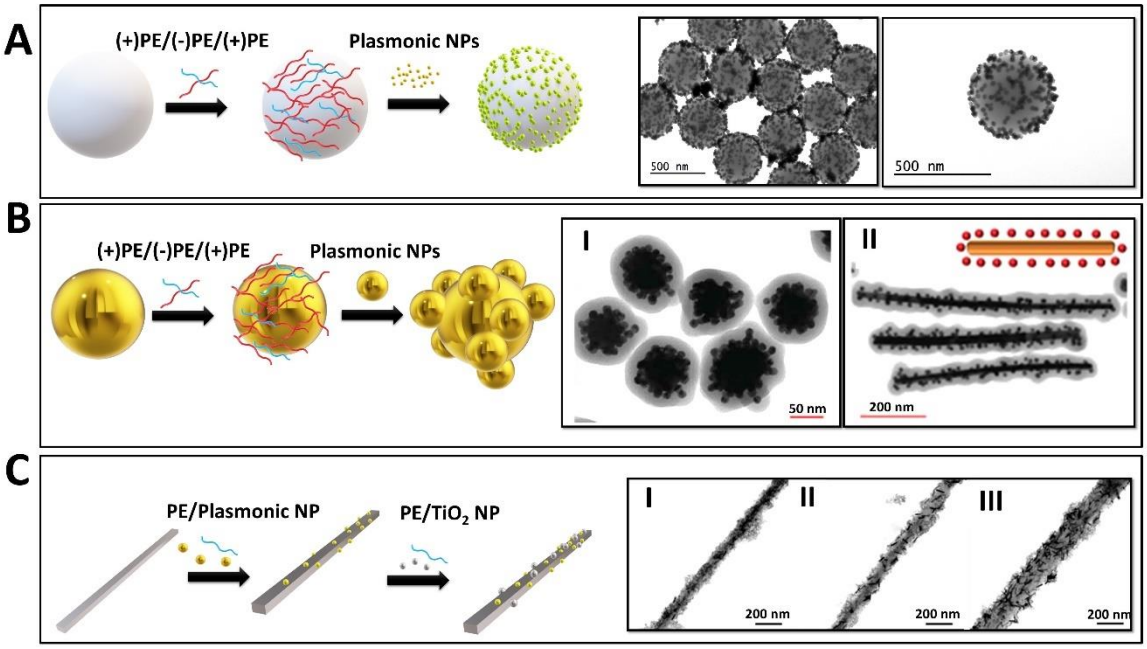

Figure 1.10. *Schematic representation of LbL technique.* ***(A)*** *Coating of an inert template with PEs and depositing of plasmonic NPs onto it. Inset figures show TEM images of the nanocomposites which obtained from an inert template, PS bead, and Ag NPs on the surface of it.* ***(B)*** *Coating of a plasmonic NPs with PEs and depositing of other plasmonic NPs onto it: I) Au-Au core-satellite nanocomposites coated with SiO_2 shell (with spherical core), and II) the structures with Au NR core. Adapted with permission from ref. [110]. Copyright 2018, Royal Society of Chemistry.* ***(C)*** *Coating of TiO_2 NW template with PE and depositing of plasmonic NPs and TiO_2 NPs onto it. TEM images of the nanocomposites with different molar ratios of Au/TiO_2: I) 0.023, II) 0.059 and III) 0.1. Adapted with permission from ref. [111]. Copyright 2019, Multidisciplinary Digital Publishing Institute.*

The distances between the plasmonic NPs deposited onto the surface can be increased or decreased with changes in the NP deposition time or with multistage deposition methods. Adjustment of these inter-NP gaps is a factor that determines the interparticle plasmon coupling in particular. Plasmon coupling is a very important phenomenon for SERS and generally broadened and redshifted LSPR bands due to the coupling are not preferred in some applications [112].

In some SERS applications, these kinds of nanocomposites can be coated with another material. In this way, it is expected that the plasmonic nanocomposite will not be affected by changes in different and realistic environmental conditions, so that the SERS signal quality will remain the same as the experimental conditions. It is also observed in some cases where the

template material is eliminated. In this manner, plasmonic NPs, which cannot be dispersed into the environment with the help of the outer shell, are trapped inside the shell and are free in the large voids obtained due to the destruction of the template. This results in an increase in the SERS signal from the analyte due to both more analyte filling into these voids and more hotspots appearing between the plasmonic NPs. In one of these studies, Mariño-Lopez et al. (2019) developed a SERS substrate made of microporous SiO_2 capsule in which Au NPs are entrapped capable of detecting analytes in natural water [113]. For this, the authors coated PS templates with LbL technique and adsorbed Au seeds onto these templates. Then, the nanocomposite was covered with SiO_2 shell and PS template was removed at 600^oC to obtain void@Au@SiO_2 nanocomposites as SERS substrates. Finally, the authors grew the seeds in the composite with growth solutions. The results show that even in natural river water, the composites retain their colloidal stability and can detect DDT up to 1.77 ppb.

1.3.3. Core-Shell Plasmonic Nanocomposites

Core-shell materials are one of the special classes of nanocomposites. A typical plasmonic core-shell nanocomposite has two main parts, core, and shell parts. By increasing or decreasing the core size and shell thickness, or by changing the morphology of these parts, the plasmonic properties of the nanocomposite can also be adjusted as desired. In this type of material, the part that works effectively in various SERS applications can be a core, shell, or both. If the core is the effective part, then the shell is responsible for protecting it for various reasons. These reasons include protecting the core from aggregation, high temperature and oxidation or keeping unwanted side-reactions in the solution away from the core.

Biplasmonic core-shell nanocomposites are one of the highly beneficial SERS substrates. In these substrates, Au NPs are generally chosen as core materials due to its stability and easy preparation. Likewise, there are also core-shell materials in which Ag NPs are selected as cores. The advantage is that, better SERS performances and broadening the range of excitation spectrum can be achieved because both parts of the nanocomposite are plasmonic [114]. In addition, different extinction spectrums can be obtained depending on the plasmonic material used in the core and shell, or the thickness of the plasmonic shell (Figure 1.11). The shell thickness is an important issue not only for biplasmonic core-shell but also for all of the core-shell nanocomposites, and it can easily affect the SERS activity of the substrate. In one study, Wang et al. (2019) tested the SERS performance of Au@Ag biplasmonic core-

shell materials with different Ag shell thicknesses on R6G and thiram, a pesticide [115]. The results showed that among different Ag shell thicknesses ranging from 3 to 13 nm, covering an Au core of about 32 nm, the nanocomposite with a thickness of 8.5 nm gave the best SERS performance. The authors also reported that the Ag shell thickness exceeded a certain threshold value, and therefore, the SERS activities of the nanocomposites with shell thicknesses higher than the optimum value decreased. On the other hand, the nanocomposite with a shell thickness of 8.5 nm was able to detect R6G and thiram up to 1×10^{-12} M and 1.09×10^{-9} M, respectively.

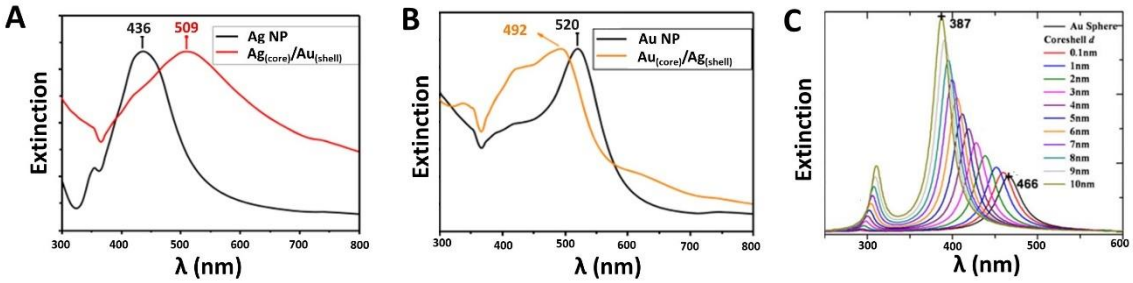

Figure 1.11. *Extinction spectrums of different types of plasmonic-plasmonic core-shell nanocomposites. The LSPRs of the nanocomposites of the same composition differ from each other depending on which plasmonic material is used in the core or shell:* ***(A)*** *The spectrum of core-shell Ag@Au NPs, and* ***(B)*** *core-shell Au@Ag NPs. Adapted with permission from ref. [116]. Copyright 2020, Springer Nature.* ***(C)*** *The simulation of the changing of LSPR of Au@Ag nanocomposites with different Ag shell thicknesses increasing from 0.1 to 10 nm. Adapted with permission from ref. [117]. Copyright 2012, Springer Nature.*

Post-modifications of biplasmonic core-shell nanocomposites in various ways can also yield stronger SERS substrates. The most commonly used of these post-modifications is the Galvanic replacement reaction (GRR) [118]. GRR is a corrosion process caused by the electrochemical potential difference between two different metals [119]. When this reaction is applied to a biplasmonic nanocomposite, we see that Ag disappears, and porous or hollow SERS substrates can be obtained depending on where Ag is in the core-shell structure. The study of Wang et al. (2022) can be given as a good example for this issue [120]. Accordingly, the authors added $HAuCl_4$ at certain concentrations to Au@Ag and Ag@Au nanocomposites to obtain porous NP and porous nanoshell materials, respectively, and compared these substrates with Au NPs in terms of both SERS performance and drug loading capacity, using

DOX, an anticancer drug. The results showed that the DOX signal collected by porous NPs is 68-times more intense compared to Au NPs under SERS. On the other hand, it was revealed that porous nanoshells are the materials with the highest DOX loading capacity.

Plasmonic nanomaterials can be also used with non-plasmonic materials to obtain novel nanocomposites with different properties for SERS applications. Commonly used metals for the core, which do not have a plasmonic nature, are usually chosen from magnetic NPs [121, 122]. These types of substrates are particularly ideal for many SERS applications, as they can both move under a magnetic field and exhibit plasmonic characteristics. For instance, Nguyen et al. (2020) investigated the separation and SERS detection of thiram via core-shell nanocomposite consisting of the magnetic core and plasmonic shell in star morphology [123]. It was reported that the nanocomposite successfully achieved magnetic separation in diluted thiram solution and could detect 10^{-8} M thiram via SERS. Another material that can be widely used with plasmonic materials in nanocomposite form is TiO_2 NP [124-126]. Yang et al. (2021) coated Ag NPs with different thicknesses of TiO_2, and tested these nanocomposites for thiram detection [127]. The authors reported that a thiram detection limit as low as 1.15×10^{-10} M could be reached, as TiO_2 acts not only as a shell but also as a spacer between the plasmonic Ag core and the thiram molecule. It was also confirmed that nanocomposites with shell thickness of about 12 nm have higher SERS performance than those with shell thickness of about 22 nm.

For some SERS applications, plasmonic NPs may need to be coated with chemically inert materials. Normally, the changes in the position of the LSPR bands are observed before and after the aggregation of the plasmonic NPs. These are very useful for not only in SERS but also for various bioanalytical colorimetric studies as colour changes can be observed with the naked eye. However, there are some disadvantages such as adsorbing unwanted biomolecules to the plasmonic surface or desorption of ligands that are not covalently bound on the surface. To eliminate these disadvantages, plasmonic NPs can be coated with inert materials such as SiO_2 to ensure sustainability in SERS applications. The study carried out by Shanthil et al. (2012) is a very good example in this regard [128]. In the study, the effects of approximately 60 nm Ag NPs coated with different SiO_2 shell thicknesses (from 3 to 25 nm), and pyrene signal enhancement were investigated. The results showed that the nanocomposites with the shells

thinner than 15 nm significantly increased the signal, and the nanocomposites with 5 nm shell thickness possessed the best SERS performance (Figure 1.12).

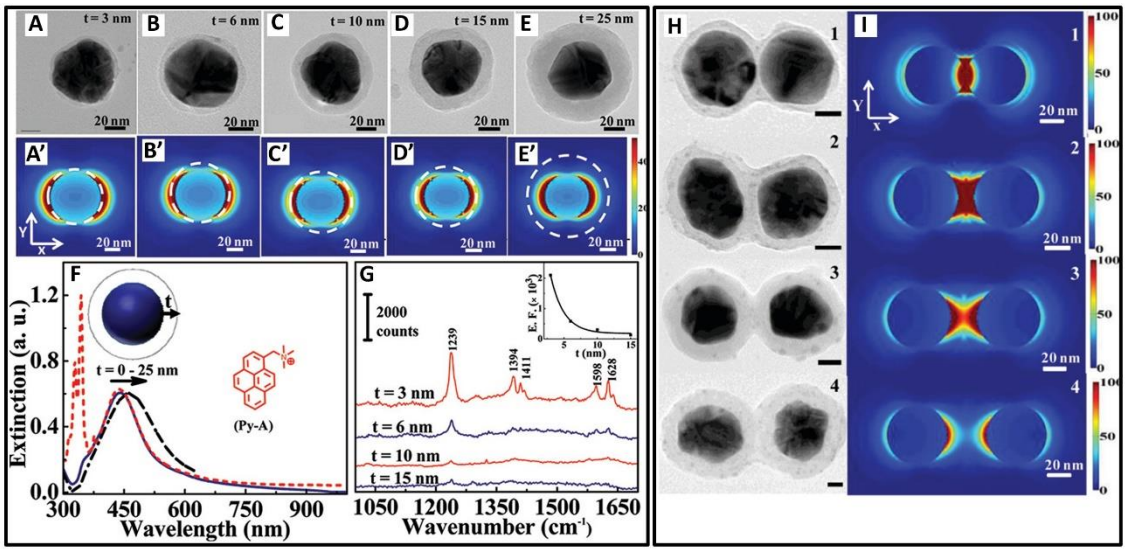

Fig. 1.12. ***(A-E)*** *HRTEM images of $Ag@SiO_2$ nanocomposites with different SiO_2 thicknesses.* ***(A'-E')*** *FDTD simulations of the relative electric field around the corresponding $Ag@SiO_2$ nanocomposites.* ***(F)*** *Extinction spectra of Ag NP (blue solid), $Ag@SiO_2$ NP with 25 nm shell thickness (black dash-dotted), and $Ag@SiO_2$ NP with 3 nm shell thickness after addition of pyrene (red-dotted).* ***(G)*** *SERS spectra of Pyrene with $Ag@SiO_2$ with different shell thicknesses. Inset shows EF plot of 1239 cm^{-1}.* ***(H)*** *HRTEM images of isolated $Ag@SiO_2$ dimers with different shell thicknesses. 1) 6 nm, 2) 10 nm, 3) 15 nm, and 4) 25 nm.* ***I)*** *FDTD simulations of the relative electric field around the corresponding $Ag@SiO_2$ dimers. Adapted with permission from ref. [128]. Copyright 2012, American Chemical Society.*

1.4. Metal-Organic Frameworks

1.4.1. Definition

MOFs are one the extraordinary materials that can be integrated with plasmonic NPs, thus allowing to obtain of highly innovative plasmonic nanocomposites for SERS applications. According to IUPAC recommendation, MOFs are defined as "*a metal-organic framework, abbreviated to MOF, is a coordination network with organic ligands containing potential voids*"[129]. The key feature of MOFs is that polynuclear metal clusters can form strong bonds with organic molecules called *linkers*, revealing crystalline solid lattice structures. Due to the diversity of metal ions in the centre of the structure, and different organic linkers that can bind to it, it is theoretically possible to obtain a solid net or framework with different properties and complexity. At this point, the concept of a secondary building unit (SBU) should also be mentioned. SBU is the most basic building block of MOFs and is also known as metal cluster entities [130]. These metal clusters are linked to each other by functional and branched organic linkers. Depending on the modifications of SBUs or the change in the length of the linkers connected to a selected constant SBU, it is possible to obtain the MOFs with different properties (Figure 1.13).

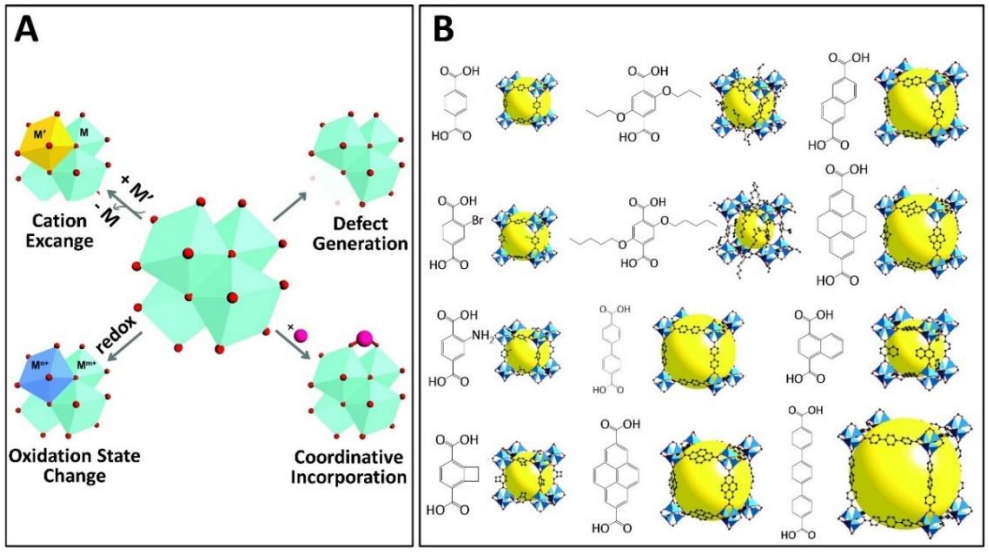

Figure 1.13. (A) *SBUs are easily modified by some post-synthetic methods to obtain MOFs with different properties. Adapted with permission with from ref. [131]. Copyright 2020, Royal Society of Chemistry.* ***(B)*** *The same SBU can be also used with different linkers. Yellow spheres represent the pore size for each MOF. Adapted with permission from ref. [132]. Copyright 2002, The American Association for the Advancement of Science.*

1.4.2. Emergence of MOFs

Although usage and investigation of MOFs have been seen in almost the last two decades, we see that their primitive versions like *Prussian blue* was reported in the 1700s [133]. However, a better understanding of these compounds would come true almost a century and a half from that time with Alfred Werner [134]. In his research, which is that he was trying to explain the nature of chemical bonds in products, Werner obtained yellow ($CoCl_3 \cdot 6NH_3$), purple ($CoCl_3 \cdot 5NH_3$), green ($CoCl_3 \cdot 4NH_3$), and sometimes violet-coloured ($CoCl_3 \cdot 4NH_3$) products when he reacted to $CoCl_3$ with different amounts of NH_3. Accordingly, Werner suggested that the metal ions in these complexes must have two different valences despite the common sense at that time was that every element has one valance and therefore can only have one coordination number. The first of these is the valance, which determines the amount of positive charge of the metal ion in the complex, and the other one determines the number of ligands coordinated to this metal ion. To achieve this result, Werner reacted to cobalt complexes that have different amounts of NH_3 with saturated $AgNO_3$. In this way, the amount of AgCl emerged would directly give the number of NH_3 molecules coordinating with the central cobalt ion:

$$CoCl_3.6NH_3 + AgNO_3 \xrightarrow{Saturated} 3AgCl + Co(NO_3)_3.6NH_3 \quad 1.15$$

$$CoCl_3.5NH_3 + AgNO_3 \xrightarrow{Saturated} 2AgCl + Co(NO_3)_2Cl.5NH_3 \quad 1.16$$

$$CoCl_3.4NH_3 + AgNO_3 \xrightarrow{Saturated} AgCl + Co(NO_3)Cl_2.4NH_3 \quad 1.17$$

As a result, it can be seen that the formula of the complex for equation (1) is actually $[Co(NH_3)_6]Cl_3$. This shows that the central cobalt metal ion is in coordination with 6 NH_3, and therefore it has six secondary valences and three primary valances. For equations (2) and (3), the complexes have the same secondary valences as the previous complex but different primary valences. Werner also tried to understand the geometries of these complexes to take his work one step further. Accordingly, all complexes could have three different geometries such as hexagonal planar, trigonal prismatic, or octahedral, and $[Co(NH_3)_6]Cl_3$ and $[Co(NH_3)_5Cl]Cl_2$ complexes with any of these geometries would not have any isomers either. However, $[Co\ (NH_3)_4Cl_2]Cl$ could have three different stereoisomers for hexagonal planar and trigonal prismatic geometry, and two different isomers for octahedral geometry. Indeed, since

he obtained two different colours (green and violet-coloured) isomers for $[Co(NH_3)_4Cl_2]Cl$ in his experiments, Werner suggested the basic geometry for the complex is octahedral.

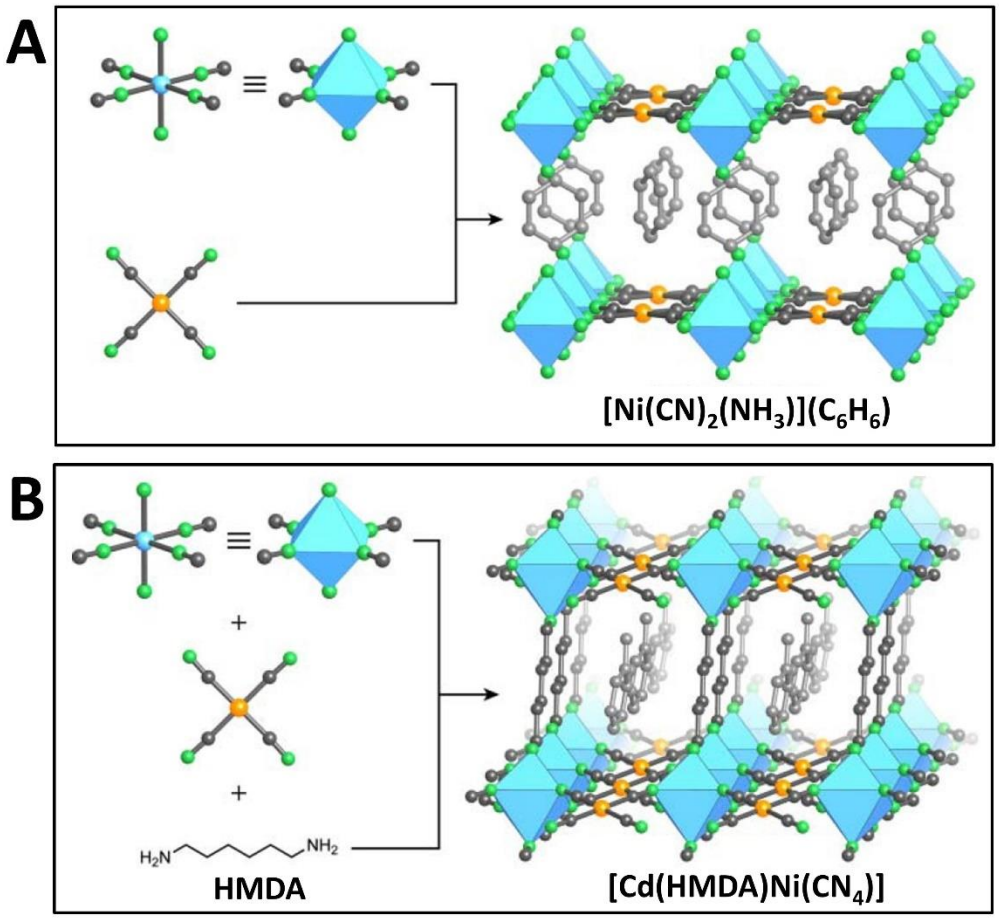

Figure 1.14. *Schematic representation of* ***(A)*** *Hofmann clathrates, and* ***(B)*** *Linking the clathrates with HMDA and arranging them as 3D structures. All hydrogen atoms are omitted for clarity. Colour code: cadmium, blue; nickel, orange; nitrogen, green; carbon, gray. Guest molecules are represented as light gray. Adapted with permission from ref. [135]. Copyright 2019, John Wiley and Sons.*

Werner's demonstration of how the metal ion in the complexes can coordinate with other atoms sheds light on further innovative works. Indeed, in 1897, Karl Andreas Hofmann synthesized the first coordination compound, known today as *Hofmann Clathrates*, which exhibits 2D morphological properties unlike the complexes of Werner with 0D morphology [136] (Figure 1.14A). In 1984, Iwamoto et al. completely changed the composition of the octahedral complex in the compound, and added another complex with the same geometry but has divalent Cd atom in the centre and diaminoalkane ligands attached to it [137]. Thus, just as in the original Hofmann clathrate, the octahedral complexes were linked to each other

by square planar $Ni(CN_4)$ complexes. The 3D arrangement of the layers was revealed as a result of the binding of the terminal N atoms in the octahedral complex with HMDA. In this coordination compound with a new arrangement, structural collapse problems were eliminated, and a 3D arrangement was obtained that allows encapsulation of various guest molecules (Figure 1.14B).

Saito et al. managed to obtain the networks with different morphologies in the compound based on the Cu^+ ion, simply by changing the length of the linker [138-140]. For this, they used dinitrile linkers with different lengths such as SUC, GLU, and ADI to obtain coordination networks with 1D, 2D, and 3D morphology, respectively, according to the length of the linkers (Figure 1.15). Among the structures, $[Cu(ADI)_2](NO_3)$ has special importance as it is the first reported 3D network.

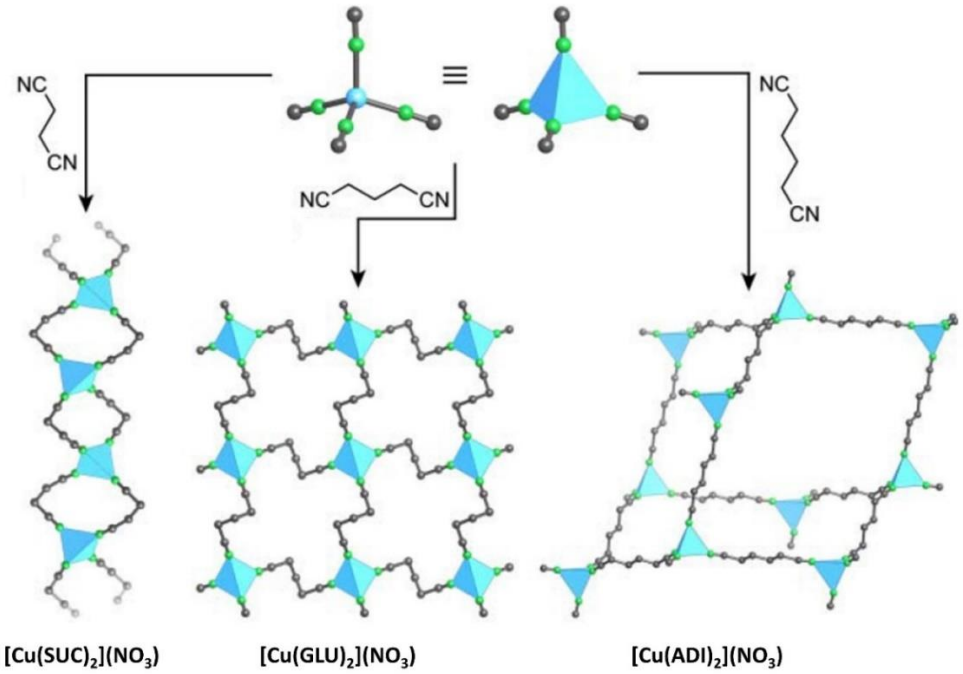

Figure 1.15. *Structures of coordination networks include dinitriles with different lengths linked Cu^+. All hydrogen atoms are omitted for clarity. Colour code: copper, blue polyhedra; carbon, gray; and nitrogen, green. Adapted with permission from ref. [135]. Copyright 2019, John Wiley and Sons.*

After the first demonstration of 3D networks and various experiments with different metals and linkers, finally In 1995, Omar M. Yaghi and his co-workers, who have made a great contribution to coordination networks with their studies and the different materials they have

produced, brought the term MOF to the literature for the first time, and more than 25 years since that time, MOFs with different compositions and topologies for various purposes continue to attract attention.

1.4.3. Properties of MOFs

1.4.3.1. Porosity

According to IUPAC recommendation, porous materials are classified under three different categories: (1) microporous, (2) mesoporous and (3) macroporous materials [141]. Consequently, the pore widths of microporous materials are less than 2 nm. Mesoporous materials have pore widths between 2 and 50 nm, while this width is greater than 50 nm for macroporous materials.

Generally, adsorption isotherms of porous materials are carried out with the help of inert probe gases such as N_2 or Ar. The adsorption data obtained as a result of the interaction of these gases with the porous materials are presented in the form of the *quantity of adsorbed gas* plotted against the *relative pressure*, and is called a *physisorption isotherm* [142]. These isotherms have been categorized by IUPAC in different ways, ranging from type 1 to type 6 [141] (Figure 1.16A). MOFs are microporous materials associated with type I isotherm due to their general characteristic structure. Accordingly, these types of materials generally have very high surface areas and a narrow pore size distribution.

1.4.3.2. Specific Surface Area

Data from N_2 adsorption/desorption isotherms are used to calculate specific surface areas of porous materials. The specific surface area is the surface area per 1 g of material and is expressed in m^2/g. Generally, to calculate this area, some points taken from the isotherm are interpreted with the BET calculation, and the resulting data is called the BET surface area (S_{BET}). Another expression method is the Langmuir calculation, and the output is called the Langmuir surface area ($S_{Langmuir}$). Shortly, the difference between the two calculation methods is that the Langmuir model assumes adsorbed molecules as a monolayer. On the other hand, the BET model assumes that these molecules are adsorbed as a multilayer. While types II and IV isotherms are used for Langmuir modelling; types I, III and V are used for BET modelling. Because MOFs are microporous materials that perfectly match type I isotherm, S_{BET} is taken

into account when calculating their specific surface area. All of the MOF species introduced in the literature so far, there are no species with a specific surface area of less than 1000 m^2/g. Figure 1.16B shows different MOFs with different amounts of S_{BET} introduced to date.

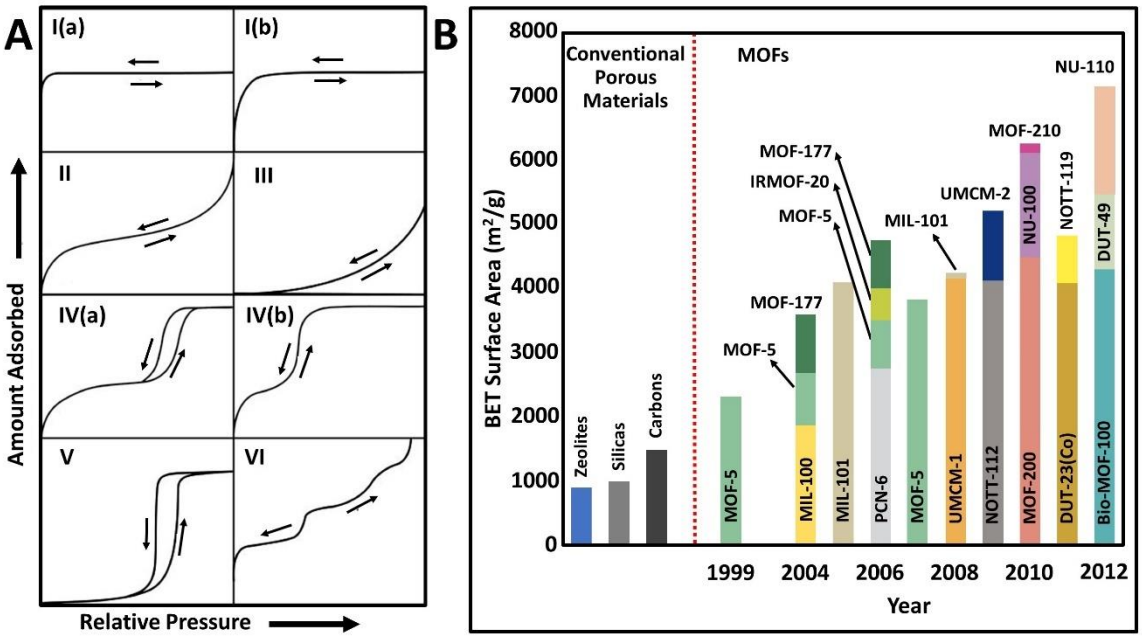

Figure 1.16. (A) *Classification of physisorption isotherms according to IUPAC. Adapted with permission from ref. [141].* ***(B)*** *Chart of MOFs with the highest S_{BET} values. Adapted with permission from ref. [143]. Copyright 2013, The American Association for the Advancement of Science.*

1.4.3.3. Stability

It can be evaluated the stability of MOFs in two parts as chemical and physical stability. Chemical stability can be defined as the retention of chemical composition and permanent porosity of MOFs when exposed to water, acid, alkali or salt solutions [144]. This is closely related to the strength of the bond between the MOF metal clusters and the linkers or the environment surrounding the MOFs [145]. Correct adjustment of metal-linker bonds, connectivity, geometry, size, and even hydrophilic/hydrophobic properties of MOFs are the most important factors that increase their chemical stability [144-146]. On the other hand, the physical stability of MOFs is directly related to their mechanical strength. Factors such as tension, compression, abrasion, attrition, and pressure changes must be taken into account when determining the mechanical strength of MOFs [147-149]. All these factors profoundly affect the properties of MOFs such as gas sorption, sensing, molecular sieving and catalysis,

and the applications they are used in. In a study on the resistance of MOFs to physical forces, Moggach et al. (2009) tested the crystal structure stability and pore diameter changes of the zeolitic imidazolate framework-8 (ZIF-8) under high pressure [150]. The results showed that the structure can maintain its stability against the increase in pressure and with this pressure, both nanopore and unit cell volume can be increased (Figure 1.17). Moreover, the authors suggested that these kinds of changes in the structure would be an advantage and thus, more gas and solvent can rush into the structure.

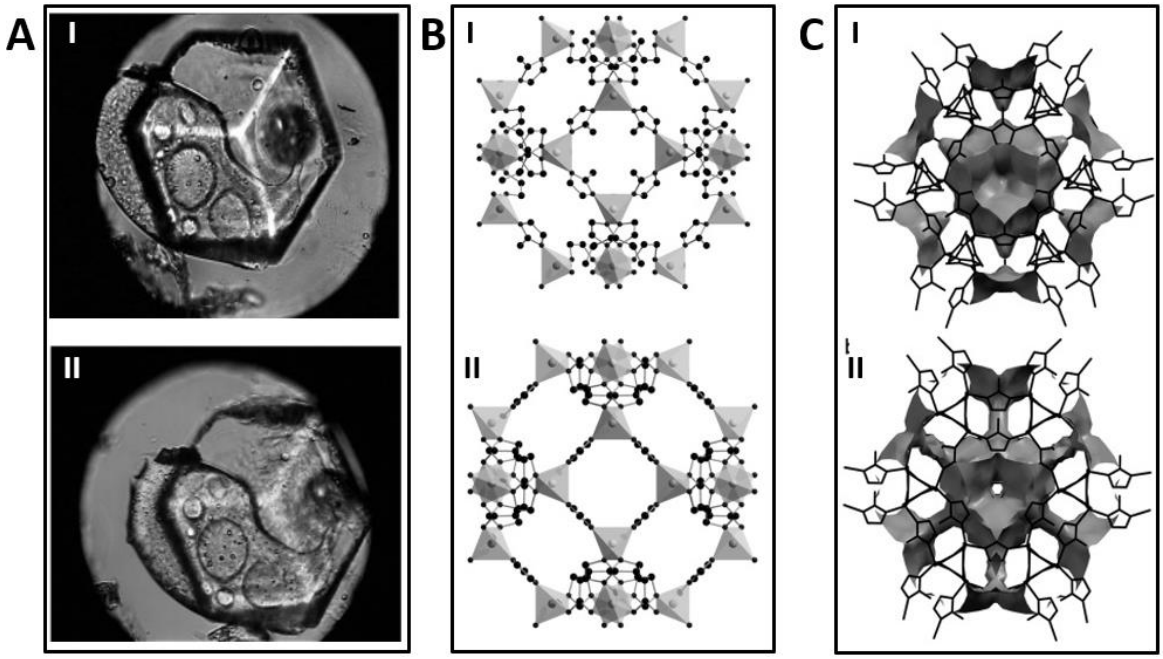

Figure 1.17. (A) Optical images of a single ZIF-8 crystal under ambient pressure (I) and 1.47 GPa (II). (B) The modelling of the changing of packing arrangements of ZIF-8 under ambient pressure (I) and 1.47 GPa (II). (C) The modelling of the changing of voids of ZIF-8 under ambient pressure (I) and 1.47 GPa. Adapted with permission from ref. [150]. Copyright 2009, John Wiley and Sons.

1.4.4. Plasmonic-MOF Nanocomposites

The integration of Novel MOF structures with plasmonic NPs and the resulting plasmonic-MOF nanocomposites have removed many limitations in terms of SERS applications and created new opportunities. Because such nanocomposites are porous, have ultra-high surface areas, and interact more with target molecules, they are seen as a valuable tool for improving the performance of SERS substrates [151]. In particular, due to the sieving effect

and hydrophobic nature of MOFs, the detection limits of various analytes can be decreased depending on the type of MOF used.

The metal ions such as Cr^{3+}, Fe^{2+} or Fe^{3+}, Zn^{2+} and Zr^{4+} can be used in the preparation of different plasmonic-MOF nanocomposites. In this way, different metal ions yield different geometries such as tetrahedral, trigonal bipyramidal square, or pyramidal octahedral due to different coordination sites [152]. On the other hand, the chemical and structural diversity of organic linkers further increases the customizability of the nanocomposites. The most important aspect for the effective use of a plasmonic-MOF substrate for different SERS applications is that the nanocomposite must be high stability and that the pore profile must be suitable for most analytes. Therefore, MOF structures such as ZIF-8 or ZIF-67, IRMOF (Isoreticular metal-organic frameworks or MOF-5), UiO-66 or UiO-67 (UiO, Universitetet i Oslo), and MIL-101 (MIL, Matérial Institut Lavoisier) are ideal for a variety of SERS applications. In addition, MOFs with wider aperture sizes such as NU-901 (NU, Northwestern University) have also been used for SERS studies in recent years. Figure 1.18 shows the SERS substrates obtained as a result of the cooperation of MOFs mentioned with plasmonic NPs in various SERS studies.

MOF-5 [$Zn_4O(BDC)_3$] (BDC: 1,4-benzodicarboxylate), also known as IRMOF-1, is a type of MOF that can be preferred for SERS applications because of its high surface area (S_{BET}: 2500-3000 m^2/g). However, due to the fact that the Zn-O bond in the structure is sensitive to hydrolysis and therefore the structure is deteriorated, it has not found a place for itself in various applications very often. Nevertheless, its use is encountered in some SERS studies. In one of these studies, Guselnikova et al. (2019) used a SERS substrate consisting of Au surface and MOF-5 for the detection of organophosphorus pesticides (Figure 1.18A) [153]. The results showed that the composite could detect pesticides such as paraoxon and fenitrothion up to 10^{-12} M, and it was reported that the detection limit could be reduced thanks to MOF-5.

Another type of MOF that is studied in the field of plasmonics is UiO-66. It is obtained as a result of coordinating $Zr_6O_4(OH)_4$ metal clusters with BDC linkers and preferred due to its high chemical and thermal stability for SERS applications. In one study, Xu et al. (2021) used UiO-66@Ag NP nanocomposites to perform sensitive SERS detection of DEHP in plastic samples (Figure 1.18B) [154]. For this purpose, the authors grew Ag NPs on the surface of UiO-66 and reported that Ag NP aggregation was reduced and hotspots between NPs were increased due to the high surface area and porous structure of UiO-66. Moreover, DEHP was

adsorbed by the nanocomposite quite well, and SERS detection results showed that the detection limit was 3×10^{-12} M. In another study, Fu et al. (2021) introduced two different SERS substrates consisting of UiO-66 and Au NPs for the analysis of food samples [155]. Among these substrates, the nanocomposite composed of UiO-66/Au NP was used for detection of carcinogenic MeIQ, and the other substrate, UiO-66(NH_2)/AuNPs/Nylon-66 membrane, was used for enrichment, separation, and SERS-based detection of Sudan Red 7B. The results showed that both nanocomposites were highly successful SERS substrates and the detection limits of MeIQ and Sudan Red 7B were calculated as 1.18 μg/L and 0.49 μg/L, respectively. On the other hand, Li et al. (2022) showed that SERS-based detection of an antibiotic such as TTC is possible with the plasmonic-UiO-66 nanocomposite (Figure 1.18C) [156]. For this, firstly, UiO-66(NH_2) was prepared, and its pores were filled with methylene blue and Au NPs. Then, the MOF was functionalized with via TTC-specific aptamer that acts as a *molecular gate*. Thus, SERS-based TTC detection from the supernatant was designed as the aptamer opens the MOF pores in the presence of TTC, and methylene blue and Au NP are released from the pores. The results showed that the detected TTC concentration was correlated with methylene blue, and Au NPs released from the pores, and the calculated detection limit for TTC was 0.01 ng/mL.

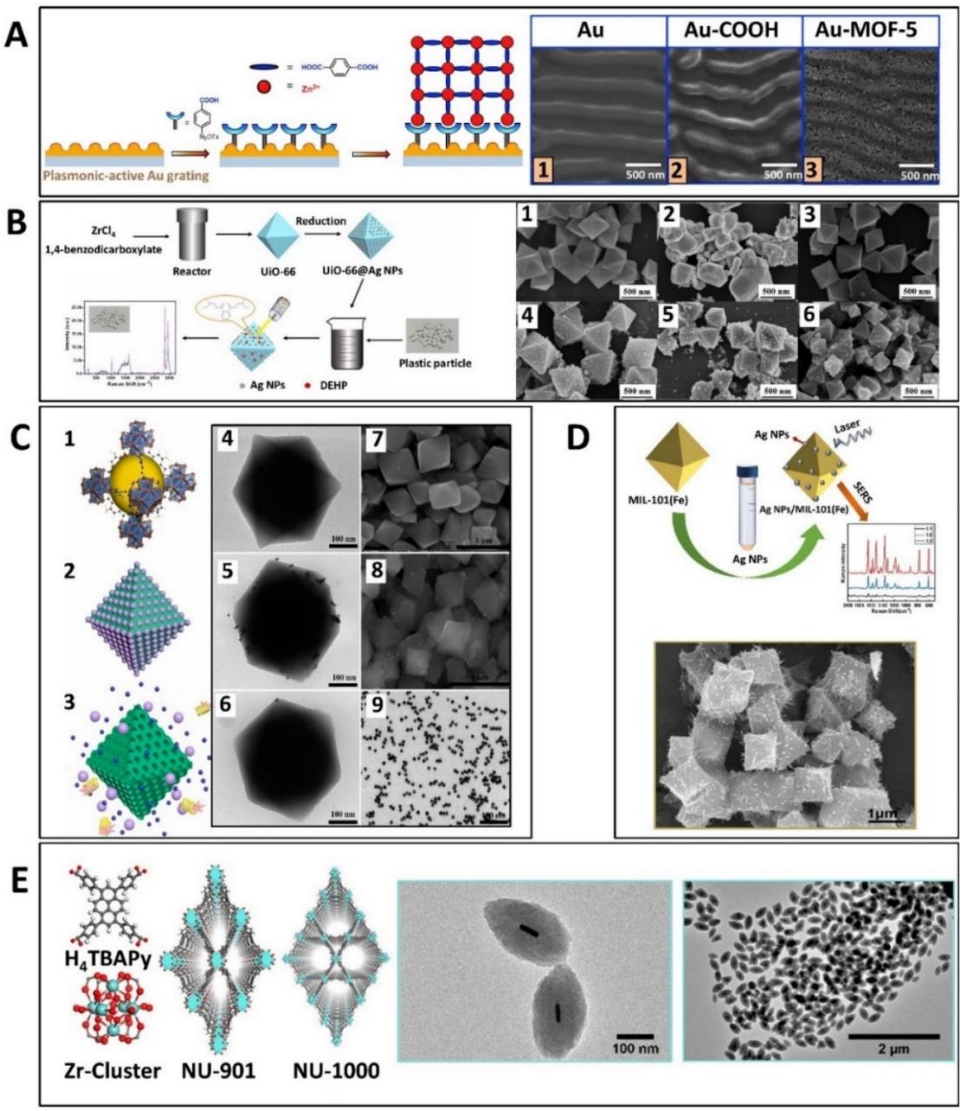

Figure 1.18. Examples of plasmonic-MOF nanocomposites. ***(A)*** *Schematic illustration of preparing of Au-MOF-5 SERS substrates, and SEM images of the substrate surfaces: 1) Au, 2) COOH-modified Au, and 3) Au-MOF-5. Adapted with permission from ref. [153]. Copyright 2019, Elsevier.* ***(B)*** *Schematic illustration of preparing of UiO-66@Ag NPs, and SEM images of (1) UiO-66, and (2) Ag NPs, different proportions of UiO-66 and Ag NPs (3) 1:1, (4) 1:2, (5) 1:3, and (6) 1:4. Adapted with permission from ref. [154]. Copyright 2021, Elsevier.* ***(C)*** *Schematic illustration of (1) UiO-66(NH_2), (2) MOFs@AuNPs@Methylene blue, (3) MOFs@AuNPs@Methylene blue@Aptamer@TTC, (4-6) Corresponding TEM images, and (7-9) SEM images of the nanocomposites. Adapted with permission from ref. [156]. Copyright 2022, Elsevier.* ***(D)*** *Schematic illustration of preparing of Ag NPs/MIL-101(Fe), and the inset shows to corresponding TEM images of the nanocomposites. Adapted with permission from ref. [157]. Copyright 2021, Elsevier.* ***(E)*** *Schematic illustration of H_4TBAPy linker, Zr-cluster, the structure of NU-901 and its "sister", NU-1000. The Insets show to corresponding TEM images of Au NR@NU-901. Adapted with permission from ref. [158]. Copyright 2019, American Chemical Society.*

MIL-101 is a type of MOF that contains BDC and Cr^{3+}, Fe^{2+} or Fe^{3+}, as linkers and metal ions, respectively. Due to its high surface area, biocompatibility, and non-toxic properties, MIL-101(Fe) is the MOF that can be used together with plasmonic NPs to give a powerful SERS substrate for many applications. Fu et al. (2020) reported that they could detect toluene up to 2.5 ppm with MIL-101(Fe) alone, but this limit could be reduced to 0.48 ppb when Au NPs were embedded onto the MOFs [159]. In another study, MIL-101(Fe) decorated with Ag NPs was able to detect Paraquat, an herbicide, up to 10^{-12} M (Figure 1.18D) [157]. On the other hand, MIL-101(Cr), which is the structural analogue of MIL-101(Fe), finds its place in various SERS studies although it is has toxic nature. In one of these studies, Wang et al. (2020) decorated NH_2-MIL-101(Cr) with Au NPs and investigated the adsorption and SERS detection of acid orange (II) [160]. The results showed that the substrate has high adsorption performance and can detect acid orange (II) up to 0.05 ppm. In another study, MIL-101(Cr) film was prepared and it was ensured that Ag^+ was reduced to Ag NPs on the material by UV irradiation [161]. In this way, ABT and nitrofurantoin could be detected up to 10^{-11} M and 10^{-7} M, respectively.

NU-901, a Zirconium-MOF, has been used in the coating of various plasmonic NPs and SERS applications in the last 3 years due to its high surface area and wide aperture size that allows the passing of analytes have especially large dimensions. In this type of MOF, Zr^{4+} ions are connected by H_4TBAPy linkers, resulting in MOFs with *scu* lattice topology. These kinds of novel plasmonic@NU-901 nanocomposites were tested in various SERS applications, especially after Prof. Omar K. Farha and his co-workers showed that coating of plasmonic NPs with NU-901 is possible, and this kind of MOF has different pore profile than its "*sister structure*", NU-1000 (Figure 1.18E) [158]. In one of these studies, Xia et al. (2021) decorated Au NRs with QDs via electrostatic interactions and then coated these NPs with NU-901 to produce bimodal sensors that could detect volatile benzaldehyde with the help of fluorescent and SERS methods [162]. The results showed that gaseous benzaldehyde is easily captured by the MOF, and SERS detection of benzaldehyde at sub-ppb level is possible with ABT-modified Au NR. The authors also reported that the detection limit calculated from the fluorescent and SERS method was 1.2 and 0.1 ppb, respectively. In another study, Huo et al. (2022) coated thiol-magenta modified Ag NPs with NU-901 and performed colorimetric and SERS-based detection of SO_2 [163]. The results shows that this type of dual-mode strategy is highly suitable for SO_2 detection in various samples.

1.5. Zeolitic Imidazolate Frameworks

ZIFs are undoubtedly one of the most popular MOFs that can be used together with plasmonic NPs in various SERS applications, resulting in novel SERS substrates. They are a sub-group of MOFs made up of M-Im-M moieties [164] and here, *M* represents a metal ion such as Zn^{2+} or Co^{2+} and *Im* represents imidazolate linker. The way the metal ion and the linker are bonded to each other is similar to Si-O-Si bonds, and they are connected at an angle of about 145° just like them [150]. Therefore, lattice topologies are quite similar to zeolites. MOFs belonging to the ZIF sub-group have different lattice topologies, and ZIF variants with these topologies such as *poz*, *RHO*, *LTA*, *moz*, *SOD*, *GME*, *MER*, *ANA* and *GIS* have been well defined in the past years [165] (Figure 1.19). To obtain ZIFs with these kinds of topologies, it is usually sufficient to change the type of imidazolate or the solvent used during synthesis [166, 167].

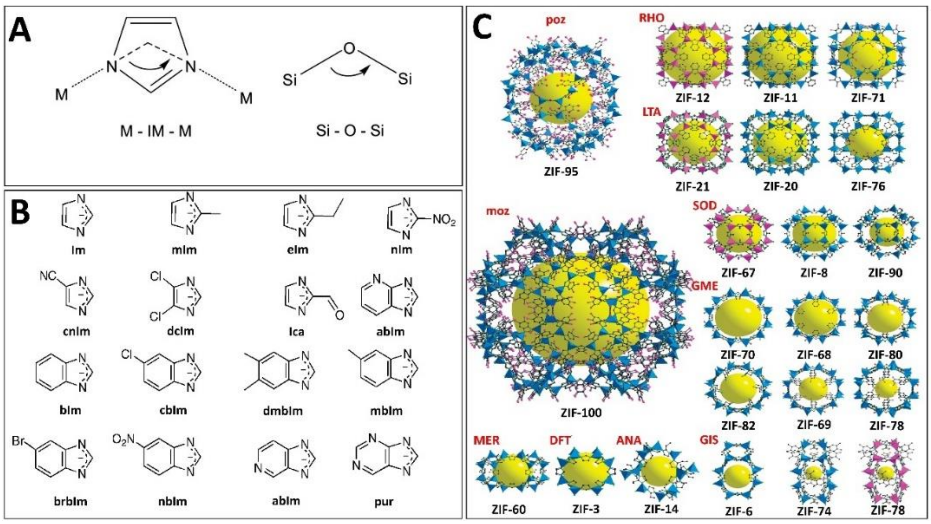

Figure 1.19. *Schematic representations and different structures of ZIFs.* ***(A)*** *The similarity between Si-O-Si bonds in zeolites and M-Im-M bonds in ZIFs.* ***(B)*** *Different imidazolate linkers that can be used for different kinds of ZIFs. (Im: Imidazole, mIm: 2-Methylimidazole, eIm: 2-Ethylimidazole, nIm: 2-Nitroimidazole, cnIm: 1H-Imidazole-4-carbonitrile, dcIm: 4,5-Dichloroimidazole, Ica: Imidazolate-2-carboxyaldehyde, abIm: 4-Azabenzimidazole, bIm: Benzimidazole, cbIm: 5-Chlorobenzimidazole, dmbIm: 5,6-Dimethylbenzimidazole, mbIm: 5-methylbenzimidazole, brbIm: 5-Bromo-1H-benzimidazole, nbIm: 5-Nitro-1H-benzimidazole, and pur: Purine).* ***(C)*** *Crystal structures of ZIFs with different linkers. Yellow spheres represent the pore size of the structures. Blue and purple represent zinc and cobalt metals, respectively. Adapted with permission from ref. [165]. Copyright 2010, American Chemical Society.*

In the early 2000s, due to the lack of stability of MOFs such as IRMOF series, the roles in various applications were quite limited and they received various criticisms about this issue [168]. To dispel this bad impression, Lee et al. (2002) synthesized a zeolite-like MOF ($Co_5(Im)_{10}\cdot 2MB$, MB stands for 3-methyl-1-butanol) which has surprisingly high stability and *nog* lattice topology formed by the coordination of tetrahedral Co^{2+} metal ions with four imidazole linkers [169]. For a short time, this MOF was more popular than its predecessor MOF structures such as IRMOF-1. However, this effort was not sufficient since the structure was not very open, and the functionality of its structural features was limited. [170]. Another MOF type $[Zn(bIm)_2]\cdot(H_2O)_{1.67}$, introduced in 2003, just a year later, was considered to be the first ZIF type synthesized due to its *SOD* lattice topology [171]. In 2006, Prof. Xiao-Ming Chen's research group synthesized three different zeolite-like MOFs with molecular formulas $[Zn(mIm)_2]$, $[Zn(eIm)_2]$ and $[Zn(eIm/mIm)_2]$ [172] and reported that these MOFs have *SOD*, *ANA*, and *RHO* lattice topologies, respectively. In a rivalry with Chen's group, Prof. Omar M. Yaghi's group also synthesized twelve different zeolite-like MOFs just six months later [164] and named these MOFs as *ZIFs*. On the other hand, Chen's group named these MOFs as "*metal-azolate frameworks (MAFs)*". However, ZIF nomenclature was academically accepted because some of the MOFs synthesized by Chen's group were nearly incapable of N_2 adsorption ($Zn(eIm)_2$, S_{BET}: $28m^2$) and were less interesting than the MOFs produced by Yaghi's group. Later, ZIF nomenclature was also accepted by Chen's group.

In recent years, ZIFs have been frequently preferred and became popular due to their easy synthesizing, large pore sizes and easy integration with plasmonic NPs to produce nanocomposites. When looking at the various studies on MOFs, there are approximately 150 variants of ZIFs among the 20000 reported MOFs, and yet one out of every three studies examines MOFs belonging to the ZIF sub-group [168]. Among these ZIFs, ZIF-8 and its cobalt isomorph ZIF-67 stand out one step further.

1.6. ZIF-8

1.6.1. Definition

ZIF-8 [$Zn(mIm)_2$] (mIm: 2-methylimidazole) has the *SOD* lattice topology and is the most well-known of the MOFs belonging to the ZIF sub-group. It contains 276 atoms in each unit cell and crystallizes in the $I\bar{4}3m$ cubic space group with a lattice constant of 16.992 Å [173]. Each Zn^{2+} metal ion has four secondary valances, and therefore coordinates with four mIm to form ZnN_4 clusters which is the SBUs of ZIF-8. These SBUs are then connected by mIm linkers to give the *SOD* crystal structure with a pore size of 11.6 Å and a pore opening of 3.4 Å. (Figure 1.20).

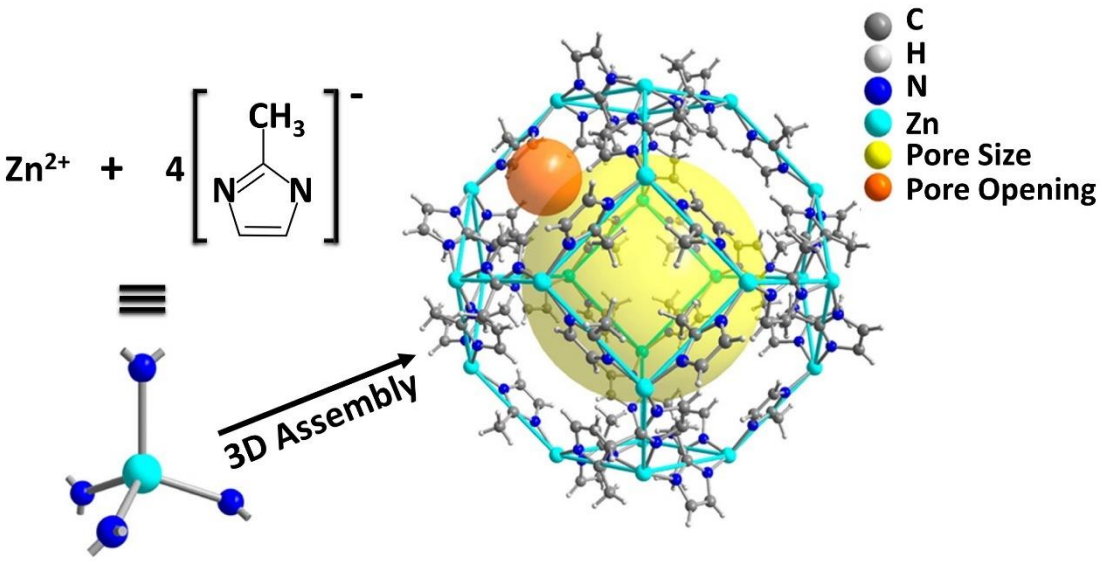

Figure 1.20. *Schematic illustration of coordination between Zn^{2+} metal ion and mIm linker to give ZIF-8 MOF with SOD lattice topology. Yellow and orange spheres represent the pore size and opening of ZIF-8, respectively. Adapted with permission from ref. [174]. Copyright 2017, Elsevier.*

1.6.2. Properties of ZIF-8

In the determination of structural properties of the ZIF-8, 2-methylmimidazole linker has a vital role. As previously shown in figure 1.19, there are different types of ZIFs resulting from the interaction of imidazole rings that have different functional groups with zinc metal ions. Some of these, such as 2-ethylimidazole, cause the emergence of non-porous ZIFs, while mIm or some of the other functional imidazole rings result in ZIF variants with different pore

size, pore opening, or different chemical and physical stabilities. On the other hand, the position of the methyl functional group in the imidazole ring is also very important. Although 1-methylimidazole and 2-methylimidazole have the same chemical formula, 1-methylimidazole does not contribute to crystal formation. However, it was shown that it acts as a modulator which directly effects of size and morphology regulation of the MOFs such as ZIF-4 [$Zn(Im)_2$] [175]. Another important point is that the methyl group in 2-methylimidazole make ZIF-8 hydrophobic. A large number of methyl groups in the structure causes both the interior and exterior of the framework to show no affinity for water, unlike zeolites.

Various studies carried out in the past years reported that ZIF-8 is a material with excellent thermal and chemical stability [176, 177]. As Yaghi and his co-workers showed, TGA results indicate that in inert atmosphere, ZIF-8 maintains its physical stability up to 550^{o}C [164]. However, some doubts arise about the long-term thermal stability of ZIF-8, when considering the high temperatures, pressures, and inert atmospheres in industrial processes. Indeed, Yin et al. (2015) examined the thermal stability of ZIF-8 from their perspective [178]. Accordingly, ZIF-8 maintained its stability in an inert atmosphere for 24 hours at 300^{o}C and for 5 hours at 400^{o}C. On the other hand, the stability was maintained at 200^{o}C for 24 hours and at 300^{o}C for 5 hours in an air atmosphere. The worst stability performance was encountered in the stream atmosphere, and the authors reported that the thermal stability of ZIF-8 strongly depends on atmospheric conditions and exposure time. There are some attempts to increase the thermal stability of ZIF-8, and these are generally based on post-modification methods. On the contrary, performing pre-modifications to increase the thermal stability of ZIF-8 can be preferred. In one of the studies on this, Wang et al. (2020) increased the thermal stability and CO_2 adsorption properties of ZIF-8 through PANI, and reported that the thermal stability can be increased up to 632.71^{o}C. [179].

The chemical stability of ZIF-8 was well-reported when it was first introduced [164]. According to this, ZIF-8 was kept in different boiling solvents for seven days and was not physically degraded during this period. In particular, the fact that ZIF-8 remained unhydrolyzed in water is a rather surprising and contradictory result with later published studies. Because it was shown very well that the structure of ZIF-8 can be hydrolysed even under room temperature (Figure 1.21).

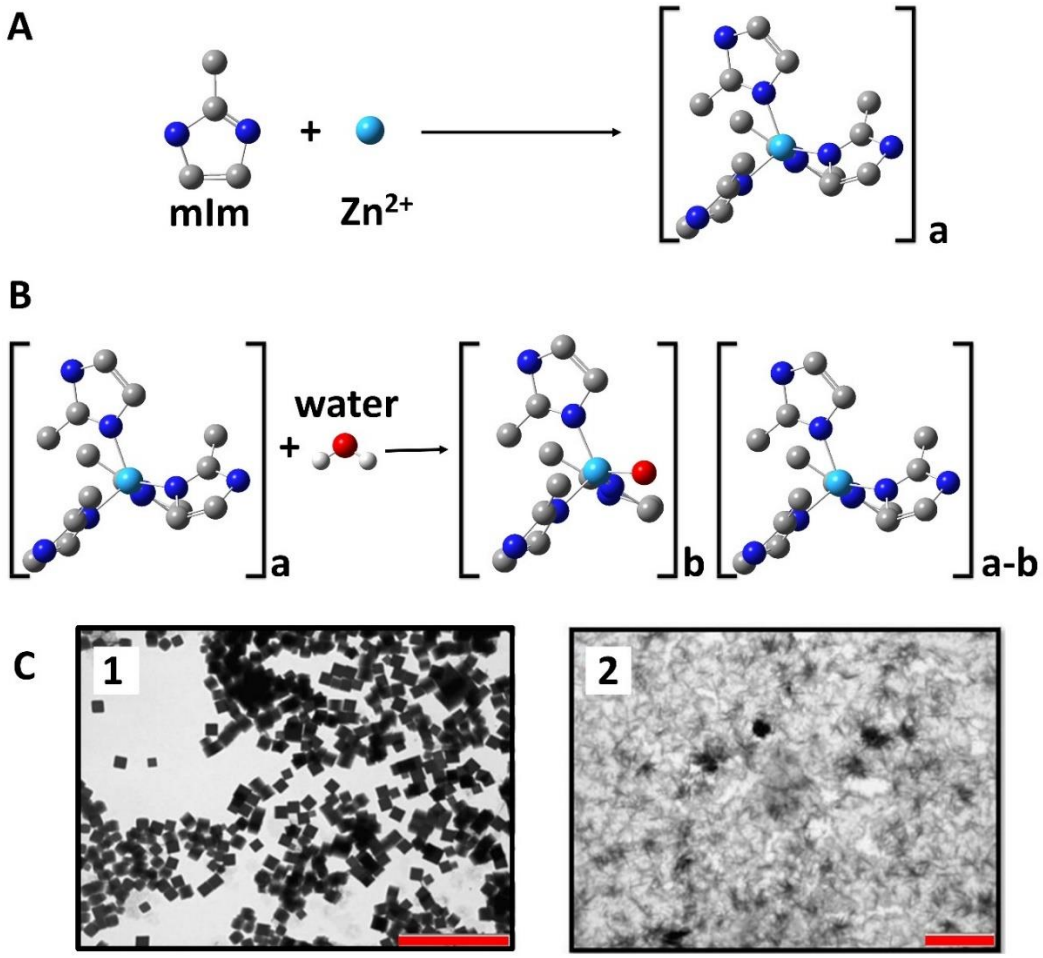

Figure 1.21. *Schematic representation of hydrolysis process of ZIF-8.* ***(A)*** *During synthesis, four 2-methylimidazole rings and one zinc metal ion combine to form SBUs of ZIF-8.* ***(B)*** *However, this structure is generally stable in organic solvents such as methanol, ethanol, or acetone, depending on the type of zinc precursor. If the ZIF-8 crystals interact with water, OH^- ions attack the bond between the linker and the metal ion, damaging the integrity of the structure. As a result, while "b" amount of water molecules interacting with "a" amount of SBU causes the same amount of deformed SBU to form, "a-b" amount of SBU leaves this process unharmed.* ***(C)*** *TEM images show the effect of the process on ZIF-8 crystals before (1) and after (2). Red bar is the scale with 2 µm.*

ZIF-8 is known as a special material in drug delivery applications due to its porous structure and high absorption capacity [180-183]. Besides, ZIF-8 can release its cargo (drug, enzyme, amino acid, etc.) in the desired region, thanks to its degradation in acidic [184] and aqueous solutions [185, 186], and losing its physical integrity. One of the biggest reasons for this is the pH-dependent ionization of the imidazole linker and the reversible coordination with metal ions [187]. The degree of hydrolysis is variable in different environments. In a study, the

degradation profile of ZIF-8 was investigated in widely used different cell culture mediums (DMEM, MEM, opti-MEM, α-MEM, 199, IMDM, RPMI-1640 and L-15) [188]. The results showed that ZIF-8 was degraded in all cell culture mediums, but the extent of this was dependent on the type of culture medium. Another study also reported that the light may be another factor that can degrade ZIF-8 [189]. Normally, under normal conditions, the light is not capable of degrading ZIF-8. On the other hand, according to the study, if ZIF-8 particles are added to water and exposed to light illumination at the same time, then the light could accelerate the hydrolysis of ZIF-8.

In the ground-breaking study by Yaghi and his co-workers, it was underlined that some ZIF types are more stable than others Accordingly, ZIF-8 has higher stability than ZIF-11, and ZIF-11 can degrade in a much shorter time under the same conditions (e.g. in aqueous solution), and transform into a different crystalline material after the third day [164]. This reveals, however, that ZIF-8 is one of the most stable ZIF variants.

1.6.3. The Factors Affecting Crystallization and Morphology of ZIF-8

Before looking at the general crystal structure of ZIF-8, it should to be understand how inorganic and organic materials crystallize. According to Gibbs' theory of heterogeneous phase equilibrium, for a crystal to be in equilibrium, it must be positioned at a minimum total surface area times total surface free energy [190]. On the other hand, Curie suggested that the rate of crystal surface growth is proportional to the surface free energy [191]. Then, Wulff stated that for the equilibrium, the central distances (h_i) of the crystal faces from a selected point (Wulff point) of the crystal are proportional to the specific surface free energy (γ_i) associated with that crystal face ($\gamma_i / h_i = constant$) [192]. These propositions about crystal growth led us to the well-known "*Gibbs-Curie-Wulff theorem*".

There is a basic difference between the crystal growth of inorganic and organic materials. Accordingly, the components that make up the Inorganic materials are usually "spherical" and therefore, no orientation difference is observed during growth. However, organic molecules are more complex than components of inorganic materials, and orientation differences are likely [193]. Consequently, crystals formed by organic molecules must thermodynamically adjust their morphology according to the lowest surface free energy, following the Gibbs-Curie-Wulff theorem. Since these organic molecules in the crystal are held

together by non-covalent interactions such as van der Waals or weak hydrogen bonds, they can switch to different crystal morphologies by being rapidly affected by low surface free energy changes arising from various factors [194] (Figure 1.22A and B).

According to the theorem, crystal growth of ZIF-8 begins with the formation of cubes revealing six (100) faces. This crystal grows into a truncated rhombic dodecahedron (TRD) revealing six (100) and twelve (110) directions. Finally, the growth of ZIF-8 terminates in the more thermodynamically stable rhombic dodecahedra (RD) in which the (100) faces disappear and only twelve (110) faces remain, by the theorem (Figure 1.22C) [195].

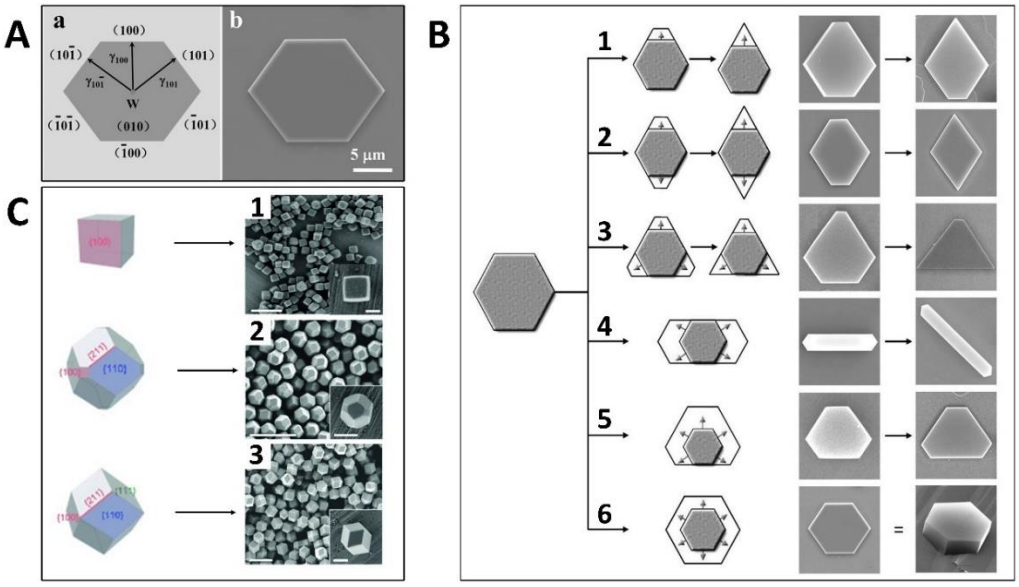

Figure 1.22. (A) Representation of Wulff construction of a crystal, DBTDT, viewing along the b direction (a), and SEM image of the representative crystal viewing along the b direction. (B) Schematic illustration and SEM images of the growing of the crystal shapes according to the theorem. The crystal can grow according to six different possible routes from 1 to 6. Adapted with permission from ref. [193]. Copyright 2015, John Wiley and Sons. (C) Schematic illustration and SEM images of crystal growth of ZIF-8. From 1 to 3 represent the taken SEM images of the different stages from the growth process. 1: Cubic, 2: TRD, and 3: RD. Adapted with permission from ref. [195]. Copyright 2015, John Wiley and Sons.

Generally, when be looked up the factors affecting the size and morphology changes of ZIF-8 crystals, we first encounter the differences in the ZIF-8 synthesis methods. The common methods for the synthesis of ZIF-8 are based on the solvothermal and hydrothermal approaches [196-198], which are generally traditional methods. Apart from these, the

synthesis methods such as mechanochemical and sonochemical, were also proposed [199, 200].

The temperature is vital for ZIF-8 crystallization and therefore, it is effective on pore morphology and size, and crystal size. A study showed that the size of ZIF-8 crystals in nanoparticular form changes from 78 nm to 26 nm at temperatures ranging from -15^{o}C to 60^{o}C respectively, and due to the decreasing size, there is an increase in the surface area [201]. In another study, the importance of the temperature used during the synthesis of ZIF-8 was demonstrated with the help of the counter diffusion method through the propylene/propane separation application [202]. The results revealed that the ZIF-8 membrane thicknesses decreased from 70 µm to 40 µm with increasing temperatures and the best separation efficiency was achieved with the ZIF-8 membrane synthesized at 100^{o}C.

Apart from temperature, the solvent in which the synthesis is carried out also influences ZIF-8 morphology and phase crystallinity. Bustamente et al. (2014) demonstrated this effect very well in their study [203]. In the study, they reported that there were differences in the reaction rates and resulting crystal sizes of ZIF-8s synthesized in different types of aliphatic alcohols, water, DMF and acetone, and that the differences were due to the different hydrogen bond donation capacities of the solvents used. Malekmohammadi et al. (2019) also examined the effects of solvent and other parameters on ZIF-8 in their study [204]. Accordingly, while ZIF-8 crystals with truncated cubic phase were formed in aqueous solution, ZIF-8 with RD phase was formed in methanolic solution even though metal/linker ratio, temperature, and concentration are the same. Moreover, it was determined that the RD phase occurs again in the aqueous solution when the temperature and metal/linker ratio are changed. This indicates that the synthesis of ZIF-8 carried out in aqueous solution is much more sensitive than that carried out in organic solvent.

Although the synthesis of ZIF-8 in water is sensitive to the kinetics of the reaction, currently the most preferred method of ZIF-8 synthesis is the approaches performed in aqueous solutions. There are two main reasons for this situation. First, organic solvents are generally more expensive and can cause irreversible damage to the environment. Secondly and the most importantly, in organic solvent-based methods, organic molecules can easily interact with ZIF-8, and it is a very difficult process to separate these crystals formed after synthesis from organic molecules [205]. Moreover, in reactions carried out in solvents such as

DMF, the pores of ZIF-8 may become clogged [206]. ZIF-8 preparation techniques carried out until 2011 were synthesis studies generally using organic solvents. However, Pan et al. (2011) had shown that ZIF-8 can be synthesized in aqueous solutions and at room temperature easily and in a very short time, then the synthesis methods of ZIF-8 generally changed to be based on aqueous solutions [207].

Another factor affecting the morphology and crystal structure of ZIF-8 is the mIm/Zn ratio. Generally, this ratio is one of the most important factors responsible for the rate at which the reaction will take place, and the morphology and size of the crystal structure. For instance, Zhang et al. (2018) examined the effect of the mIm/Zn ratio on ZIF-8 crystals in their study [208]. Among the ZIF-8 crystals synthesized in different ratios (1, 2, 4, 8, and 16), low ratios produced ZIF-8s in cubic shapes, while those with high ratios formed TRD or RD crystals. Moreover, a reduction in size and an increase in crystallinity and surface area were observed for ZIF-8s synthesized at high ratios.

Different zinc precursors used during the synthesis of ZIF-8 can affect the emergence of ZIF-8s with different crystal morphologies and sizes. In one of the good and systematic studies on this subject, the effects of both mIm/Zn molar ratio and different zinc sources on ZIF-8 crystal morphology and size were shown (Figure 1.23) [209]. Accordingly, it was reported that among the six different zinc precursors ($Zn(OAc)_2$, $ZNSO_4$, $Zn(NO_3)_2$, $ZnCl_2$, $ZnBr_2$ and ZnI_2), $Zn(OAc)_2$ helped to produce the best quality ZIF-8 crystals with RD morphology. Moreover, different crystal morphologies and sizes were obtained with different adjustments of the mIm/Zn ratio. On the other hand, the synthesis approach of ZIF-8 is also important about which zinc precursor should be selected. For instance, Ramu et al. (2018) used three different zinc precursors ($Zn(NO_3)_2$, $ZnCl_2$ and $Zn(OAc)_2$) and synthesized ZIF-8 membranes by microwave-assisted seeding method [210]. They reported that the most suitable zinc precursor for this method is $Zn(NO_3)_2$. In another study, Wang et al. (2017) showed that ZIF-8s synthesized with $ZnSO_4$ precursor had the best catalytic activity [211]. Undoubtedly, the choice of precursor does not only affect the crystal structure or size. but also, be an answer to hydrolysis and, accordingly, low hydrostability problems that limit the use of ZIF-8 in various applications. In a study conducted in this context, Sheng et al. (2017) investigated the difference in hydrostability of ZIF-8 nanocrystals obtained from different zinc precursors [212]. The results revealed that ZIF-8 NPs synthesized using $Zn(OAc)_2$ were much more resistant to hydrostability than those

using $Zn(NO_3)_2$. The authors reported that ZIF-8s synthesized from the $Zn(OAc)_2$ precursor had a smaller concentration of defects as the reason for this.

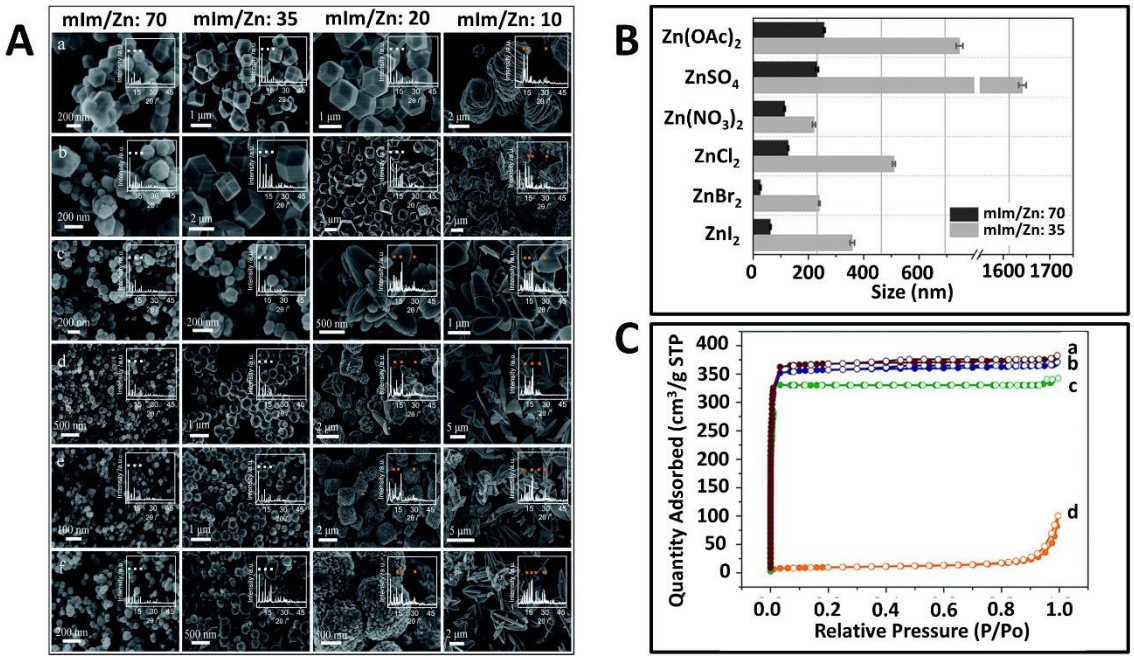

Figure. 1.23. (A) *SEM images and PXRD results of ZIF-8 obtained from different mIm/Zn ratios and Zn precursors (a) $Zn(OAc)_2$, (b) $ZnSO_4$, (c) $Zn(NO_3)_2$, (d) $ZnCl_2$, (e) $ZnBr_2$, (f) ZnI_2.* ***(B)*** *Comparison of the crystal size of ZIF-8 particles obtained from 6 different Zn precursors at the mIm/Zn ratio of 70 and 35.* ***(C)*** *N_2 isotherms of ZIF-8 prepared from $Zn(OAc)_2$ at mIm/Zn molar ratios of (a) 70, (b) 35, (c) 20 and (d) 10. Adapted with permission from ref. [209]. Copyright 2011, Royal Society of Chemistry.*

One of the other important factors to reveal ZIF-8 crystals is the addition of chemical molecules called *capping agents* into the reaction. A capping agent regulates the rate of ZIF-8 crystallization by controlling the nucleation phase. As a result, different agents or the same agent at different concentrations cause the appearance of ZIF-8 crystals with different crystal morphologies or sizes (Figure 1.24A). The most commonly used capping agent in ZIF-8 synthesis is CTAB. Apart from this, molecules such as CTAC, PVP, PEG, SDS, and TEA are often used as capping agents. Pan and his co-worker's work (2011) is valuable as it was the first to show the importance of using modulators or capping agents during synthesis of ZIF-8 [213]. In their work, the effects of molecules such as CTAB, CTAC, STAC and TPABr on ZIF-8 crystallization were investigated (Figure 1.24B). The results showed that with increasing CTAB concentration, both the crystal sizes of ZIF-8s decreased, and their crystal morphologies

changed from RD to cubic morphology. The reason is that the hydrophobic tail of CTAB selectively suppresses the growth of (100) faces of ZIF-8 crystals, resulting in smaller and cubic-shaped ZIF-8 crystals. Similar results were obtained from CTAC and STAC, but TPABr could not show a similar effect as it does not have any hydrophobic tail. Another study carried out by Pan's research group shed light on how to form ZIF-8 crystals of different anisotropic shapes [214]. Accordingly, both the CTAB concentration and the H_2O/mIm molar ratio have an effect on the formation of these morphologies and the authors also presented a morphological map of ZIF-8 (Figure 1.24C).

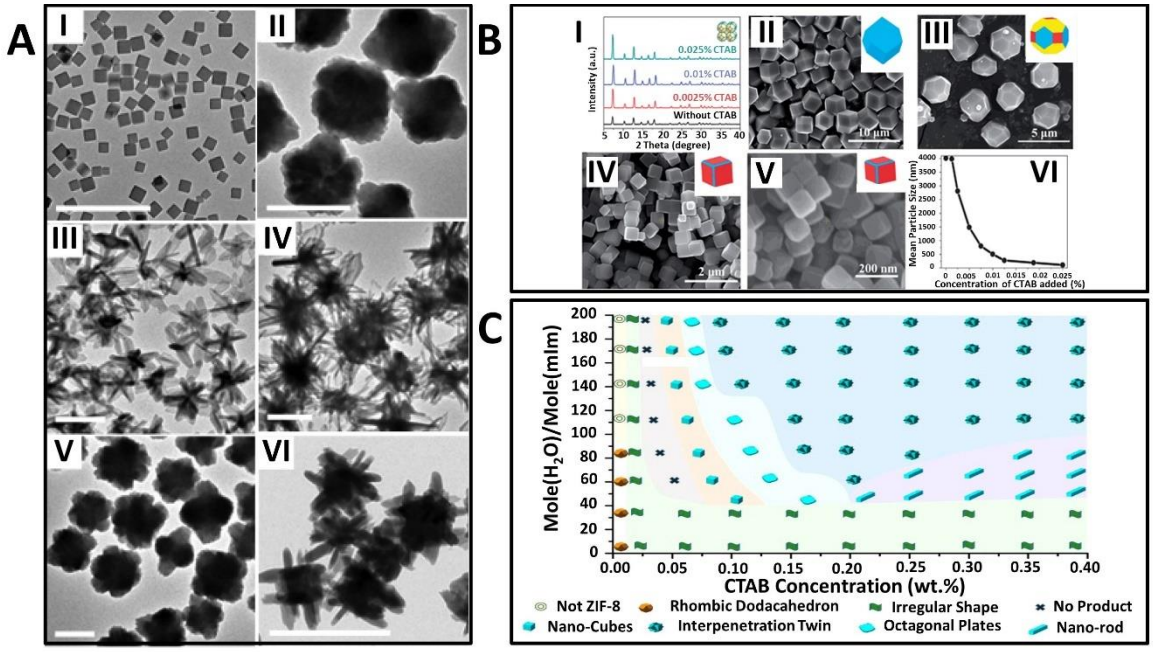

Figure 1.24. (A) *TEM images of ZIF-8 nanocrystals synthesized in the presence of different capping agents: (I) 0.07 mM CTAB, (II) 10 mM TRIS, (III) 50 mM TRIS, (IV) 100 mM TRIS, (V) 0.07 mM CTAB and 10 mM TRIS, and (VI) 0.07 mM CTAB and 50 mM TRIS. Adapted with permission from ref. [215]. Copyright 2009, Royal Society of Chemistry.* ***(B)*** *XRD patterns and SEM images of ZIF-8 crystals prepared with different amounts of CTAB. (I) XRD patterns, (II) no CTAB, (III) 0.0025 wt%, (IV) 0.01 wt%, (V) 0.025 wt%, and (VI) plot of the mean particle size of ZIF-8 crystals versus the concentrations of CTAB added. Adapted with permission from ref. [213]. Copyright 2011, Royal Society of Chemistry.* ***(C)*** *Morphological map of ZIF-8 crystals synthesized with different concentrations of CTAB and the molar ratio of H_2O/mIm. Adapted with permission from ref. [214]. Copyright 2018, American Chemical Society.*

1.7. Plasmonic-ZIF-8 Nanocomposites

It is possible to obtain nanoparticular plasmonic-ZIF-8 composites with different sizes, crystal morphologies and surface areas, thanks to the fact that the factors described above. Generally, there are some advantages to using plasmonic NPs with ZIF-8 compared to other plasmonic nanocomposites. First, there is no need for very high temperatures, pressures, or organic solvents during the synthesis of ZIF-8. In this way, it is ensured that some anisotropic plasmonic NPs, which may lose their morphology due to temperature, are not affected by ZIF-8 crystallization in these kinds of environments. This allows the protection of the shape and properties of plasmonic NPs, and the development of composites containing plasmonic NPs in different morphologies for various SERS applications. Second, ZIF-8 has one of the superior molecular sieving properties, which is very important for SERS applications. Although its pore opening size is 3.4 Å, the methylimidazole linker in the structure can rotate freely and therefore the structure has flexibility, allowing larger molecules to be absorbed into the structure [216]. Third, ZIF-8, as a shell material, keeps plasmonic NPs away from the chaotic external environment and maintains the SERS signal quality due to its tuneable mechanical and chemical stability. Finally, due to the highly hydrophobic nature of ZIF-8, it can be expected that most molecules of interest for which SERS measurement should be made in aqueous media will rush into the pores of ZIF-8. In this way, ZIF-8 acts as enrichment material and it is allowing a large number of molecules of interest to accumulate on the surface of plasmonic NPs, compared to NPs that are not integrated with ZIF-8. This means better quality SERS signal and lower detection limit for many analytes.

Today, we see that ZIF-8 can be integrated with plasmonic NPs via different approaches. The general understanding is based on coating one or more plasmonic or biplasmonic cores of different morphologies with ZIF-8 and obtaining plasmonic@ZIF-8 core-shell structures. This approach, called *bottle-around-ship*, is a classic method that is often encountered in the preparation of core-shell nanocomposites while it is ideal for coating a single plasmonic NP with ZIF-8, it can also be encountered in ways where multiple plasmonic NPs are encapsulated within a single ZIF-8 crystal. The most important points in this method are the good adjustment of concentrations of ZIF-8 precursors and plasmonic NPs, and ZIF-8 crystallization time to obtain the desired shell thickness. On the other hand, in another approach, *the-ship-in-a-bottle* approach, ZIF-8 crystals are first produced in the desired morphology and size, and then these

crystals are immersed in the medium for plasmonic NP precursors (for instance $HAuCl_4$ and $AgNO_3$, for Au NP and Ag NP, respectively). Thus, it is expected that ZIF-8 absorb these precursors and then, ZIF-8 particles carrying precursors are reacted with different reducing agents under appropriate conditions, and plasmonic NPs are formed within ZIF-8 crystals. However, this approach has some risks such as being laborious and occurring problems that may cause differences in the ZIF-8 surface area before and after the reaction, and aggregated plasmonic NPs that will be formed as a result of the reaction.

Recently, Plasmonic-ZIF-8 nanocomposites are frequently used for SERS-based detections of various analytes such as gases, volatile organic compounds (VOCs), polycyclic aromatic hydrocarbons (PAHs), and pesticides. Up to now, with photovoltaic technologies, the detection of environmentally harmful, toxic or flammable gases has been widely recognized [217, 218]. However, one of the major disadvantages of these techniques is that they are inefficient for detecting low-concentration gases [219]. As an alternative to these traditional approaches, ZIF-8-based plasmonic substrates for SERS-based techniques are very attractive. In this way, the gases which are difficult to detect at low levels or are normally difficult to be detected by the plasmonic surface, can be easily detected.

In one of the first example of this kind of detection, benzene, toluene, nitrobenzene, and 2,6-di-tert-butylpyridine vapours, which are normally not interact with the plasmonic surface and therefore do not give SERS signals, were trapped by ZIF-8 and good SERS signal quality could be received [220]. Generally, the substrates based on bottle-around-ship approach with a thin ZIF-8 shell are considered to be powerful SERS substrates when compared them to the materials with thick ZIF-8 shell. For instance, Chen et al. (2021) detected weakly adsorbed molecules such as VOCs with core-shell Au@ZIF-8 materials with shell thicknesses ranging from 3 to 50 nm [221]. The results indicated that Au@ZIF-8 nanocomposites with shell thicknesses of 3 nm show the best SERS performance, and it was suggested that superior SERS performance can be obtained from the substrates, when been kept the distance between the plasmonic surface and the ZIF-8 shell short. On the other hand, keeping the distance between the plasmonic surface and the shell short does not always mean that the best SERS performance can be achieved. The study by Phan-Quang et al. (2019) on this subject gives us a different perspective [222]. In their study, the authors produced a 3D multilayered Ag@ZIF-8 SERS platform to detect of 4-MBT aerosols (Figure 1.26A). Accordingly, the multilayered

platform gave better SERS performance than the other platforms which were only consisted of Ag NC and only the top layer is covered with ZIF-8. As a result, they pointed out that the analyte had the best penetration behaviour for the multilayered SERS substrate. Moreover, they reported that among the substrates tested in five different thicknesses (from 0.2 to 9.2 μm), the platform with a thickness of 1.3 μm had given the best performance, and they assumed that the laser focal volume was one of the critical factors to obtain good SERS signal from the gaseous analytes via these kinds of substrates. In another study, it was also reported that harmful VOCs such as toluene can be detected at ppm levels as a result of fine-tuning both the ZIF-8 thickness and the distance between the plasmonic NPs (Figure 1.26B) [223]. On the other hand, CO_2, another harmful gas, was detected with Au-dotted Ag-NWs which were coated with thin shell of ZIF-8 (Figure 1.26C) [224]. The results showed that CO_2 gas, which normally cannot be adsorbed by the plasmonic surface, can be easily captured by ZIF-8 even if its thickness is ultrathin, and SERS detection of gaseous analytes can be performed.

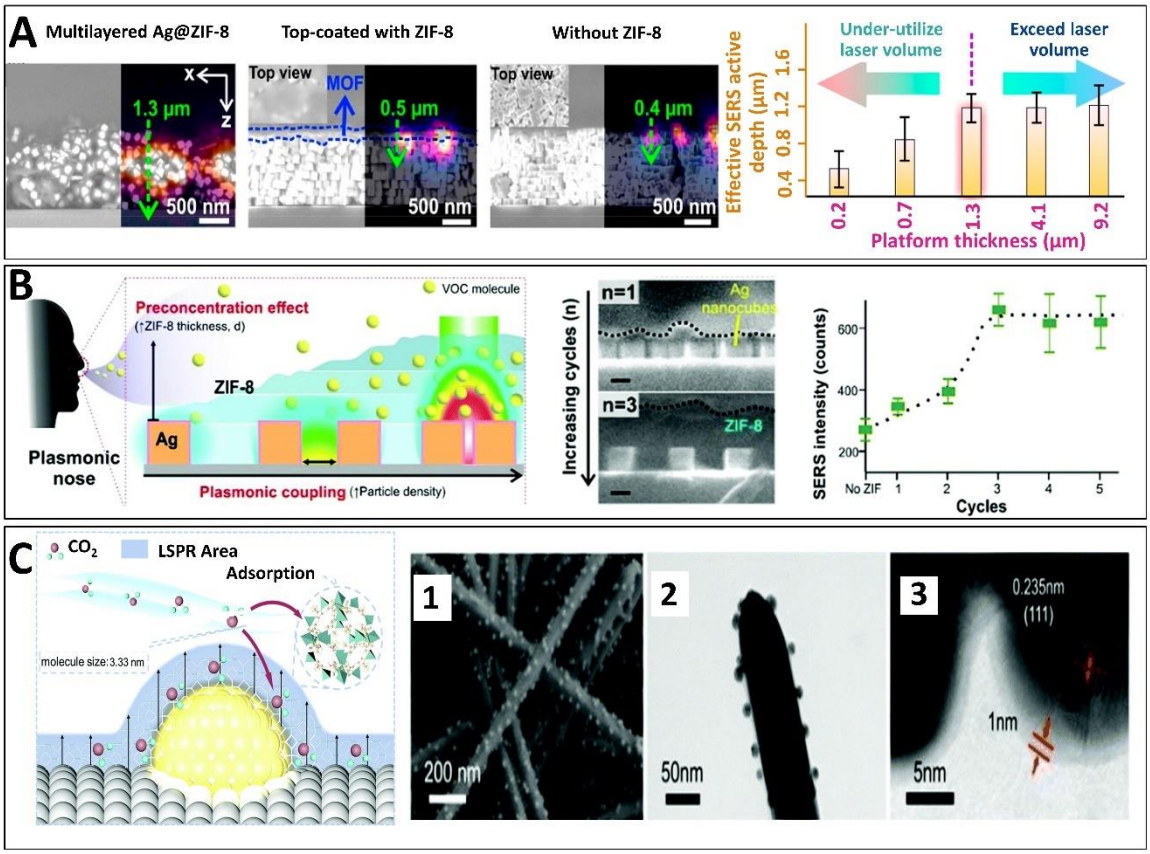

Figure 1.25. *Examples of different plasmonic-ZIF-8 SERS substrates for detection of various volatile analytes.* ***(A)*** *Cross-sectional SEM and SERS hyperspectral images show the different platform configurations and the penetration of gaseous 4-MBT into these platforms, respectively. The Relation between effective SERS active depth and the platform thicknesses is also showing the changing of SERS signal of 4-MBT at 1077 cm^{-1} band. Adapted with permission from ref. [222]. Copyright 2019, American Chemical Society.* ***(B)*** *Schematic illustration of the "plasmonic nose" concept based on tuning plasmonic hotspots and ZIF-8 thickness. Cross-sectional SEM images show to the substrates after one (n=1) and three (n=3) ZIF-8 growth cycles. Scale bars, 100 nm. SERS intensity of 4-MBT vapour is also given as a function of ZIF-8 growth cycles. The SERS intensities are based on the characteristic vibrational mode of 4-MBT at 1079 cm^{-1}. Adapted with permission from ref. [223]. Copyright 2018, Royal Society of Chemistry.* ***(C)*** *Schematic illustration of enrichment of CO_2 gas molecules via plasmonic-ZIF-8 substrate. (1) SEM image of Ag@Au@ZIF-8 NWs. (2) TEM images of a single Ag@Au NW with an ultrathin ZIF-8 shell. (2) HRTEM image of a single Ag@Au NW with an ultrathin ZIF-8 shell. Adapted with permission from ref [224]. Copyright 2021, Royal Society of Chemistry.*

The use of SERS substrates, in which plasmonic NPs are individually coated with ZIF-8, is widely studied (Figure 1.26). In this way, both NPs are prevented from being aggregated and

the quality of the SERS signal level is preserved by ensuring that these NPs are not affected by the chaotic external environment.

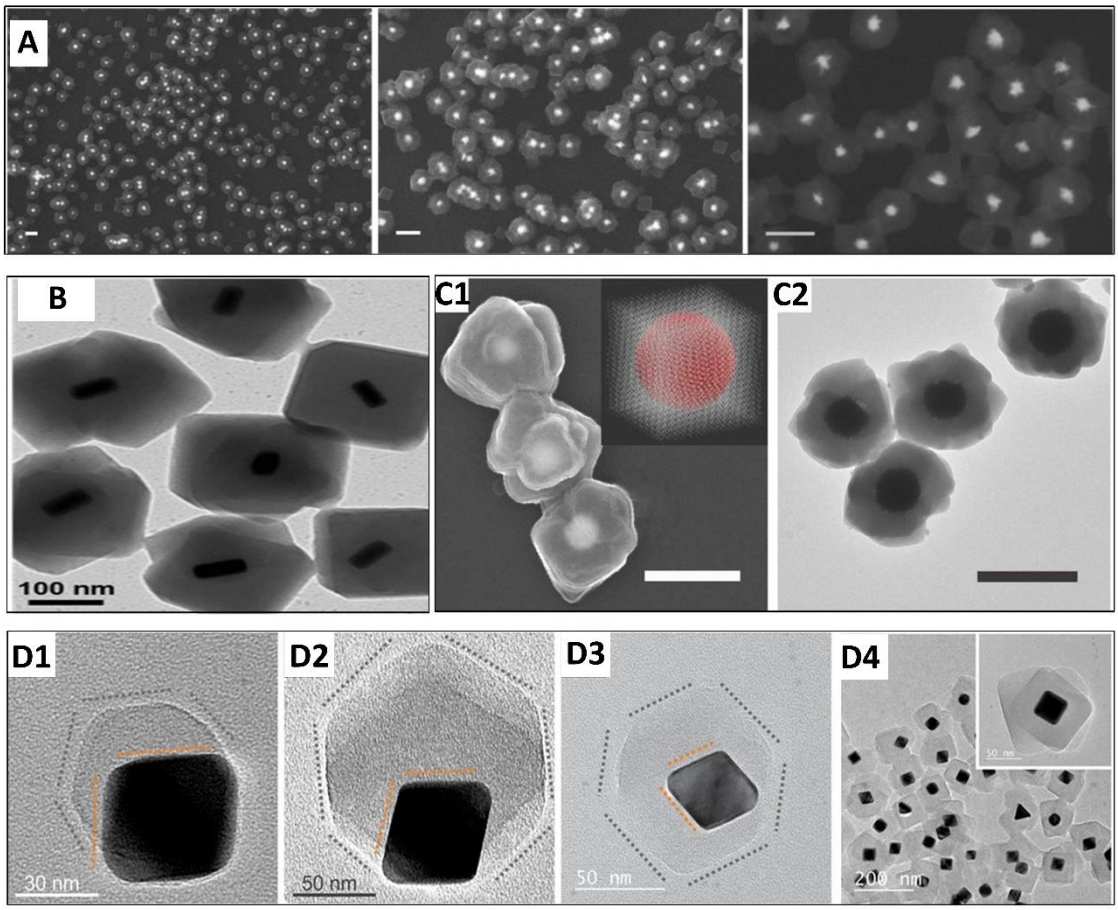

Figure 1.26. *Examples of plasmonic@ZIF-8 nanocomposites that have plasmonic cores with different morphologies.* ***(A)*** *SEM images of NS@ZIF-8 with different magnifications. Scale bars, 200 nm. Adapted with permission from ref. [66]. Copyright 2019, John Wiley and Sons.* ***(B)*** *TEM image of NR@ZIF-8. Adapted with permission from ref. [225]. Copyright 2021, American Chemical Society.* ***(C1)*** *and* ***(C2)*** *SEM and TEM images of spherical@ZIF-8 superparticle, respectively. Scale bars: 500 nm. Adapted with permission from ref. [226]. Copyright 2017, John Wiley and Sons. TEM images of octahedron@ZIF-8 at different reaction stages,* ***(D1):*** *1 min,* ***(D2)*** *and* ***(D3):*** *2 min.* ***(D4)*** *Polycrystalline ZIF-8 shell. Adapted with permission from ref. [227]. Copyright 2014, American Chemical Society.*

There are some studies in which plasmonic NPs with various morphologies are individually coated with ZIF-8 and used them as core-shell SERS substrates for detection of harmful molecules. For instance, the gas form of formaldehyde, which has a carcinogenic effect on humans, was detected at ppb level thanks to the molecular trapping feature of Au NS@ZIF-

8 core-shell nanocomposite. [228]. It is one of the promising developments for the future that chemicals such as chemical warfare agents (CWAs) that can be instantly fatal or cause irreversible damage to humans can be detected with plasmonic-ZIF-8 substrates. In one of the recent studies, Lafuente et al. (2021) detected CWA gases by Au@Ag@ZIF-8 [229]. For this, the authors selected the chemicals such as DMMP and CEES as simulants of hazardous gases such as sarin and mustard gas, respectively. The results showed that portable Raman equipment can detect DMMP up to 2.5 ppm in air and CEES up to 76 ppb in N_2 environment. In addition, the authors reported that DMMP and CEES had detection response times of 21 and 54 seconds, respectively.

Plasmonic-ZIF-8 nanocomposites can be used for not only gaseous molecules, but also SERS-based detections of various herbicides, insecticides and pesticides that have the potential to harm the environment and therefore human health. In one of these studies, Zhou et al. (2019) coated urchin-like Au-Ag alloyed nanocrystals (UAANs) with ZIF-8 and used these nanocomposites for the detection of HCH molecule, an insecticide [230]. The authors reported that among the ZIF-8 shell thicknesses ranging from 0 to 40 nm, the best SERS performance was achieved with a substrate with a thickness of 20 nm, and HCH could be detected up to 1.5 ppb. In another study, bead-string like Ag NW@ZIF-8 core-shell nanochains were prepared and the SERS performance of the substrate was tested [231]. The results showed that the substrate could detect two different pesticides such as methylparathion and carbaryl up to 7.6×10^{-9} M and 5.7×10^{-9} M, respectively. The new structures obtained as a result of various post-modification methods of ZIF-8 offer us different perspectives for SERS-based analytical methods. The most well-known of these post-modifications is calcination of ZIF-8 under high temperature, thereby converting it to ZnO, a widely used photocatalyst. The use of such materials with plasmonic NPs and their synergistic effects are very advantageous in terms of SERS performance. In this context, Ye et al. (2022) coated TiO_2 NRs prepared on FTO glass surface with ZIF-8 and these nanomaterials calcined under high temperature to evolved them to TiO_2/ZnO heterostructures [232]. Then, the surface of these structures was decorated with Ag NPs and the obtained SERS substrate was used for the detection of pesticides such as thiram, acephate and phoxim. In this way, the authors were able to detect pesticides by 10^{-7} M and reported that TiO_2/ZnO/Ag substrate had a 39-fold higher signal amplification ability than TiO_2/Ag substrate.

Plasmonic-ZIF-8 core-shell nanocomposites are also well suited for various medical-purpose SERS applications. This allows SERS-based analyses of changes in the levels of various molecules involved in intracellular or intercellular signal pathways with plasmonic-ZIF-8 substrates. A study showed that the substrates obtained by coating of 2-MHQ grafted-Au NPs with ZIF-8 can be effective for *in situ* monitoring of H_2O_2 released from living cells ([233]. On the other hand, thanks to the Zn^{2+} metal ion in SBUs, the affinity of biological molecules toward ZIF-8 structure can be ensured [103]. In a study on this topic, individual Au@Ag NRs were coated with ZIF-8 and encoded with Raman reporters such as astra blue (AB), methylene blue (MB), malachite green isothiocyanate (MGI), and nile blue (NB) [234]. SERS nanotags were formed by the interaction of polyhistidine with Zn^{2+}. (Figure 1.27A). Then, *Streptococcus* protein G (pG) and SpyCatcher (SC) domains interacted with polyhistidine, and these domains were bound with immunoglobulin and SpyTag peptide, respectively. Thus, *in vitro* SERS-based detection of EGFR and CD44 biomarkers on the cell surface was carried out. The use of plasmonic-ZIF-8 nanocomposites in medical applications should not be considered only as SERS-based detection. In recent years, these structures have been accepted as medically versatile materials and have thus become theragnostic substrates that promise diagnosis and treatment at the same time. In this context, Sun et al. (2020)'s study is quite interesting [235]. In the study, mercaptobenzonitrile-decorated Ag NPs (Ag@MBN) and glucose oxidase (GOx) were coated with ZIF-8, and thus theragnostic plasmonic substrates that could work as a "*nanoreactor*" in the tumor cell were revealed. The aim here is that ZIF-8 degrades to release GOx and Ag@MBN within the tumor microenvironment, and GOXs initiate the catalytic cascade of β-α-glucose (Figure 1.27B). The results show that the free Zn^{2+} ions formed by the degradation of ZIF-8, and H_2O_2 molecules which are formed as a result of the catalytic reaction of glucose, can trigger apoptosis, and that the intracellular glucose level can be measured with a SERS-based technique thanks to Ag@MBN NPs.

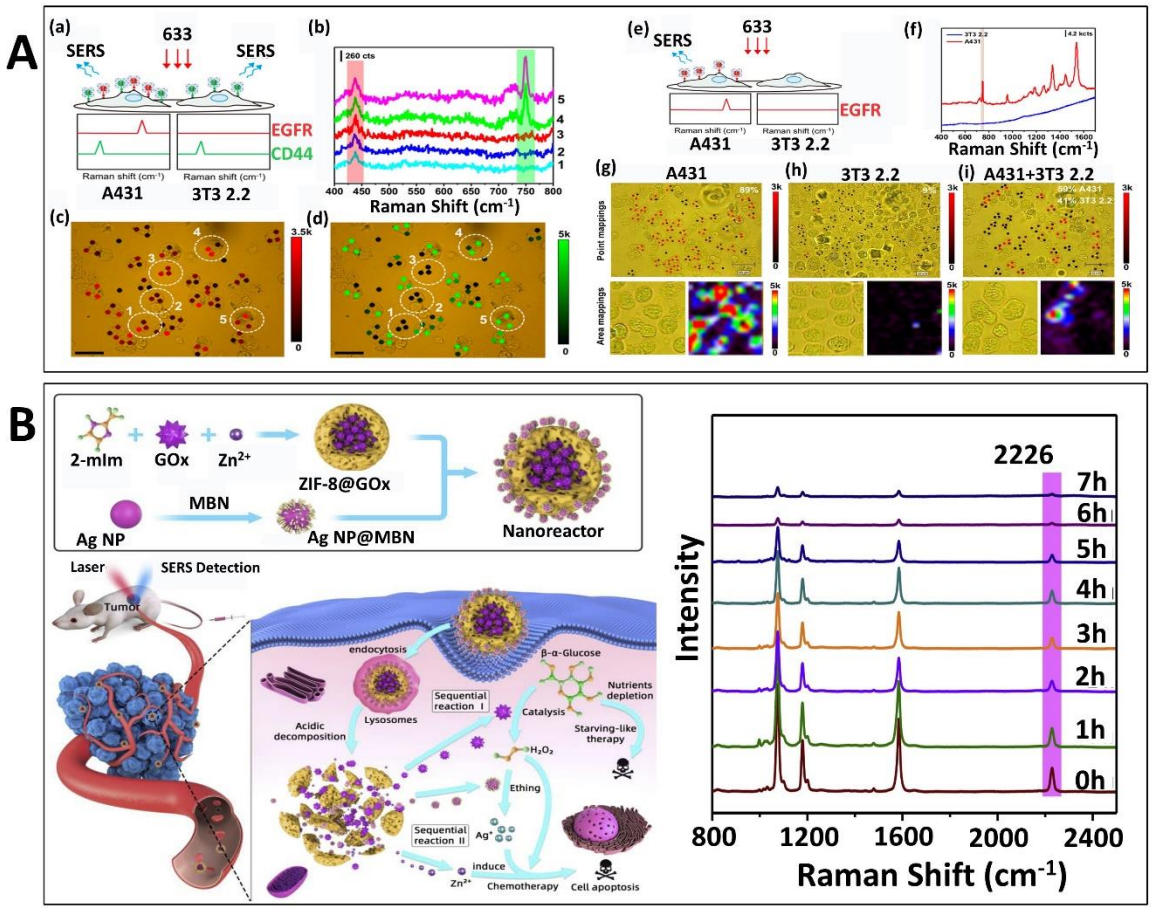

Figure 1.27. Usage of plasmonic-ZIF-8 SERS substrates in medical application. ***(A)*** *Schematic representation for the identification of EGFR and CD44 in mixtures of A431 and 3T3 2.2 cells using plasmonic@ZIF-8 NPs encoded with AB or MGI and functionalized with anti-EGFR or anti-CD44 antibodies, respectively (a). Representative SERS spectra obtained from the cells indicated with a white dashed circle and numbered in the bright-field images (b). Bright-field images of mixed A431 and 3T3 2.2 cells and single-point SERS mappings recorded at 440 (MGI, panel c) and 748 cm–1 (AB, panel d) for the detection of CD44 and EGFR, respectively (c-d). Schematic representation for the identification of EGFR in mixtures of A431 and 3T3 2.2 cells using plasmonic-ZIF-8 NPs functionalized with nanobodies via polyhistidine-tagged SpyCatcher (e). Representative SERS spectra obtained from A431 (red) and 3T3 2.2 (blue) cells (f). Bright-field images and SERS mappings of (g) A431, (h) 3T3 2.2, and (i) mixed A431 + 3T3 2.2 cells. Adapted with permission from ref. [234]. Copyright 2020, American Chemical Society.* ***(B)*** *Schematic illustration of the preparation of ZIF-8-based nanoreactors, and their catalytic cascade-enhanced synergistic chemo-starvation therapy for cancer cells. The spectra shows that changing of glucose in HeLa cells incubated with ZIF-8@GOx-AgNPs@MBN for different times. Adapted with permission from ref. [235]. Copyright 2020, Elsevier.*

Plasmonic-ZIF-8 nanocomposites are likely to evolve into more useful SERS-based sensors by various post-modification methods. Generally, calcination at very high temperatures or coating of ZIF-8 with various polymers are the most well-known of these modifications [66, 236-238]. However, these approaches have some risks such as affecting the surface area, crystal structure and pores of ZIF-8. Therefore, these approaches can be disadvantageous in terms of SERS applications. Post-modification techniques without affecting the physical and chemical integrity of ZIF-8 are of great importance in this context. One of the most well-known examples of modification is to introduce plasmonic-ZIF-8 SERS substrates in a yolk-shell structure. Yolk-shell nanocomposites, like core-shells, are promising materials for a variety of applications. The common point in both materials is to protect the core from external effects. As mentioned earlier, such a material for an innovative SERS application is very popular due to its ability to prevent plasmonic NPs from aggregating in various mediums, thereby achieving high SERS signal amounts from analyte of interest. The point where yolk-shell nanocomposites differ is the high-volume voids they have. Thanks to these voids, larger amounts of analyte are expected to accumulate inside the pores of ZIF-8 and interact with the plasmonic surface. Thus, more powerful SERS-substrates can be obtained when compared with bare NPs and core-shell plasmonic-ZIF-8 composites.

There are two simple basic approaches to fabricate Yolk-shell plasmonic-ZIF-8 nanocomposites: **(1)** template-free, and **(2)** template-assisted methods. In template free methods, it is aimed to etching ZIF-8 chemically. The most common chemical etching agents are molecules such as tannic acid, gallic acid or phytic acid [239-241]. In this way, the H^+ ions released from these types of phenolic acids interact with the Zn^{2+} metal ions in ZIF-8 and, starting from the outer layer of ZIF-8, provide the transformation of the MOF to the yolk-shell structure towards the inner parts. There are two important points at this stage. The first is the concentration of the organic acid, and the second is the interaction time between acid and ZIF-8. Morphological deformation of ZIF-8 may be seen if the interaction is prolonged, or the concentration is too high. In such a scenario, as a result, it is meaningless to talk about a yolk-shell structure. On the other hand, ZIF-8 may occur in the short-term or low-concentration acid application, which degrades the outer layer but can survive in the inner part (Figure 1.28A).

Template-free approaches have the potential to affect the LSPR changes in plasmonic NPs which are encapsulated in ZIF-8. Morphological changes or surface oxidations can be

observed in plasmonic NPs, especially due to the use of different organic acids. Moreover, because the acids used for etching are relatively large molecules, the pores of ZIF-8 might be also blocked. This is one of the biggest problems for SERS-based sensing studies via yolk-shell substrates. Therefore, such an approach is more suitable for NPs that will not be affected much by these processes, and accordingly, we do not see many yolk-shell plasmonic-ZIF-8 structures prepared with the template-free method in the field of plasmonics.

As an alternative way, yolk-shell plasmonic-ZIF-8 nanocomposites produced by template-assisted methods may be more efficient in terms of conservation of plasmonic nature. The main logic in this approach is to coat the plasmonic NPs with a *sacrificial template* and then grow ZIF-8 on this template. The important point is to ensure that the chemical composition of both the plasmonic NPs and ZIF-8 crystals is minimally affected during the degradation of the sacrificial template. There are some studies in which PS beads, Cu_2O or different MOF types are used as sacrificial templates for this purpose (Figure 1.28B-D). However, because the method is time consuming and, in some cases, requires high temperatures or different types of solvents to remove the sacrificial template, anisotropic plasmonic NPs, which can lose their morphology under such stimuli, are generally not preferred in the produced yolk-shell nanocomposites.

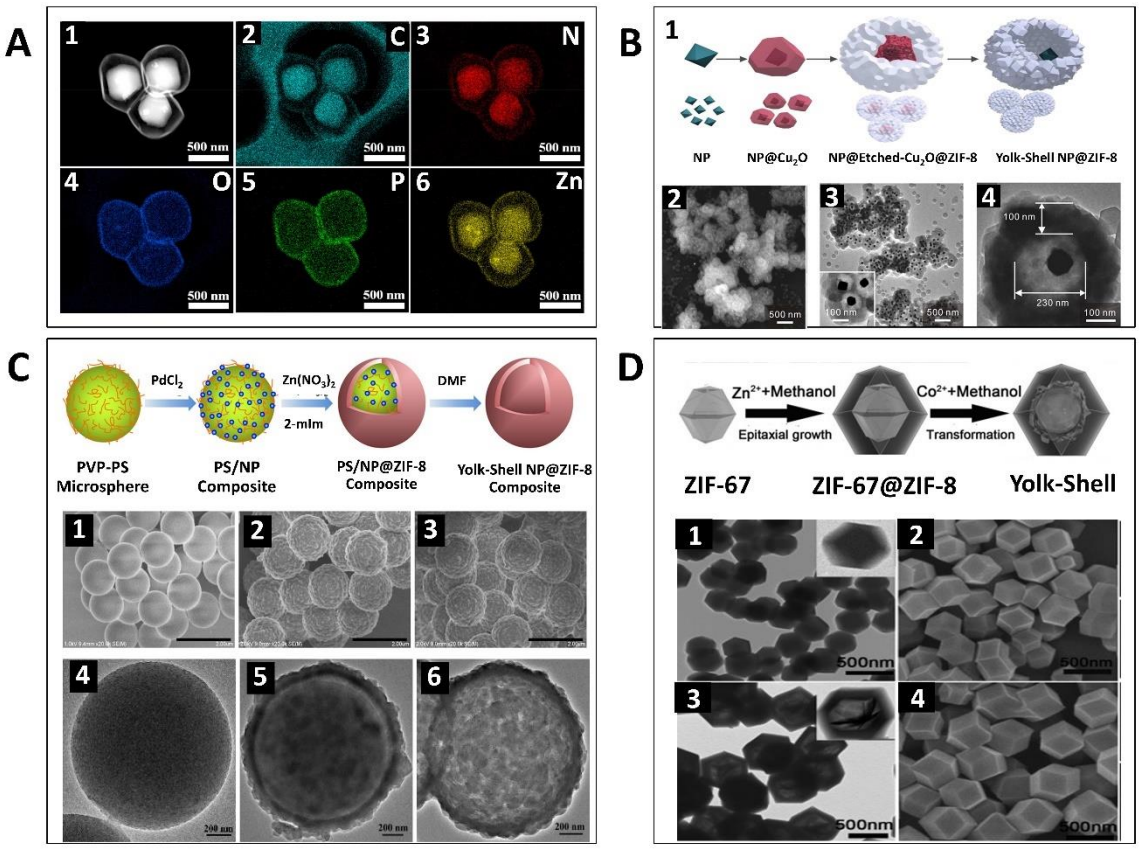

Figure 1.28. (A) EDX element mapping images of yolk-shell ZIF-8 particles produced via template-free approach (1-6). Degradation of the outer layer is clearly seen from the images. Adapted with permission from ref. [241]. Copyright 2021, Elsevier. (B) Schematic illustration of preparing yolk-shell NP@ZIF-8 nanocomposites via template-assisted strategy (1). In here, Cu2O was used as a sacrificial template to obtain the final structure, and it can be etched via adjustment of pH of the reaction. (2-4) show SEM and TEM images of the final product. Adapted with permission from ref. [242]. Copyright 2012, American Chemical Society. (C) Schematic representation of synthesis procedure yolk-shell NP@ZIF-8. SEM and TEM images for PVP-PS (1,4), PS/NP@ZIF-8 (2,5), and yolk-shell NP@ZIF-8 composites (3,6). Adapted with permission from ref. [243]. Copyright 2020, American Chemical Society. (D) Schematic representation of the structural evolution. TEM and SEM images for ZIF-67@ZIF-8 (1,2), and yolk-shell material (3,4). Adapted with permission from ref. [244]. Copyright 2015, John Wiley and Sons.

All the properties described so far regarding plasmonic-ZIF-8 nanocomposites prove that these materials can be good substrates for SERS-based sensing strategies. Moreover, with various modifications, these materials have the potential to improve their SERS performance to one step further.

1.8. References

1. Puolamaa, M., *The appropriateness of existing methodologies to assess the potential risks associated with engineered and adventitious produc.* 2006.
2. Feynman, R.P. *Plenty of Room at the Bottom*. in *APS annual meeting*. 1959.
3. Yang, T., et al., *Food and beverage ingredients induce the formation of silver nanoparticles in products stored within nanotechnology-enabled packaging.* ACS Applied Materials & Interfaces, 2021. **13**(1): p. 1398-1412.
4. Salvioni, L., et al., *The emerging role of nanotechnology in skincare.* Advances in Colloid and Interface Science, 2021. **293**: p. 102437.
5. Kumar, A., et al., *Nanotechnology in paper and wood engineering: an introduction*, in *Nanotechnology in Paper and Wood Engineering*. 2022, Elsevier. p. 3-13.
6. Singh, P., et al., *Insights from nanotechnology in COVID-19: prevention, detection, therapy and immunomodulation.* Nanomedicine, 2021. **16**(14): p. 1219-1235.
7. Chintagunta, A.D., S. Nalluru, and S.K. NS, *Nanotechnology: An emerging approach to combat COVID-19.* Emergent materials, 2021. **4**(1): p. 119-130.
8. Ikumapayi, O., et al., *Microfabrication and nanotechnology in manufacturing system–An overview.* Materials Today: Proceedings, 2021. **44**: p. 1154-1162.
9. Yadav, N., et al., *Detection and remediation of pollutants to maintain ecosustainability employing nanotechnology: A review.* Chemosphere, 2021. **280**: p. 130792.
10. Sharma, R., *Nanotechnology in space exploration: needs and applications.* Journal of Pure Applied and Industrial Physics, 2012. **2**(3A): p. 286-335.
11. Wang, J., J. Gong, and Z. Wei, *Strategies for liposome drug delivery systems to improve tumor treatment efficacy.* AAPS PharmSciTech, 2022. **23**(1): p. 1-14.
12. Large, D.E., et al., *Liposome composition in drug delivery design, synthesis, characterization, and clinical application.* Advanced Drug Delivery Reviews, 2021. **176**: p. 113851.
13. Nikzamir, M., et al., *Applications of dendrimers in nanomedicine and drug delivery: A review.* Journal of Inorganic and Organometallic Polymers and Materials, 2021. **31**(6): p. 2246-2261.
14. Dulińska-Litewka, J., et al., *Superparamagnetic iron oxide nanoparticles—Current and prospective medical applications.* Materials, 2019. **12**(4): p. 617.
15. Magro, M. and F. Vianello, *Bare iron oxide nanoparticles: Surface tunability for biomedical, sensing and environmental applications.* Nanomaterials, 2019. **9**(11): p. 1608.
16. Hui, K.C., et al., *Effects of nitrogen/bismuth-doping on the photocatalyst composite of carbon dots/titanium dioxide nanoparticles (CDs/TNP) for enhanced visible light-driven removal of diclofenac.* Chemosphere, 2022. **290**: p. 133377.
17. Sagadevan, S., et al., *Photocatalytic Efficiency of Titanium Dioxide for Dyes and Heavy Metals Removal from Wastewater.* Bulletin of Chemical Reaction Engineering & Catalysis, 2022: p. 17.
18. Jones, R.S., *Gold in Meteorites and in the Earth's Crust*. Vol. 603. 1968: US Government Printing Office.
19. Goodman, P., *Current and future uses of gold in electronics.* Gold bulletin, 2002. **35**(1): p. 21-26.
20. Pricker, S.P., *Medical uses of gold compounds: past, present and future.* Gold bulletin, 1996. **29**(2): p. 53-60.
21. Balfourier, A., et al., *Gold-based therapy: From past to present.* Proceedings of the National Academy of Sciences, 2020. **117**(37): p. 22639-22648.
22. Phillips, A.C., et al. *Progress and new techniques for protected-silver coatings*. in *Advances in Optical and Mechanical Technologies for Telescopes and Instrumentation*. 2014. SPIE.
23. Paladini, F. and M. Pollini, *Antimicrobial silver nanoparticles for wound healing application: progress and future trends.* Materials, 2019. **12**(16): p. 2540.
24. Zamarayeva, A.M., et al., *Fabrication of a High-Performance Flexible Silver–Zinc Wire Battery.* Advanced Electronic Materials, 2016. **2**(5): p. 1500296.
25. Alvarez-Puebla, R.A., J.-F. Li, and X.Y. Ling, *Introduction to advances in plasmonics and its applications.* Nanoscale, 2021. **13**(12): p. 5935-5936.
26. Zhang, Z., et al., *Propagating surface plasmon polaritons: towards applications for remote-excitation surface catalytic reactions.* Advanced Science, 2016. **3**(1): p. 1500215.
27. Liu, J., et al., *Recent advances of plasmonic nanoparticles and their applications.* Materials, 2018. **11**(10): p. 1833.
28. Johnson, P.B. and R.-W. Christy, *Optical constants of the noble metals.* Physical review B, 1972. **6**(12): p. 4370.
29. Homola, J., S.S. Yee, and G. Gauglitz, *Surface plasmon resonance sensors.* Sensors and actuators B: Chemical, 1999. **54**(1-2): p. 3-15.
30. Jain, P.K., et al., *Calculated absorption and scattering properties of gold nanoparticles of different size, shape, and composition: applications in biological imaging and biomedicine.* The journal of physical chemistry B, 2006. **110**(14): p. 7238-7248.
31. Gonzalez, A. and C. Noguez, *Optical properties of silver nanoparticles.* physica status solidi c, 2007. **4**(11): p. 4118-4126.
32. de Aberasturi, D.J., A.B. Serrano-Montes, and L.M. Liz-Marzán, *Modern applications of plasmonic nanoparticles: from energy to health.* Advanced Optical Materials, 2015. **3**(5): p. 602-617.

33. Faraday, M., *X. The Bakerian Lecture.—Experimental relations of gold (and other metals) to light.* Philosophical transactions of the Royal Society of London, 1857(147): p. 145-181.
34. Amendola, V., et al., *Surface plasmon resonance in gold nanoparticles: a review.* Journal of Physics: Condensed Matter, 2017. **29**(20): p. 203002.
35. Nolan, J.P. and D.S. Sebba, *Surface-enhanced Raman scattering (SERS) cytometry*, in *Methods in cell biology*. 2011, Elsevier. p. 515-532.
36. Stockman, M.I., *Nanoplasmonics: The physics behind the applications.* Phys. Today, 2011. **64**(2): p. 39-44.
37. Masson, J.-F., *Portable and field-deployed surface plasmon resonance and plasmonic sensors.* Analyst, 2020. **145**(11): p. 3776-3800.
38. Olson, J., et al., *Optical characterization of single plasmonic nanoparticles.* Chemical Society Reviews, 2015. **44**(1): p. 40-57.
39. Wang, L., M. Hasanzadeh Kafshgari, and M. Meunier, *Optical properties and applications of plasmonic-metal nanoparticles.* Advanced Functional Materials, 2020. **30**(51): p. 2005400.
40. Derkachova, A., K. Kolwas, and I. Demchenko, *Dielectric function for gold in plasmonics applications: size dependence of plasmon resonance frequencies and damping rates for nanospheres.* Plasmonics, 2016. **11**(3): p. 941-951.
41. Maier, S.A., *Plasmonics: fundamentals and applications*. Vol. 1. 2007: Springer.
42. Yeshchenko, O.A., et al., *Size and temperature effects on the surface plasmon resonance in silver nanoparticles.* Plasmonics, 2012. **7**(4): p. 685-694.
43. LaMer, V.K. and R.H. Dinegar, *Theory, production and mechanism of formation of monodispersed hydrosols.* Journal of the american chemical society, 1950. **72**(11): p. 4847-4854.
44. Shields, S.P., V.N. Richards, and W.E. Buhro, *Nucleation control of size and dispersity in aggregative nanoparticle growth. A study of the coarsening kinetics of thiolate-capped gold nanocrystals.* Chemistry of materials, 2010. **22**(10): p. 3212-3225.
45. Lea, M.C., *ART. L.--On Allotropic Forms of Silver.* American Journal of Science (1880-1910), 1889. **37**(222): p. 476.
46. Turkevich, J., P.C. Stevenson, and J. Hillier, *A study of the nucleation and growth processes in the synthesis of colloidal gold.* Discussions of the Faraday Society, 1951. **11**: p. 55-75.
47. Brust, M., et al., *Synthesis of thiol-derivatised gold nanoparticles in a two-phase liquid–liquid system.* Journal of the Chemical Society, Chemical Communications, 1994(7): p. 801-802.
48. Schmid, G., *Large clusters and colloids. Metals in the embryonic state.* Chemical reviews, 1992. **92**(8): p. 1709-1727.
49. Haruta, M., *Gold rush.* Nature, 2005. **437**(7062): p. 1098-1099.
50. Song, K.C., et al., *Preparation of colloidal silver nanoparticles by chemical reduction method.* Korean Journal of Chemical Engineering, 2009. **26**(1): p. 153-155.
51. Tanimoto, H., S. Ohmura, and Y. Maeda, *Size-selective formation of hexagonal silver nanoprisms in silver citrate solution by monochromatic-visible-light irradiation.* The Journal of Physical Chemistry C, 2012. **116**(29): p. 15819-15825.
52. Jana, N.R., L. Gearheart, and C.J. Murphy, *Seeding growth for size control of 5− 40 nm diameter gold nanoparticles.* Langmuir, 2001. **17**(22): p. 6782-6786.
53. Murphy, C.J., et al., *Anisotropic metal nanoparticles: synthesis, assembly, and optical applications.* The Journal of Physical Chemistry B, 2005. **109**(29): p. 13857-13870.
54. Niu, W., L. Zhang, and G. Xu, *Seed-mediated growth of noble metal nanocrystals: crystal growth and shape control.* Nanoscale, 2013. **5**(8): p. 3172-3181.
55. Zheng, Y., et al., *Successive, Seed-Mediated Growth for the Synthesis of Single-Crystal Gold Nanospheres with Uniform Diameters Controlled in the Range of 5–150 nm.* Particle & Particle Systems Characterization, 2014. **31**(2): p. 266-273.
56. Barbosa, S., et al., *Tuning size and sensing properties in colloidal gold nanostars.* Langmuir, 2010. **26**(18): p. 14943-14950.
57. Vigderman, L. and E.R. Zubarev, *High-yield synthesis of gold nanorods with longitudinal SPR peak greater than 1200 nm using hydroquinone as a reducing agent.* Chemistry of Materials, 2013. **25**(8): p. 1450-1457.
58. Lin, X., et al., *Facile synthesis of monodisperse silver nanospheres in aqueous solution via seed-mediated growth coupled with oxidative etching.* Langmuir, 2018. **34**(21): p. 6077-6084.
59. Goldmann, C., et al., *Symmetry Breaking in Seed-Mediated Silver Nanorod Growth Induced by Dimethyl Sulfoxide.* Chemistry of Materials, 2021. **33**(8): p. 2948-2956.
60. Sánchez-Iglesias, A., et al., *High-yield seeded growth of monodisperse pentatwinned gold nanoparticles through thermally induced seed twinning.* Journal of the American Chemical Society, 2017. **139**(1): p. 107-110.
61. Dovgolevsky, E. and H. Haick, *Direct Observation of the Transition Point Between Quasi-Spherical and Cubic Nanoparticles in a Two-Step Seed-Mediated Growth Method.* Small, 2008. **4**(11): p. 2059-2066.
62. Millstone, J.E., G.S. Métraux, and C.A. Mirkin, *Controlling the edge length of gold nanoprisms via a seed-mediated approach.* Advanced Functional Materials, 2006. **16**(9): p. 1209-1214.
63. Nikoobakht, B. and M.A. El-Sayed, *Preparation and growth mechanism of gold nanorods (NRs) using seed-mediated growth method.* Chemistry of Materials, 2003. **15**(10): p. 1957-1962.
64. Khoury, R.A., et al., *Monitoring the seed-mediated growth of gold nanoparticles using in situ second harmonic generation and extinction spectroscopy.* The Journal of Physical Chemistry C, 2018. **122**(42): p. 24400-24406.

65. Philip, A., B. Ankudze, and T.T. Pakkanen, *Polyethylenimine-assisted seed-mediated synthesis of gold nanoparticles for surface-enhanced Raman scattering studies.* Applied Surface Science, 2018. **444**: p. 243-252.
66. Carrillo-Carrión, C., et al., *Aqueous stable gold nanostar/ZIF-8 nanocomposites for light-triggered release of active cargo inside living cells.* Angewandte Chemie, 2019. **131**(21): p. 7152-7156.
67. Kuttner, C., et al., *Seeded growth synthesis of gold nanotriangles: size control, SAXS analysis, and SERS performance.* ACS applied materials & interfaces, 2018. **10**(13): p. 11152-11163.
68. Podlesnaia, E., A. Csáki, and W. Fritzsche, *Time Optimization of Seed-Mediated Gold Nanotriangle Synthesis Based on Kinetic Studies.* Nanomaterials, 2021. **11**(4): p. 1049.
69. Qiu, P. and C. Mao, *Seed-mediated shape evolution of gold nanomaterials: from spherical nanoparticles to polycrystalline nanochains and single-crystalline nanowires.* Journal of Nanoparticle Research, 2009. **11**(4): p. 885-894.
70. Wang, Y.-N., et al., *Seed-mediated growth of ultralong gold nanorods and nanowires with a wide range of length tunability.* Langmuir, 2013. **29**(33): p. 10491-10497.
71. Tavakkoli Yaraki, M., et al., *Synthesis and simulation study of right silver bipyramids via seed-mediated growth cum selective oxidative etching approach.* Particle & Particle Systems Characterization, 2020. **37**(5): p. 2000027.
72. Wiley, B.J., et al., *Right bipyramids of silver: a new shape derived from single twinned seeds.* Nano letters, 2006. **6**(4): p. 765-768.
73. Lin, Z.W., et al., *Seed-Mediated Growth of Silver Nanocubes in Aqueous Solution with Tunable Size and Their Conversion to Au Nanocages with Efficient Photothermal Property.* Chemistry–A European Journal, 2016. **22**(7): p. 2326-2332.
74. Zhong, Y., et al., *Preparation of triangular silver nanoplates by silver seeds capped with citrate-CTA+.* RSC advances, 2018. **8**(51): p. 28934-28943.
75. Qi, K., et al., *Enhancing the CO2-to-CO conversion from 2D silver nanoprisms via superstructure assembly.* ACS nano, 2021. **15**(4): p. 7682-7693.
76. Wan, Y., et al., *Quasi-spherical silver nanoparticles: Aqueous synthesis and size control by the seed-mediated Lee–Meisel method.* Journal of colloid and interface science, 2013. **394**: p. 263-268.
77. Bastús, N.G., et al., *Synthesis of highly monodisperse citrate-stabilized silver nanoparticles of up to 200 nm: kinetic control and catalytic properties.* Chemistry of Materials, 2014. **26**(9): p. 2836-2846.
78. Xing, L., et al., *Size control synthesis of monodisperse, quasi-spherical silver nanoparticles to realize surface-enhanced Raman scattering uniformity and reproducibility.* ACS applied materials & interfaces, 2019. **11**(19): p. 17637-17646.
79. Hegde, H., C. Santhosh, and R.K. Sinha, *Seed mediated synthesis of highly stable CTAB capped triangular silver nanoplates for LSPR sensing.* Materials Research Express, 2019. **6**(10): p. 105075.
80. Anh, M.N.T., et al., *Unveiling the SERS activity of silver triangular nanoplates in the enhanced detection of 4-mercaptobenzoic acid.* Optik, 2021. **248**: p. 168155.
81. Nie, S. and S.R. Emory, *Probing single molecules and single nanoparticles by surface-enhanced Raman scattering.* science, 1997. **275**(5303): p. 1102-1106.
82. Fleischmann, M., P.J. Hendra, and A.J. McQuillan, *Raman spectra of pyridine adsorbed at a silver electrode.* Chemical physics letters, 1974. **26**(2): p. 163-166.
83. Albrecht, M.G. and J.A. Creighton, *Anomalously intense Raman spectra of pyridine at a silver electrode.* Journal of the american chemical society, 1977. **99**(15): p. 5215-5217.
84. Moskovits, M., *Surface roughness and the enhanced intensity of Raman scattering by molecules adsorbed on metals.* The Journal of Chemical Physics, 1978. **69**(9): p. 4159-4161.
85. Creighton, J.A., C.G. Blatchford, and M.G. Albrecht, *Plasma resonance enhancement of Raman scattering by pyridine adsorbed on silver or gold sol particles of size comparable to the excitation wavelength.* Journal of the Chemical Society, Faraday Transactions 2: Molecular and Chemical Physics, 1979. **75**: p. 790-798.
86. Raman, C.V. and K.S. Krishnan, *A new type of secondary radiation.* Nature, 1928. **121**(3048): p. 501-502.
87. Kiselev, R., *Towards clinical translation of raman spectroscopy for tumor cell identification*. 2019.
88. Le Ru, E.C., et al., *Surface enhanced Raman scattering enhancement factors: a comprehensive study.* The Journal of Physical Chemistry C, 2007. **111**(37): p. 13794-13803.
89. Guerrini, L. and D. Graham, *Molecularly-mediated assemblies of plasmonic nanoparticles for Surface-Enhanced Raman Spectroscopy applications.* Chemical Society Reviews, 2012. **41**(21): p. 7085-7107.
90. Aroca, R., *Surface-enhanced vibrational spectroscopy*. 2006: John Wiley & Sons.
91. Cong, S., et al., *Surface enhanced Raman scattering revealed by interfacial charge-transfer transitions.* The Innovation, 2020. **1**(3): p. 100051.
92. Le Ru, E. and P. Etchegoin, *Rigorous justification of the| E| 4 enhancement factor in surface enhanced Raman spectroscopy.* Chemical Physics Letters, 2006. **423**(1-3): p. 63-66.
93. Bohren, C.F. and D.R. Huffman, *Absorption and scattering of light by small particles*. 2008: John Wiley & Sons.
94. Lin, X.-M., et al., *Surface-enhanced Raman spectroscopy: substrate-related issues.* Analytical and bioanalytical chemistry, 2009. **394**(7): p. 1729-1745.
95. Pérez-Jiménez, A.I., et al., *Surface-enhanced Raman spectroscopy: benefits, trade-offs and future developments.* Chemical science, 2020. **11**(18): p. 4563-4577.

96. Zong, C., et al., *Surface-enhanced Raman spectroscopy for bioanalysis: reliability and challenges.* Chemical reviews, 2018. **118**(10): p. 4946-4980.
97. Bell, S.E., et al., *Towards reliable and quantitative surface-enhanced Raman scattering (SERS): From key parameters to good analytical practice.* Angewandte Chemie International Edition, 2020. **59**(14): p. 5454-5462.
98. Álvarez-Puebla, R.n.A., *Effects of the Excitation Wavelength on the SERS Spectrum.* The journal of physical chemistry letters, 2012. **3**(7): p. 857-866.
99. Alvarez-Puebla, R.A., et al., *Surface-enhanced Raman scattering on nanoshells with tunable surface plasmon resonance.* Langmuir, 2005. **21**(23): p. 10504-10508.
100. McFarland, A.D., et al., *Wavelength-scanned surface-enhanced Raman excitation spectroscopy.* The Journal of Physical Chemistry B, 2005. **109**(22): p. 11279-11285.
101. Cooney, R.P., et al., *Chemical reactivity and surface-enhanced raman scattering.* Chemical Physics Letters, 1981. **79**(3): p. 459-464.
102. Otto, A., *What is observed in single molecule SERS, and why?* Journal of Raman Spectroscopy, 2002. **33**(8): p. 593-598.
103. Sperling, R.A. and W.J. Parak, *Surface modification, functionalization and bioconjugation of colloidal inorganic nanoparticles.* Philosophical Transactions of the Royal Society A: Mathematical, Physical and Engineering Sciences, 2010. **368**(1915): p. 1333-1383.
104. Zhang, Y., et al., *Tunable and linker free nanogaps in core–shell plasmonic nanorods for selective and quantitative detection of circulating tumor cells by SERS.* ACS applied materials & interfaces, 2017. **9**(43): p. 37597-37605.
105. Fathima, H., et al., *Core–Shell Plasmonic Nanostructures on Au Films as SERS Substrates: Thickness of Film and Quality Factor of Nanoparticle Matter.* The Journal of Physical Chemistry C, 2021. **125**(29): p. 16024-16032.
106. Chen, L., et al., *Plasmonic-induced SERS enhancement of shell-dependent Ag@ Cu 2 O core–shell nanoparticles.* RSC advances, 2017. **7**(27): p. 16553-16560.
107. Alemán, J., et al., *Definitions of terms relating to the structure and processing of sols, gels, networks, and inorganic-organic hybrid materials (IUPAC Recommendations 2007).* Pure and Applied Chemistry, 2007. **79**(10): p. 1801-1829.
108. Meiklejohn, W.H. and C.P. Bean, *New magnetic anisotropy.* Physical Review, 1957. **105**(3): p. 904.
109. Decher, G., *Fuzzy nanoassemblies: toward layered polymeric multicomposites.* science, 1997. **277**(5330): p. 1232-1237.
110. Pazos-Perez, N., et al., *Modular assembly of plasmonic core–satellite structures as highly brilliant SERS-encoded nanoparticles.* Nanoscale Advances, 2019. **1**(1): p. 122-131.
111. Negrín-Montecelo, Y., et al., *Titanate Nanowires as One-Dimensional Hot Spot Generators for Broadband Au–TiO2 Photocatalysis.* Nanomaterials, 2019. **9**(7): p. 990.
112. Sakai, N., et al., *Layer-by-layer assembly of gold nanoparticles with titania nanosheets: control of plasmon resonance and photovoltaic properties.* Journal of Materials Chemistry, 2010. **20**(21): p. 4371-4378.
113. Mariño-Lopez, A., et al., *Microporous plasmonic capsules as stable molecular sieves for direct SERS quantification of small pollutants in natural waters.* ChemNanoMat, 2019. **5**(1): p. 46-50.
114. Zhang, Y.J., et al., *Plasmonic core–shell nanomaterials and their applications in spectroscopies.* Advanced Materials, 2021. **33**(50): p. 2005900.
115. Wang, K., et al., *Shell thickness-dependent Au@ Ag nanoparticles aggregates for high-performance SERS applications.* Talanta, 2019. **195**: p. 506-515.
116. Mohsin, M., et al., *An insight into the coating behavior of bimetallic silver and gold core-shell nanoparticles.* Plasmonics, 2020. **15**(6): p. 1599-1612.
117. Chen, Y., et al., *The study of surface plasmon in Au/Ag core/shell compound nanoparticles.* Plasmonics, 2012. **7**(3): p. 509-513.
118. Li, G.G., Z. Wang, and H. Wang, *Complementing Nanoscale Galvanic Exchange with Redox Manipulation toward Architectural Control of Multimetallic Hollow Nanostructures.* ChemNanoMat, 2020. **6**(7): p. 998-1013.
119. Oh, M.H., et al., *Galvanic replacement reactions in metal oxide nanocrystals.* Science, 2013. **340**(6135): p. 964-968.
120. Wang, L., et al., *Porous Au–Ag Nanoparticles from Galvanic Replacement Applied as Single-Particle SERS Probe for Quantitative Monitoring.* Small, 2022. **18**(1): p. 2105209.
121. Wang, L., et al., *Magnetic–plasmonic Ni@ Au core–shell nanoparticle arrays and their SERS properties.* RSC advances, 2020. **10**(5): p. 2661-2669.
122. Trang, N.T., et al., *Magnetic–plasmonic FePt@ Ag core–shell nanoparticles and their magnetic and SERS properties.* Plasmonics, 2013. **8**(2): p. 1177-1184.
123. Nguyen, T.T., et al., *Star-shaped Fe3-xO4-Au core-shell nanoparticles: From synthesis to SERS application.* Nanomaterials, 2020. **10**(2): p. 294.
124. Kutrovskaya, S., et al., *Nanocomposite Metamaterials Based on Self-assembled Titanium Dioxide Rolls with Embedded Gold Nanoparticles.* Scientific Reports, 2019. **9**(1): p. 1-7.
125. Xiong, W., et al., *The highly sensitive electrocatalytic sensing of catechol using a gold/titanium dioxide nanocomposite-modified gold electrode.* RSC Advances, 2014. **4**(61): p. 32092-32099.
126. Saud, P.S., et al., *Effective photocatalytic efficacy of hydrothermally synthesized silver phosphate decorated titanium dioxide nanocomposite fibers.* Journal of colloid and interface science, 2016. **465**: p. 225-232.
127. Yang, J., et al., *Highly sensitively detecting tetramethylthiuram disulfide based on synergistic contribution of metal and semiconductor in stable Ag/TiO2 core-shell SERS substrates.* Applied Surface Science, 2021. **539**: p. 147744.

128. Shanthil, M., et al., *Ag@ SiO2 core–shell nanostructures: distance-dependent plasmon coupling and SERS investigation.* The journal of physical chemistry letters, 2012. **3**(11): p. 1459-1464.
129. Batten, S.R., et al., *Terminology of metal–organic frameworks and coordination polymers (IUPAC Recommendations 2013).* Pure and Applied Chemistry, 2013. **85**(8): p. 1715-1724.
130. Eddaoudi, M., et al., *Modular chemistry: secondary building units as a basis for the design of highly porous and robust metal− organic carboxylate frameworks.* Accounts of chemical research, 2001. **34**(4): p. 319-330.
131. Ha, J., J.H. Lee, and H.R. Moon, *Alterations to secondary building units of metal–organic frameworks for the development of new functions.* Inorganic Chemistry Frontiers, 2020. **7**(1): p. 12-27.
132. Eddaoudi, M., et al., *Systematic design of pore size and functionality in isoreticular MOFs and their application in methane storage.* Science, 2002. **295**(5554): p. 469-472.
133. Kraft, A., *The history of Prussian blue*, in *Prussian Blue-Type Nanoparticles and Nanocomposites*. 2019, Jenny Stanford Publishing. p. 1-26.
134. Constable, E.C. and C.E. Housecroft, *Coordination chemistry: the scientific legacy of Alfred Werner.* Chemical Society Reviews, 2013. **42**(4): p. 1429-1439.
135. Yaghi, O.M., M.J. Kalmutzki, and C.S. Diercks, *Introduction to reticular chemistry: metal-organic frameworks and covalent organic frameworks*. 2019: John Wiley & Sons.
136. Hofmann, K. and F. Küspert, *Verbindungen von kohlenwasserstoffen mit metallsalzen.* Zeitschrift für anorganische Chemie, 1897. **15**(1): p. 204-207.
137. Nishikiori, S.-i. and T. Iwamoto, *Crystal structure of Hofmann-dma-type benzene clathrate bis (dimethylamine) cadmium (II) tetracyanonickelate (II)-benzene (2/1).* Chemistry Letters, 1984. **13**(3): p. 319-322.
138. Kinoshita, Y., I. Matsubara, and Y. Saito, *The crystal structure of bis (succinonitrilo) copper (I) nitrate.* Bulletin of the Chemical Society of Japan, 1959. **32**(7): p. 741-747.
139. Kinoshita, Y., I. Matsubara, and Y. Saito, *The crystal structure of bis (glutaronitrilo) copper (I) nitrate.* Bulletin of the Chemical Society of Japan, 1959. **32**(11): p. 1216-1221.
140. Kinoshita, Y., et al., *The crystal structure of bis (adiponitrilo) copper (I) nitrate.* Bulletin of the Chemical Society of Japan, 1959. **32**(11): p. 1221-1226.
141. Thommes, M., et al., *Physisorption of gases, with special reference to the evaluation of surface area and pore size distribution (IUPAC Technical Report).* Pure and applied chemistry, 2015. **87**(9-10): p. 1051-1069.
142. Zhang, X., et al., *A historical overview of the activation and porosity of metal–organic frameworks.* Chemical Society Reviews, 2020. **49**(20): p. 7406-7427.
143. Furukawa, H., et al., *The chemistry and applications of metal-organic frameworks.* Science, 2013. **341**(6149): p. 1230444.
144. He, T., X.-J. Kong, and J.-R. Li, *Chemically stable metal–organic frameworks: rational construction and application expansion.* Accounts of Chemical Research, 2021. **54**(15): p. 3083-3094.
145. Ding, M., X. Cai, and H.-L. Jiang, *Improving MOF stability: approaches and applications.* Chemical Science, 2019. **10**(44): p. 10209-10230.
146. Burtch, N.C., H. Jasuja, and K.S. Walton, *Water stability and adsorption in metal–organic frameworks.* Chemical reviews, 2014. **114**(20): p. 10575-10612.
147. Yang, K., G. Zhou, and Q. Xu, *The elasticity of MOFs under mechanical pressure.* RSC advances, 2016. **6**(44): p. 37506-37514.
148. Tan, J.C., T.D. Bennett, and A.K. Cheetham, *Chemical structure, network topology, and porosity effects on the mechanical properties of Zeolitic Imidazolate Frameworks.* Proceedings of the National Academy of Sciences, 2010. **107**(22): p. 9938-9943.
149. Shah, B.B., T. Kundu, and D. Zhao, *Mechanical properties of shaped metal-organic frameworks.* Metal-Organic Framework, 2020: p. 339-372.
150. Moggach, S.A., T.D. Bennett, and A.K. Cheetham, *The effect of pressure on ZIF-8: increasing pore size with pressure and the formation of a high-pressure phase at 1.47 GPa.* Angewandte Chemie International Edition, 2009. **48**(38): p. 7087-7089.
151. Zorlu, T., L. Guerrini, and R.A. Alvarez-Puebla, *The sensing applications of metal-organic frameworks and their basic features affecting the fate of detection*, in *Metal-Organic Frameworks for Chemical Reactions*. 2021, Elsevier. p. 271-293.
152. Burnett, B.J., P.M. Barron, and W. Choe, *Recent advances in porphyrinic metal–organic frameworks: materials design, synthetic strategies, and emerging applications.* CrystEngComm, 2012. **14**(11): p. 3839-3846.
153. Guselnikova, O., et al., *Metal-organic framework (MOF-5) coated SERS active gold gratings: A platform for the selective detection of organic contaminants in soil.* Analytica Chimica Acta, 2019. **1068**: p. 70-79.
154. Xu, H., et al., *Functionalized UIO-66@ Ag nanoparticles substrate for rapid and ultrasensitive SERS detection of di-(2-ethylhexyl) phthalate in plastics.* Sensors and Actuators B: Chemical, 2021. **349**: p. 130793.
155. Fu, J., et al., *UiO-66 metal-organic frameworks/gold nanoparticles based substrates for SERS analysis of food samples.* Analytica Chimica Acta, 2021. **1161**: p. 338464.
156. Li, H., et al., *A target-responsive release SERS sensor for sensitive detection of tetracycline using aptamer-gated HP-UiO-66-NH2 nanochannel strategy.* Analytica Chimica Acta, 2022: p. 339999.

157. Zheng, J., et al., *AgNPs and MIL-101 (Fe) self-assembled nanometer materials improved the SERS detection sensitivity and reproducibility.* Spectrochimica Acta Part A: Molecular and Biomolecular Spectroscopy, 2021. **251**: p. 119396.
158. Osterrieth, J.W., et al., *Core–shell gold Nanorod@ zirconium-based metal–organic framework composites as in situ size-selective Raman probes.* Journal of the American Chemical Society, 2019. **141**(9): p. 3893-3900.
159. Fu, J.H., et al., *SERS-active MIL-100 (Fe) sensory array for ultrasensitive and multiplex detection of VOCs.* Angewandte Chemie, 2020. **132**(46): p. 20670-20679.
160. Wang, Q., et al., *Rapid simultaneous adsorption and SERS detection of acid orange II using versatile gold nanoparticles decorated NH2-MIL-101 (Cr).* Analytica Chimica Acta, 2020. **1129**: p. 126-135.
161. Shao, Q., et al., *Ag@ MIL-101 (Cr) film substrate with high SERS enhancement effect and uniformity.* The Journal of Physical Chemistry C, 2021. **125**(13): p. 7297-7304.
162. Xia, Z., D. Li, and W. Deng, *Identification and detection of volatile aldehydes as lung cancer biomarkers by vapor generation combined with paper-based thin-film microextraction.* Analytical Chemistry, 2021. **93**(11): p. 4924-4931.
163. Huo, N., et al., *MOF-based hybrid film for multiphase detection of sulfur dioxide with colorimetric and surface-enhanced Raman scattering readout.* Chemical Engineering Journal, 2022. **432**: p. 134317.
164. Park, K.S., et al., *Exceptional chemical and thermal stability of zeolitic imidazolate frameworks.* Proceedings of the National Academy of Sciences, 2006. **103**(27): p. 10186-10191.
165. Phan, A., et al., *Synthesis, structure, and carbon dioxide capture properties of zeolitic imidazolate frameworks.* 2009.
166. Bhattacharjee, S., et al., *Zeolitic imidazolate frameworks: synthesis, functionalization, and catalytic/adsorption applications.* Catalysis Surveys from Asia, 2014. **18**(4): p. 101-127.
167. Wang, B., et al., *Colossal cages in zeolitic imidazolate frameworks as selective carbon dioxide reservoirs.* Nature, 2008. **453**(7192): p. 207-211.
168. Avci, C., *Zeolitic imidazolate framework-8: control of particle size and shape and its self-assembly*. 2019.
169. Tian, Y.Q., et al., *[Co5 (im) 10·2 MB]∞: A Metal-Organic Open-Framework with Zeolite-Like Topology.* Angewandte Chemie, 2002. **114**(8): p. 1442-1444.
170. Eddaoudi, M., et al., *Zeolite-like metal–organic frameworks (ZMOFs): design, synthesis, and properties.* Chemical Society Reviews, 2015. **44**(1): p. 228-249.
171. Huang, X., J. Zhang, and X. Chen, *[Zn (bim) 2]·(H2O) 1.67: A metal-organic open-framework with sodalite topology.* Chinese Science Bulletin, 2003. **48**(15): p. 1531-1534.
172. Huang, X.C., et al., *Ligand-directed strategy for zeolite-type metal–organic frameworks: zinc (II) imidazolates with unusual zeolitic topologies.* Angewandte Chemie International Edition, 2006. **45**(10): p. 1557-1559.
173. Awadallah-F, A., et al., *On the nanogate-opening pressures of copper-doped zeolitic imidazolate framework ZIF-8 for the adsorption of propane, propylene, isobutane, and n-butane.* Journal of materials science, 2019. **54**(7): p. 5513-5527.
174. Railey, P., et al., *Metal organic frameworks with immobilized nanoparticles: Synthesis and applications in photocatalytic hydrogen generation and energy storage.* Materials Research Bulletin, 2017. **96**: p. 385-394.
175. Yu, Y., et al., *Impact of 1-Methylimidazole on Crystal Formation, Phase Transitions, and Glass Formation in a Zeolitic Imidazolate Framework.* Crystal Growth & Design, 2020. **20**(10): p. 6528-6534.
176. Low, J.J., et al., *Virtual high throughput screening confirmed experimentally: porous coordination polymer hydration.* Journal of the American Chemical Society, 2009. **131**(43): p. 15834-15842.
177. Ania, C.O., et al., *Understanding gas-induced structural deformation of ZIF-8.* The Journal of Physical Chemistry Letters, 2012. **3**(9): p. 1159-1164.
178. Yin, H., et al., *Thermal stability of ZIF-8 under oxidative and inert environments: A practical perspective on using ZIF-8 as a catalyst support.* Chemical Engineering Journal, 2015. **278**: p. 293-300.
179. Wang, S., et al., *Enhancement thermal stability and CO2 adsorption property of ZIF-8 by pre-modification with polyaniline.* Materials Research Express, 2020. **7**(2): p. 025304.
180. Wang, Q., et al., *Synthesis and modification of ZIF-8 and its application in drug delivery and tumor therapy.* RSC advances, 2020. **10**(62): p. 37600-37620.
181. de Moura Ferraz, L.R., et al., *ZIF-8 as a promising drug delivery system for benznidazole: development, characterization, in vitro dialysis release and cytotoxicity.* Scientific reports, 2020. **10**(1): p. 1-14.
182. Yin, Z., et al., *Enzyme and Au nanoparticles encapsulated ZIF-8 for glucose responsive closed-loop drug delivery.* Materials Letters, 2021. **301**: p. 130276.
183. Esfahanian, M., M.A. Ghasemzadeh, and S.M.H. Razavian, *Synthesis, identification and application of the novel metal-organic framework Fe3O4@ PAA@ ZIF-8 for the drug delivery of ciprofloxacin and investigation of antibacterial activity.* Artificial Cells, Nanomedicine, and Biotechnology, 2019. **47**(1): p. 2024-2030.
184. Feng, S., et al., *Zeolitic imidazolate framework-8 (ZIF-8) for drug delivery: A critical review.* Frontiers of Chemical Science and Engineering, 2021. **15**(2): p. 221-237.
185. Velásquez-Hernández, M.d.J., et al., *Degradation of ZIF-8 in phosphate buffered saline media.* CrystEngComm, 2019. **21**(31): p. 4538-4544.
186. Poryvaev, A.S., et al., *Guest leakage from ZIF-8 particles under drug delivery conditions: quantitative characterization and guest-induced framework stabilization.* The Journal of Physical Chemistry C, 2021. **125**(28): p. 15606-15613.

187. Lu, D., et al., *Imidazole-bearing polymeric micelles for enhanced cellular uptake, rapid endosomal escape, and on-demand cargo release.* Aaps Pharmscitech, 2018. **19**(6): p. 2610-2619.
188. Spitsyna, A.S., et al., *Stability of ZIF-8 Nanoparticles in Most Common Cell Culture Media.* Molecules, 2022. **27**(10): p. 3240.
189. Taheri, M. and T. Tsuzuki, *Photo-accelerated hydrolysis of metal organic framework ZIF-8.* ACS Materials Letters, 2021. **3**(2): p. 255-260.
190. Gibbs, J.W., *The collected works of J. Willard Gibbs, volume I: thermodynamics*. 1928: Yale University Press.
191. Curie, P., *Sur la formation des cristaux et sur les constantes capillaires de leurs différentes faces.* Bulletin de Minéralogie, 1885. **8**(6): p. 145-150.
192. Wulff, G., *Xxv. zur frage der geschwindigkeit des wachsthums und der auflösung der krystallflächen.* Zeitschrift für Kristallographie-Crystalline Materials, 1901. **34**(1-6): p. 449-530.
193. Li, R., et al., *Gibbs–Curie–Wulff theorem in organic materials: a case study on the relationship between surface energy and crystal growth.* Advanced Materials, 2016. **28**(8): p. 1697-1702.
194. Whitesides, G.M. and B. Grzybowski, *Self-assembly at all scales.* Science, 2002. **295**(5564): p. 2418-2421.
195. Avci, C., et al., *Post-synthetic anisotropic wet-chemical etching of colloidal sodalite ZIF crystals.* Angewandte Chemie, 2015. **127**(48): p. 14625-14629.
196. Munn, A., et al., *Large-scale continuous hydrothermal production and activation of ZIF-8.* Chemical communications, 2015. **51**(64): p. 12811-12814.
197. Shi, Q., et al., *Synthesis of ZIF-8 and ZIF-67 by steam-assisted conversion and an investigation of their tribological behaviors.* Angewandte Chemie, 2011. **123**(3): p. 698-701.
198. Lee, Y.-R., et al., *ZIF-8: A comparison of synthesis methods.* Chemical Engineering Journal, 2015. **271**: p. 276-280.
199. Tanaka, S., et al., *Hierarchical pore development of ZIF-8 MOF by simple salt-assisted mechanosynthesis.* Crystal Growth & Design, 2018. **18**(1): p. 274-279.
200. Zeng, X., et al., *Sonocrystallization of ZIF-8 on electrostatic spinning TiO2 nanofibers surface with enhanced photocatalysis property through synergistic effect.* ACS Applied Materials & Interfaces, 2016. **8**(31): p. 20274-20282.
201. Tsai, C.-W. and E.H. Langner, *The effect of synthesis temperature on the particle size of nano-ZIF-8.* Microporous and Mesoporous Materials, 2016. **221**: p. 8-13.
202. Hara, N., et al., *Effect of temperature on synthesis of zif-8 membranes for propylene/propane separation by counter diffusion method.* Journal of the Japan Petroleum Institute, 2015. **58**(4): p. 237-244.
203. Bustamante, E.L., J.L. Fernández, and J.M. Zamaro, *Influence of the solvent in the synthesis of zeolitic imidazolate framework-8 (ZIF-8) nanocrystals at room temperature.* Journal of colloid and interface science, 2014. **424**: p. 37-43.
204. Malekmohammadi, M., et al., *A comparative study on ZIF-8 synthesis in aqueous and methanolic solutions: Effect of temperature and ligand content.* Solid State Sciences, 2019. **91**: p. 108-112.
205. Shi, Z., et al., *Water-based synthesis of zeolitic imidazolate framework-8 for CO 2 capture.* RSC advances, 2017. **7**(46): p. 29227-29232.
206. Bux, H., et al., *Zeolitic imidazolate framework membrane with molecular sieving properties by microwave-assisted solvothermal synthesis.* Journal of the American Chemical Society, 2009. **131**(44): p. 16000-16001.
207. Pan, Y., et al., *Rapid synthesis of zeolitic imidazolate framework-8 (ZIF-8) nanocrystals in an aqueous system.* Chemical Communications, 2011. **47**(7): p. 2071-2073.
208. Zhang, Y., et al., *Influence of the 2-methylimidazole/zinc nitrate hexahydrate molar ratio on the synthesis of zeolitic imidazolate framework-8 crystals at room temperature.* Scientific reports, 2018. **8**(1): p. 1-7.
209. Jian, M., et al., *Water-based synthesis of zeolitic imidazolate framework-8 with high morphology level at room temperature.* Rsc Advances, 2015. **5**(60): p. 48433-48441.
210. Ramu, G., M. Lee, and H.-K. Jeong, *Effects of zinc salts on the microstructure and performance of zeolitic-imidazolate framework ZIF-8 membranes for propylene/propane separation.* Microporous and Mesoporous Materials, 2018. **259**: p. 155-162.
211. Wang, Y., et al., *Zinc imidazolate metal–organic frameworks (ZIF-8) for electrochemical reduction of CO2 to CO.* ChemPhysChem, 2017. **18**(22): p. 3142-3147.
212. Sheng, L., et al., *Comparison of the hydrothermal stability of ZIF-8 nanocrystals and polycrystalline membranes derived from zinc salt variations.* Materials Letters, 2017. **197**: p. 184-187.
213. Pan, Y., et al., *Tuning the crystal morphology and size of zeolitic imidazolate framework-8 in aqueous solution by surfactants.* CrystEngComm, 2011. **13**(23): p. 6937-6940.
214. Yang, F., et al., *Morphological map of ZIF-8 crystals with five distinctive shapes: feature of filler in mixed-matrix membranes on C3H6/C3H8 separation.* Chemistry of Materials, 2018. **30**(10): p. 3467-3473.
215. Zheng, G., et al., *Shape control in ZIF-8 nanocrystals and metal nanoparticles@ ZIF-8 heterostructures.* Nanoscale, 2017. **9**(43): p. 16645-16651.
216. Peralta, D., et al., *Comparison of the behavior of metal–organic frameworks and zeolites for hydrocarbon separations.* Journal of the American Chemical Society, 2012. **134**(19): p. 8115-8126.
217. Liu, X.-L., et al., *Rapid and Wide-Range Detection of NO x Gas by N-Hyperdoped Silicon with the Assistance of a Photovoltaic Self-Powered Sensing Mode.* ACS sensors, 2019. **4**(11): p. 3056-3065.

218. Vashpanov, Y., et al. *Photovoltaic intelligent gas sensors for the detection of acetone concentration over a wide range of measurement for biomedical applications and tasks of public safety*. in *IOP Conference Series: Materials Science and Engineering*. 2020. IOP Publishing.
219. Honeycutt, W.T., M.T. Ley, and N.F. Materer, *Precision and limits of detection for selected commercially available, low-cost carbon dioxide and methane gas sensors.* Sensors, 2019. **19**(14): p. 3157.
220. Kreno, L.E., et al., *SERS of molecules that do not adsorb on Ag surfaces: A metal–organic framework-based functionalization strategy.* Analyst, 2014. **139**(16): p. 4073-4080.
221. Chen, Q.-Q., et al., *Au@ ZIF-8 Core–Shell Nanoparticles as a SERS Substrate for Volatile Organic Compound Gas Detection.* Analytical Chemistry, 2021. **93**(19): p. 7188-7195.
222. Phan-Quang, G.C., et al., *Tracking Airborne Molecules from Afar: Three-Dimensional Metal–Organic Framework-Surface-Enhanced Raman Scattering Platform for Stand-Off and Real-Time Atmospheric Monitoring.* ACS nano, 2019. **13**(10): p. 12090-12099.
223. Koh, C.S.L., et al., *Plasmonic nose: integrating the MOF-enabled molecular preconcentration effect with a plasmonic array for recognition of molecular-level volatile organic compounds.* Chemical Communications, 2018. **54**(20): p. 2546-2549.
224. Huang, K., et al., *Ultrathin ZIF-8 wrapping on Au-dotted Ag-nanowires for highly selective SERS-based CO 2 gas detection.* Chemical Communications, 2021. **57**(17): p. 2144-2147.
225. De Marchi, S., et al., *Plasmonic Au@ Ag@ mSiO2 Nanorattles for In Situ Imaging of Bacterial Metabolism by Surface-Enhanced Raman Scattering Spectroscopy.* ACS applied materials & interfaces, 2021. **13**(51): p. 61587-61597.
226. Qiao, X., et al., *Selective surface enhanced Raman scattering for quantitative detection of lung cancer biomarkers in superparticle@ MOF structure.* Advanced materials, 2018. **30**(5): p. 1702275.
227. Hu, P., et al., *Surfactant-directed atomic to mesoscale alignment: Metal nanocrystals encased individually in single-crystalline porous nanostructures.* Journal of the American Chemical Society, 2014. **136**(30): p. 10561-10564.
228. Fu, Y., et al., *Plasmonic gold nanostars@ ZIF-8 nanocomposite for the ultrasensitive detection of gaseous formaldehyde.* Journal of Materials Science, 2021. **56**(6): p. 4151-4160.
229. Lafuente, M., et al., *Plasmonic MOF thin films with Raman internal standard for fast and ultrasensitive SERS detection of chemical warfare agents in ambient Air.* ACS sensors, 2021. **6**(6): p. 2241-2251.
230. Zhou, X., et al., *Porous zeolite imidazole framework-wrapped urchin-like Au-Ag nanocrystals for SERS detection of trace hexachlorocyclohexane pesticides via efficient enrichment.* Journal of hazardous materials, 2019. **368**: p. 429-435.
231. Yang, J., et al., *Effective adsorption and in-situ SERS detection of multi-target pesticides on fruits and vegetables using bead-string like Ag NWs@ ZIF-8 core-shell nanochains.* Food Chemistry, 2022. **395**: p. 133623.
232. Ye, C., et al., *ZIF-8 derived TiO2/ZnO heterostructure decorated with AgNPs as SERS sensor for sensitive identification of trace pesticides.* Journal of Alloys and Compounds, 2022. **901**: p. 163675.
233. Jiang, L., et al., *In Situ Monitoring of Hydrogen Peroxide Released from Living Cells Using a ZIF-8-Based Surface-Enhanced Raman Scattering Sensor.* Analytical Chemistry, 2021. **93**(37): p. 12609-12616.
234. De Marchi, S., et al., *Programmable modular assembly of functional proteins on Raman-encoded zeolitic imidazolate framework-8 (ZIF-8) nanoparticles as SERS tags.* Chemistry of Materials, 2020. **32**(13): p. 5739-5749.
235. Sun, D., et al., *Tumor microenvironment-activated degradable multifunctional nanoreactor for synergistic cancer therapy and glucose SERS feedback.* IScience, 2020. **23**(7): p. 101274.
236. Wang, Y., et al., *Carbon nanodots in ZIF-8: synthesis, tunable luminescence and temperature sensing.* Inorganic Chemistry Frontiers, 2018. **5**(11): p. 2739-2745.
237. Tatykayev, B., et al., *Synthesis of core/shell ZnO/rGO nanoparticles by calcination of ZIF-8/rGO composites and their photocatalytic activity.* ACS omega, 2017. **2**(8): p. 4946-4954.
238. Wu, M., et al., *A poly (ethylenglycol) functionalized ZIF-8 membrane prepared by coordination-based post-synthetic strategy for the enhanced adsorption of phenolic endocrine disruptors from water.* Scientific reports, 2017. **7**(1): p. 1-11.
239. Deng, X., et al., *Yolk–shell structured Au nanostar@ metal–organic framework for synergistic chemo-photothermal therapy in the second near-infrared window.* Nano Letters, 2019. **19**(10): p. 6772-6780.
240. Hu, M., et al., *Void engineering in metal–organic frameworks via synergistic etching and surface functionalization.* Advanced Functional Materials, 2016. **26**(32): p. 5827-5834.
241. Zhao, G., et al., *Heteroatoms doped yolk-shell hierarchically porous carbon derived from ZIF-8 for electrochemical sensing.* Carbon, 2021. **183**: p. 291-300.
242. Kuo, C.-H., et al., *Yolk–shell nanocrystal@ ZIF-8 nanostructures for gas-phase heterogeneous catalysis with selectivity control.* Journal of the American Chemical Society, 2012. **134**(35): p. 14345-14348.
243. Zhao, Y., et al., *A smart route for encapsulating Pd nanoparticles into a ZIF-8 hollow microsphere and their superior catalytic properties.* Langmuir, 2020. **36**(8): p. 2037-2043.
244. Yang, J., et al., *Hollow Zn/Co ZIF particles derived from core–shell ZIF-67@ ZIF-8 as selective catalyst for the semi-hydrogenation of acetylene.* Angewandte Chemie, 2015. **127**(37): p. 11039-11043.

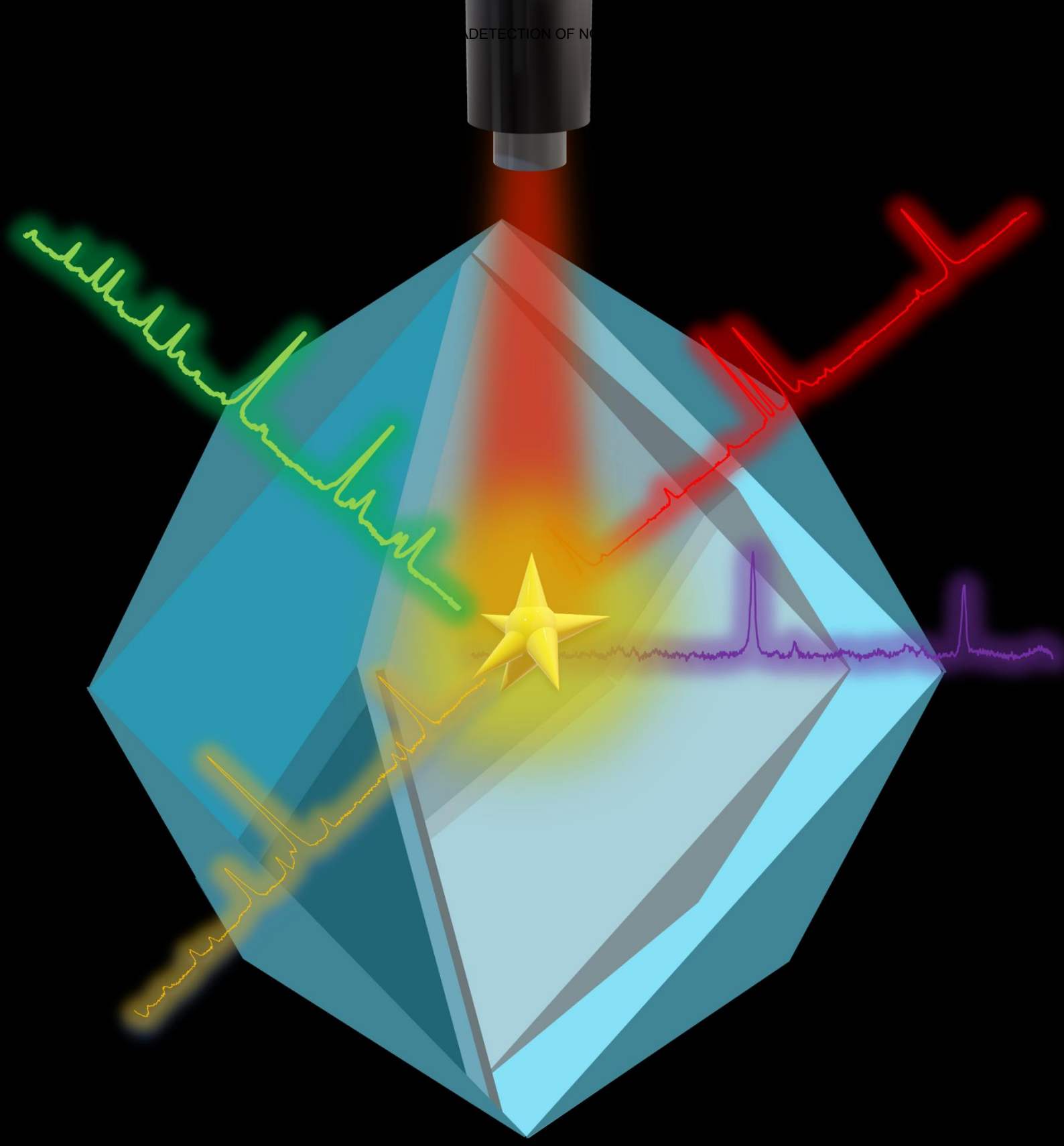

CHAPTER TWO

Yolk Shell Nanostars@Metal Organic Frameworks as Molecular Sieves for Optical Sensing and Catalysis

Hybrid composites between NPs and MOFs had been described as optimal materials for a wide range of applications in optical sensing, drug delivery, pollutant removal or catalysis. These materials are usually core-shell single- or multi-NPs, restricting the inorganic surface available for reaction. Here we develop a method for the preparation of yolk-shells consisting in a plasmonic Au NS coated with MOF. This configuration shows more colloidal stability, can sieve different molecules based on their size or charge, seems to show some interesting synergy with gold for their application in photocatalysis and present strong optical activity to be used as SERS sensors.

2.1. Introduction

Composite materials comprising plasmonic cores coated with inorganic oxides or polymers are not new [1]. These materials have been extensively engineered to improve colloidal stability, to restrict the reactivity or to impart physical and/or chemical selectivity. Conversely, formats of these composites range from single particles [2] to several aggregates [3] or semi-isolated particles [4] coated with the desired material. Additionally, composites can be obtained as regular core-shell [1] or yolk-shell [5] materials. These composites have found applications in fields such as sensing [6], drug delivery [7], and catalysis [8] among others. However, these coatings commonly present a heterogeneous collection of pore sizes, a critical parameter for these applications.

MOFs have shown outstanding performance in various strategic applications such as separation, catalysis or sensing and drug delivery systems [9]. The strength of MOF-based materials arises of their structure-dependent regular network of voids (with diameters up to 6 nm) [10], which are defined by inorganic cations interconnected by polydentate organic ligands. Since the late 1990s intense synthetic efforts have been devoted to report novel MOFs (over 20,000 structures) in terms of crystal size, porosity, geometry, and functionality [9, 11]. More recently, composites containing plasmonic NPs had been prepared in a variety of morphologies for a diversity of applications as sensors [12], catalyst [13], and drug delivery scaffolds [14]. These composites combine the optical/catalytic properties of the plasmonic NPs with the structural properties of the MOFs which, together with the high surface area due to a vast porosity of a very homogeneous distribution [15], may offer additional chemical selectivity based on the ligands used in the coordination of the metal [16].

As other hybrid materials NP@MOF composites can be prepared coating single or multiple (isolated and aggregated) NPs [17]. However, these core-shell approaches notably restrict the availability of the plasmonic surfaces limiting their capacity to interact with the target analytes or molecular substrates and restricting, as well their storage capacity to be used as drug delivery systems [5].

Herein we demonstrate the possibility of confining single plasmonic particles into a water-soluble MOF that can be recoated with a water-insoluble MOF to create a yolk-shell.

Optical performance as well as retention kinetics in multianalyte experiments and plasmonic catalysis are also studied.

2.2. Results and Discussion

Notably although similar structurally ZIF MOFs present different physicochemical properties. For example, the cobalt (II) and zinc (II) derived ZIFs ([Zn(2-methylimidazole)$_2$]n, ZIF-8 and [Co(2-methylimidazole)$_2$]n, ZIF-67) consist in tetrahedral crystals that share a quasi-identical sodalite topology. However, while ZIF-67 is soluble in water, ZIF-8 is much more resistant, both at room temperature (Figure 2.1A). Thus, taking advantage of this property, it is possible to produce yolk-shells consisting in single Au NS coated of ZIF-8 (Figure 2.1B). Au NS of 70 nm (tip-to-tip) were produced though a seed mediated method (Figure 2.1B) [18]. These NPs were selected as they are single-particle electromagnetic hot spots in the near IR [19]. Then, preparation of yolk-shell structures was achieved by initially coating the NS with ZIF-67, followed by the growth of the ZIF-8 to create a ZIF-67@ZIF-8 double shell. NS@ZIF-8 yolk-shell can be then spontaneously prepared by immersing the NS@ZIF-67@ZIF-8 in water and sonicating for 24 hours (Figures 2.1B and C) [20]. Notably, while the violet solution of the core-shell particles rapidly turns to colorless in few minutes, in the case of yolk-shells, the presence of the outer ZIF-8 layer delays the ZIF-67 dissolution (Figure 2.1D).

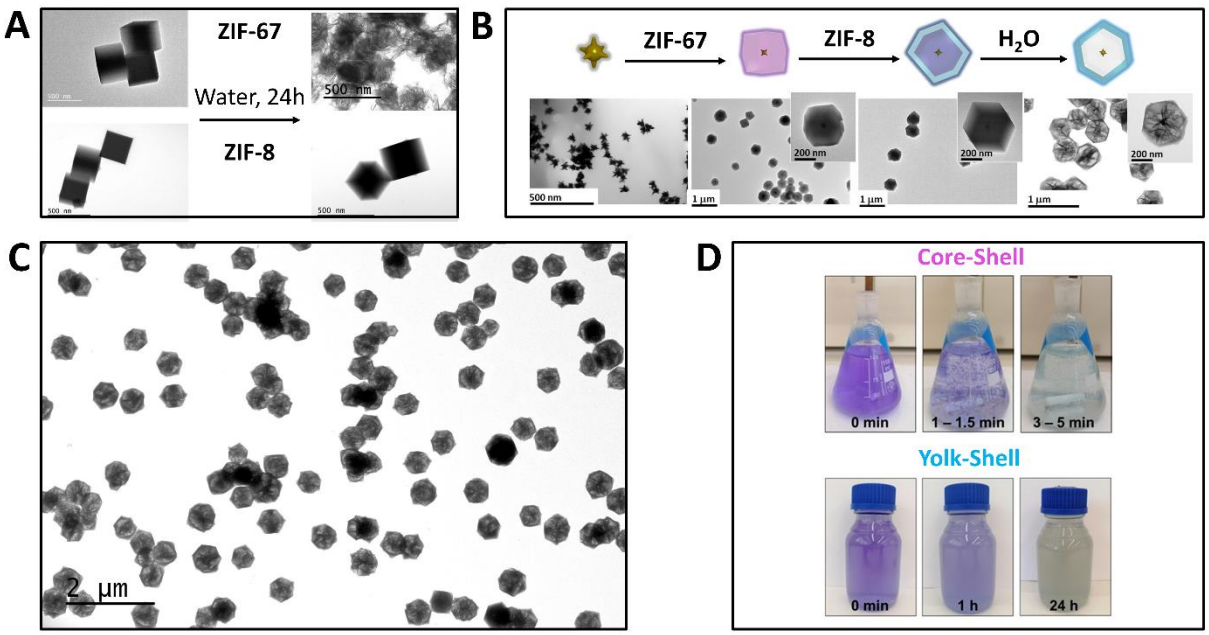

Figure 2.1. ***(A)*** *Water solubility of ZIF-67 as compared with ZIF-8 after 24h.* ***(B)*** *Conceptual scheme for the preparation of NS@ZIF-67 core-shells and NS@ZIF-8 yolk-shells and representative TEM images of the different materials.* ***(C)*** *TEM images of yolk-shell NS@ZIF-8 particles.* ***(D)*** *Optical images of NS coated with ZIF-67 (core-shell) and ZIF-67@ZIF-8 (yolk-shell) redispersed in water as a function of time*.

To assess the composition of the produced materials, EDX analysis was carried out in a high-resolution TEM. As shown in Figure 2.2, core-shell structures present signals of gold and cobalt, correspondent to the Au NS and the coating ZIF-67, respectively. In the case of the intermediate NS@ZIF-67@ZIF-8, and additional signal arises at the outer surface due to the zinc ions of the ZIF-8. Upon dissolution of the inner ZIF-67 structure, the Zn signal remains in the outer shell while traces of the cobalt signal remain. This reminiscent signal can be attributed to the spontaneous formation of some layered cobalt oxides as this cation detaches from the MOF [21], as also indicated by the TEM images (Figures 2.1B and C).

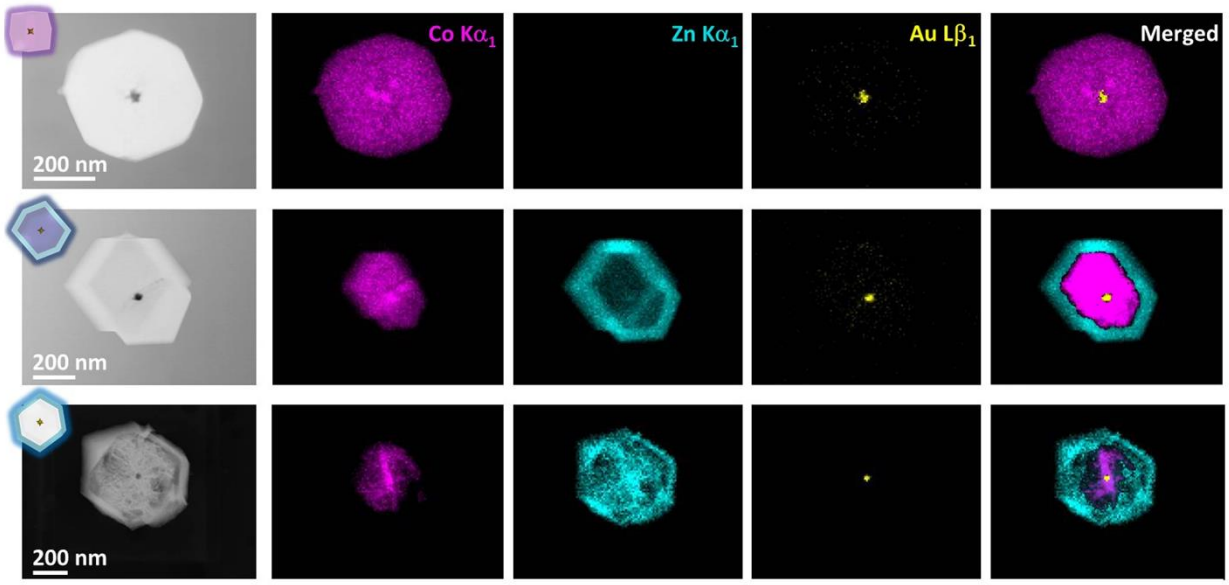

Figure 2.2. *High resolution TEM images and EDX analysis of the Au NS@ZIF-67 and Au NS@ZIF-67@ZIF-8 core-shells and the Au NS@ZIF-8 yolk-shell.*

PXRD patterns of the samples (Figure 2.3A) exhibit sharp bands that correspond to the sodalite structures of crystalline ZIF-8 and ZIF-67 in both core- and yolk-shell structures [22]. The absence of any other signals demonstrates the phase purity of the MOFs but also the epitaxial growth of ZIF-8 on ZIF-67. This is expected due to the similar sizes of the unit cell for ZIF-8 (a = b = c = 16.9910 Å) [23] and ZIF-67 (a = b = c = 16.9589 Å) [24]. The structure remains unchanged after the removal of the ZIF-67 in water. N_2 adsorption isotherms (Figure 2.3B) of the core- and yolk-shells show the typical reversible type I isotherm, as previously observed for pure ZIF-8 and ZIF-67 crystals.

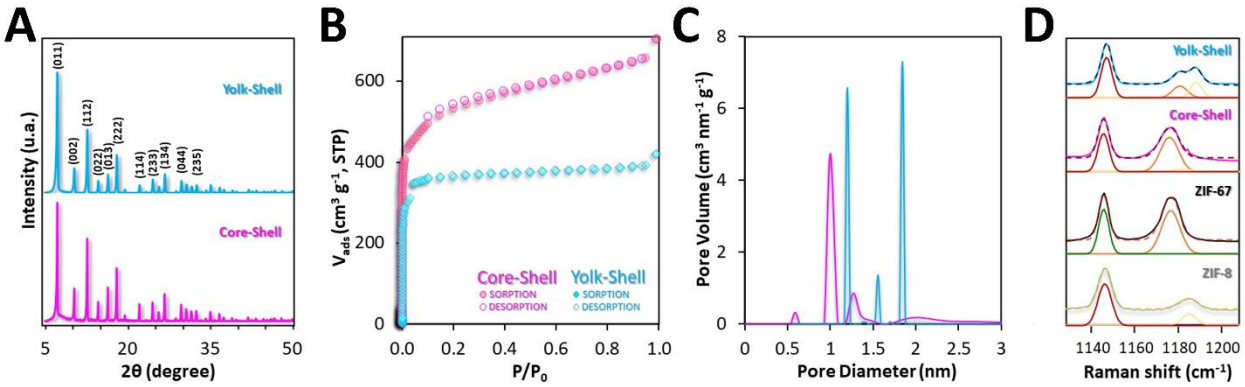

Figure 2.3. ***(A)*** *PXRD,* ***(B)*** *N_2 sorption isotherms (77 K),* ***(C)*** *BJH pore size analysis, and* ***(D)*** *Raman spectroscopy for the Au NS@ZIF-67 core-shells and the Au NS@ZIF-8 yolk-shells*

For both, the amount of adsorbed N_2 rapidly increases at low pressures, indicating the existence of micropores [25]. BET analysis of the isotherms indicates surface areas over 1700 and 1100 $m^2\ g^{-1}$ for the core- and the yolk-shell structures, respectively. These values also fall within the common range reported for pristine ZIF particles [26]. Notably, the difference in surface area, is related to the shell thickness of the composites, while in Au NS@ZIF-67 core-shell exhibits a continuous shell of 160 nm, the yolk-shell particles show an outer shell of only 50 nm. Porosity, derived from the isotherms through the BJH pore size analysis, also shows different distributions for core- and yolk-shells (Figure 2.3C). While Au NS@ZIF-67 core-shell exhibits most of its porosity at 1 nm, with small contributions at 0.6 and 1.3 nm, pore distribution of Au NS@ZIF-8 yolk-shell shows larger pores, at 1.2 and 1.9 nm, with a smaller contribution at 1.6 nm. Although ZIF-67 and ZIF-8 present similar pore distributions in large crystals the epitaxial growth of ZIF-8 on ZIF-67, and the posterior removal of ZIF-67 have two main effects in the structure of the yolk-shell. First, the growth, by itself, of a MOF on the surface of a NP slightly enlarge the pores as the shell grows [27]. Second, the removal of the sacrificial ZIF-67 increases the flexibility of the ZIF-8 yolk-shell due to the removal of the mechanical support imparted by ZIF-67. Finally, Raman spectroscopy was carried out on the composites in solid phase (Figure 2.3D and 2.4A). In the case of the pure ZIF crystals, the vibrational spectra are dominated by the characteristic vibrational modes of the ZIFs (imidazole ring puckering, 685 cm^{-1}, the CN stretching, 1146 cm^{-1} and the CCH waging, 1460 cm^{-1}) [14]. However, a detailed observation of the area between 1100 and 1200 cm^{-1} (Figure 3.3C) indicates a slight difference (1178 and 1187 cm^{-1} for ZIF-67 and ZIF-8, respectively) in the band

assigned to the CN stretching plus the NH wagging [28], which is affected by the nature of the coordinated metal. This vibrational detail can be exploited to gain information about the composition of the composite materials. The fine deconvolution of the CN stretching, and CN stretching plus the NH wagging bands clearly shows that while the Au NS@ZIF-67 core-shell can be deconvoluted in just to bands, three bands are necessary for the yolk-shell. Considering the low contribution of the 1178 cm^{-1} ZIF-67 signal (which is similar to the CN stretching in the ZIF-67 pure crystal) and the distance to the surface of ZIF-8 (much distant than ZIF-67, with the subsequent less SERS effect in the intensity of its spectrum) it becomes clear that the presence of Co(II) is reminiscent in the yolk-shell.

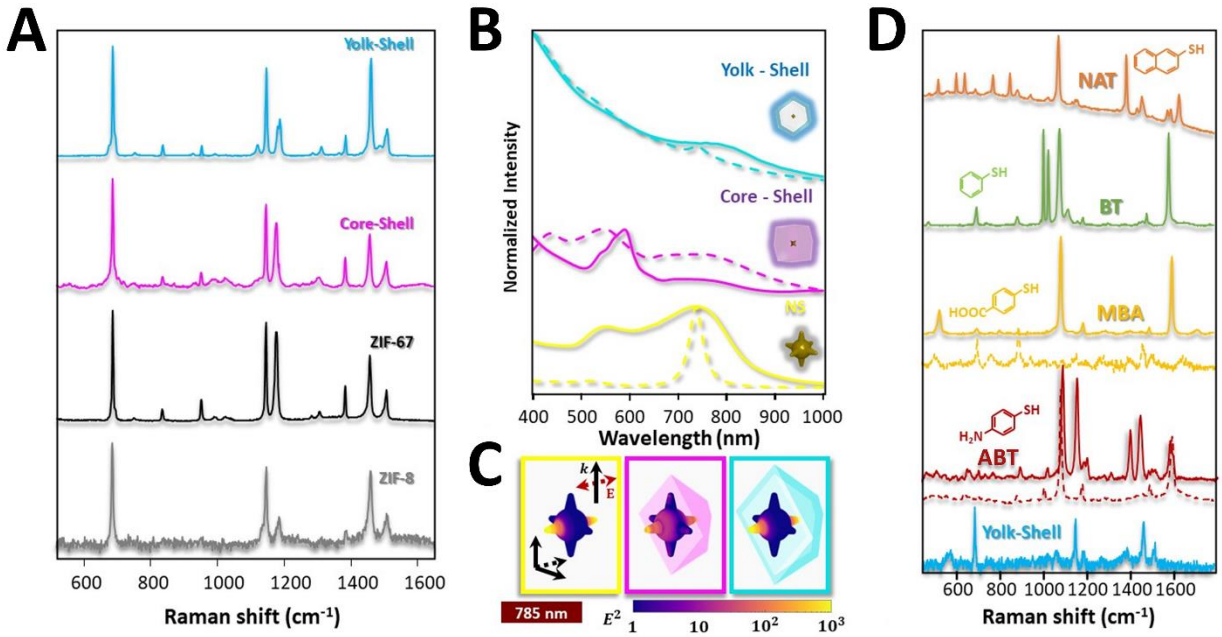

*Figure 2.4. **(A)** Raman spectrum of powder ZIF-8, ZIF-67, core- and yolk-shells. **(B)** Experimental (solid line) and calculated (dashed) extinction and **(C)** local electric field distribution at 785 nm for Au NS and its core-shell composite with ZIF-67 and yolk-shell composite with ZIF-8. **(D)** SERS spectra of micromolar solution of NAT, BT, MBA, and ABT on the NS (dashed lines) and yolk-shells (solid lines). For reference, the spectrum of the yolk-shell solution without analyte is also shown.*

Figure 2.4B, show the experimental and simulated optical response for Au NS, Au NS@ZIF-67 core-shell, and Au NS@ZIF-8 yolk-shell. The spectra simulated for the NS and the yolk-shell present a good agreement with the experimental results. However, the theoretical spectrum of the core-shell shows slight differences compared to the experimental, which can

be attributed to the imaginary part of the dielectric constant of the MOF, which we assumed to be zero in the simulations to make the calculation treatable [29]. This approximation gives sharper theoretical resonances compared with the experiments. Electric near field (Figure 2.4C) shows similar enhancements for the single NS and the yolk-shell system; this is expected because the ZIF-8 slightly attenuates the incident light that reaches the NS, slightly diminishing the intensity of the near-field enhancement. On the other hand, results for the core-shells show a lower enhancement as compared with stars and yolk-shells. This is due to the proximity of the ZIF-67 to the plasmonic structure which, in fact, increases the local refractive index (of the liquid solution); this implies a redshift of the resonances and dumps the enhancement as the plasmon resonance.

To test for the optical enhancing properties for SERS [30], the different materials, NS, core- and yolk-shells were exposed to 4 different analytes; NAT, BT, MBA, and ABT. Analytes were added to the plasmonic solutions to set a final concentration of 10^{-6} M. Spectra were recorded after 30 min, usually time enough for the chemisorption reaction to be completed (Figure 2.4D) [31]. Notably, NAT and BT yield strong signals on all the substrates. MBA, however, only produce remarkable intensity on the bare NS, with no evidence of its presence on both core- and yolk-shells. Finally, ABT shows only its characteristic spectrum on the NS, while in the case of the composite materials the signals obtained can be ascribed to DMAB, a product derived from the plasmonic driven catalytical dimerization of ABT [32]. Further, for all the analytes, but ABT (or DMAB), SERS intensity on NS resulted consistently better than that obtained on the composite materials. This fact contrasts with the literature which often considers the plasmonic NPs coated with MOFs as an example of optical accumulators [33, 34]. Thus, to further investigate this point, we designed a set of experiments based on the adsorption kinetics of single probes as compared with the same probes in the presence of the rest (Figure 2.5).

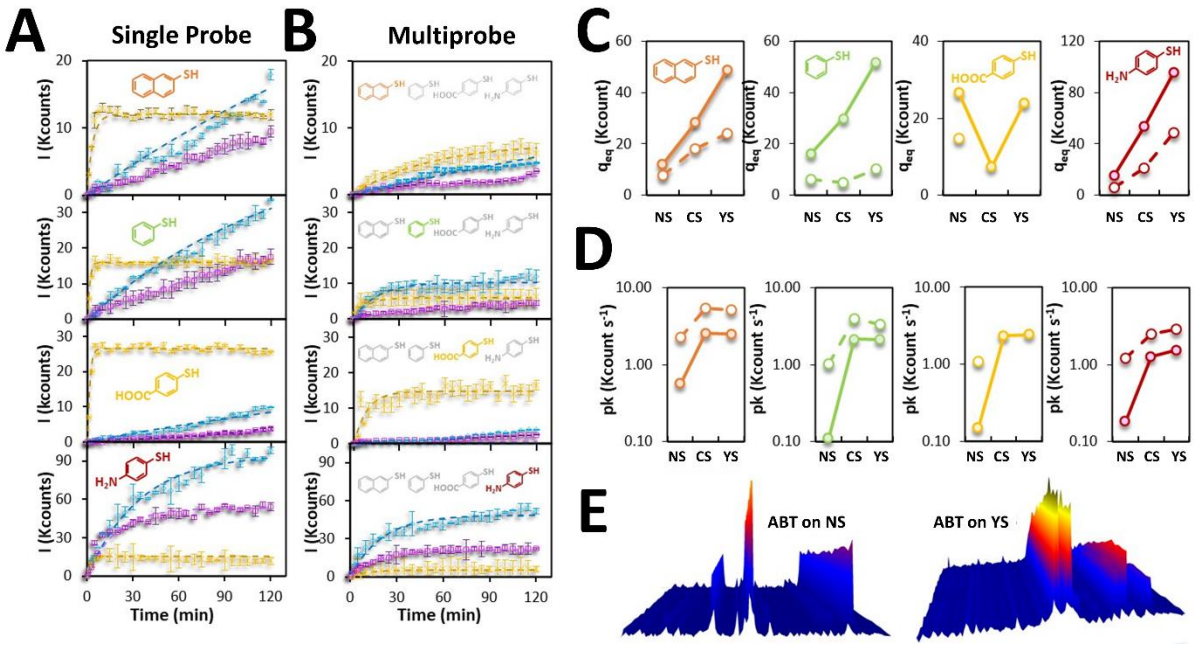

Figure 2.5. *Adsorption kinetics of micromolar solutions NAT, BT, MBA, and ABT on the NS, core- and yolk-shells* ***(A)*** *as single probes and* ***(B)*** *in a mixture containing all the molecules.* ***(C)*** *Adsorption capacity at the equilibrium and* ***(D)*** *rate constant for the kinetics (solid line, single probe; dashed line, multiprobe).* ***(E)*** *Three-dimensional representation of the kinetic adsorption of ABT on NS and on the yolk-shells.*

For that, colloidal solutions were set at pH 7.8 with analyte concentrations of 10^{-6} M (either just one or all the analytes). The examination of the temporal response of the analyte spectral intensities reveals an exponential rise to maximum curve. Thus, when the analyte collides with the adsorbent, it will chemically bind to the plasmonic surface, or it will return to the aqueous phase, which indicates a pseudo-first-order chemical kinetics [12, 35]:

$$q_t = q_{eq}\,(1 - e^{-kt}) \qquad (2.1)$$

where q_t is the amount adsorbed by the adsorbent at any time; q_{eq}, the adsorption capacity at the equilibrium (or amount adsorbed by the adsorbent at the equilibrium); k, rate constant and t, the time of reaction. Assuming that, in a liquid colloidal suspension without aggregation, the SERS intensity is equivalent to the amount adsorbed this equation (equation 1) can be used to fit the kinetic data of the probes to obtain the rate constants [36].

To give an interpretation of the kinetic results, zeta potential of the colloidal solutions was measured resulting in values of -29, 25, and 11 mV for the NS, core- and, yolk-shells, respectively. Conversely, molecular size of the analytical probes was calculated by using DFT at the B3LYP 6-311G (d,p) the level of theory (Figure 2.6A) resulting in a molecular volume tendency of NAT > MBA > ABT > BT. In general, all the analytes are adsorbed faster (and in a larger quantity) when they are alone as compared when they are in the mixture between themselves. This fact is expected as single probes have not competition with other adsorbates. Further, although NS tend to adsorb faster, adsorption capacity is maximized in yolk-shells. This indicates that the sieving layer, provided by the MOF, restricts the pass of the analyte, but favor the accumulation on the plasmonic surface once into the shell as expected in an optical accumulator [6]. Notably, this effect is more noticeable in the case of yolk-shells as they are hollow and their plasmonic surface much more available. Related with this, it is important to mention that the MOF coating also increases colloidal stability. For example, after 2h, NS tend to precipitate when the analyte is ABT (Figure 2.6B) while both composites remain stable. Considering the differences between analytes, it can be stated that for neutral molecules such as NAT and BT size is an important parameter as, although it does not affect the retention capacity, it slows the sorption process for the larger entities. On the other hand, analyte charge is a key factor. At pH 7.8 all the analytes but MBA are neutral. At this pH, MBA is ionized as mercaptobenzoate (i.e., marked with an explicit negative charge). Notwithstanding, this molecule is readily adsorbed on NS, which are eminently negative, but not in core of yolk-shells, which exposes a positively charged surface. This surprising behavior results very likely from an extraordinary electrostatic affinity between the MOF and the MBA which clogs the pores. This clogging process does not affect the rest of analytes in the multiprobe experiments. If it is true that in such experiments, both rate constant and retention capacity decreases as compared with those of single probe, the decrease of kinetic constants and the retention capacity is very likely derived of the competence between the different probes.

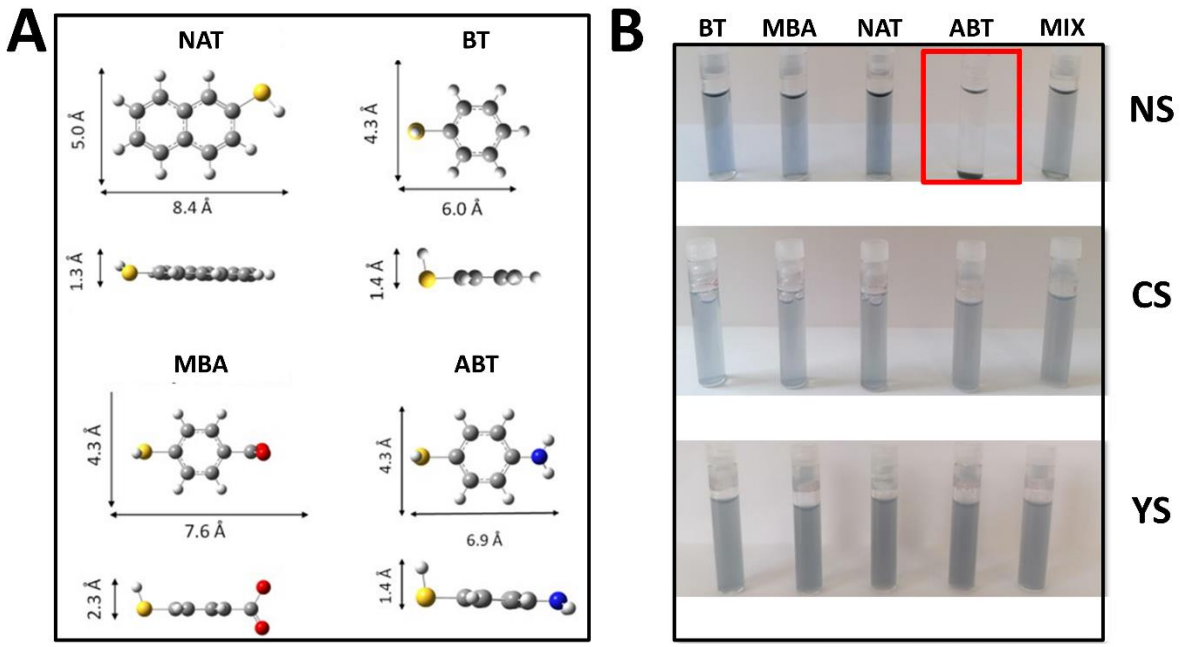

Figure 2.6. (A) *DFT calculations of the electronic structures and size of the different molecular probes.* ***(B)*** *Colloidal suspensions of Au NS, core- and yolk-shells with each of the analytes and with a mixture of all the analytes after 2h.*

The sorption of ABT shows a different behavior as compared with the rest of the probes (Figure 2.5E). ABT retention in NS shows the typical SERS spectrum of such molecule during all the acquisition time until aggregation. Notwithstanding, when measured either on core- or yolk-shells, the resulting spectrum is no longer ABT but DMAB. The dimerization of this molecule is an example of plasmonic catalysis and has been described upon illumination of plasmonic sols in an excess of ABT [37], in lower ABT concentrations when plasmonic NPs are functionalized with platinum [32] or when a ABT monolayer is deposited in a plasmonic electrode [38]. Briefly ABT oxidizes to DMAB by losing 2e (or gaining 2 holes). Oxidation of ABT on gold surfaces a thermodynamically nonspontaneous reaction. Plasmon excitation and subsequent decay in metal NPs create hot electrons and hot holes with an energy distribution above and below the Fermi level. When the LUMO or HOMO energies of the molecules are within the energy distribution, hot charge carriers are allowed to transfer to the molecules, leading to the reduction or oxidation of the molecules. Here, ZIF to increases the local concentration of ABT helping the retention onto the Au NS. This process, although also present

in the core-shells, is of lesser extension due to the smaller plasmonic surface area allowed by the compact thick shell of ZIF and its smaller hollow volume.

2.3. Conclusions

In summary, we described a simple and effective synthetic method for the fabrication of single Au NS encapsulated into hollow ZIF-8 yolk-shells. The resulting materials are characterized by three main features: (1) the electromagnetic response of isolated Au NS even in concentrated solution or even cast on surface; (2) the homogeneous porous distribution characteristic of MOF materials; and (3) the availability of a large volume between the plasmonic core and the sieving shell that can be exploited for optical accumulation, catalysis or drug storage. These materials are more colloidally stable than their counterparts without coating, can sieve different molecules based on their size or charge, seems to show some interesting synergy with gold for their application in photocatalysis and present strong optical activity to be used as SERS sensors. Further, the dependence of the SERS signal with time can be also used to design advanced analytical applications based in the adsorption time (kinetic control) or the stability (thermodynamic stability).

2.4. Experimental Section

2.4.1. Materials

$HAuCl_4$ (99.9%), zinc acetate dihydrate ((98%), $Zn(CH_3COO)_2{\cdot}2H_2O$), mIm (99%), cobalt(II) nitrate hexahydrate (98%, $Co(NO_3)_2{\cdot}6H_2O$), PVP, (MW: 10K), trisodium citrate dihydrate (98%), $AgNO_3$ (99%), MBA (90%), BT (95%), ethanol (99.5%), methanol (99.9%), DMF (99%), NAT (99%), and ABT (≥97%) were purchased from Sigma-Aldrich. CTAB (99+%) was purchased from Acros Organics. PVP (MW: 24K) was purchased from Carl Roth Chemicals. All reactants were used without further purification. Milli-Q water (18 MΩ cm^{-1}) was used in all aqueous solutions, and all the glassware was cleaned with aqua regia before the experiments.

2.4.2. Synthesis of PVP-Coated Au Seeds

Au seeds were produced by a modification of the well-known Turkevich method [39, 40]. Briefly, 5 mL of a 34 mM sodium citrate aqueous solution were added to 100 mL of a boiling 0.5 mM $HAuCl_4$ aqueous solution under vigorous stirring. The boiling mixture was allowed to react for one hour under stirring. The synthesis yielded spherical nanoparticles of 14.5 ± 1.7 nm size, with a Au^0 concentration of 2.64 mM. The obtained nanoparticles were subsequently coated with PVP (MW: 10K). Specifically, 10 mL of an aqueous PVP (100 mg/mL) was added dropwise to a vial containing 10 mL of an aqueous Au seed solution ($[Au^0]$ = 1 mM) under stirring (600 rpm). The mixture was left under stirring for 24 h at RT to maximize PVP adsorption. The as-prepared PVP-coated Au seeds were centrifuged five times (4500 rpm, 45 min). In every centrifugation step, the pellet was redispersed in ethanol and the supernatant continued to be centrifuged until the supernatant turn to colorless. Finally, the seeds redispersed in ethanol to a $[Au^0]$ = 1 mM, which approximately corresponds to a concentration of Au seeds equals to = 9.6 nM.

2.4.3. Synthesis of PVP-Coated Au NS

Au NS were prepared as reported previously [18]. Briefly, 5 gr of PVP (MW: 25K) were dissolved into 25 mL of DMF. Then, 550 µL of PVP-coated Au seeds in ethanol ($[Au^0]$ = 1 mM) were added to the solution, followed by the injection of 86.25 µL of a $HAuCl_4$ aqueous solution (0.1302 M), The solution was vortexed for 10 seconds and let to rest overnight. The obtained

colloids were submitted to 5 washing cycles consisting of centrifugations at, first, 7500 rpm for 40 min, and then 7000 rpm for 20 min and redispersion in ethanol. The final concentration of Au NS was estimated to 0.5 nM and [Au^0] = 0.696 mM assuming that all Au seeds were converted to NS (tip-to-tip length, LNS = 70.8 ± 13 nm).

2.4.4. Synthesis of NS@ZIF-67 Core-Shells

3 mL of Au NS (0.5 nM) in ethanol were submitted to two additional centrifugations (7000 rpm for 20 min) washes with water before being redispersed in 3 mL of a 0.5 mM CTAB aqueous solution to yield CTAB-capped Au NS. To prevent the NS reshaping, 100 µL of a 1 mM $AgNO_3$ solution were also added to the mixture. For the NS@ZIF-67 synthesis, 3 mL of a 1.32 M mIm aqueous solution were placed in a vial under stirring at 500 rpm. 3 mL of a $Co(NO_3)_2$ aqueous solution (24 mM) were then injected into the solution. Five seconds later, the 3 mL of the CTAB-capped NS were added, and the mixture was kept under stirring for 5 more minutes and, subsequently, incubated at room temperature for 3 hours. After this, the particles were washed with methanol for 2 times (5000 rpm for 5 min) and redispersed in 3 mL of methanol ([NS@ZIF-67] = 0.5 nM).

2.4.5. Synthesis of NS@ZIF-67@ZIF-8 and Generation of the Yolk-Shells

NS@ZIF-67@ZIF-8 particles were prepared as follows. 3 mL of NS@ZIF-67 in methanol (0.5 nM) were added under stirring (500 rpm) to 3 mL of a 1.32 M mIm aqueous solution. Five minutes later, 3 mL of a 24 mM $Zn(CH_3COO)_2{\cdot}2H_2O$ aqueous solution were added. The mixture was stirred 5 min more and then incubated at room temperature for 3 hours. After the incubation, the color of the solution changed from dark purple to whitish pink, indicating that efficient coating of Au NS@ZIF-67 with ZIF-8. The particles were washed with water for 2 times (5000 rpm, 5 min) and then, redispersed in 3 mL of water (final particle concentration = 0.5 nM). The pH of the solution was previously adjusted to 7.8 by adding a proper amount of 0.1 M NaOH solution. For the preparation of the yolk-shell particles, 3 mL of NS@ZIF-67@ZIF-8 were added to 100 mL water (pH 7.8) and sonicated for 15 min before being left overnight at room temperature. The solution was centrifuged two-times (7000 rpm, 5 min) and redispersed in 3 mL of water (pH 7.8) to a final particle concentration = 0.5 nM.

2.4.6. Synthesis of Pristine ZIF-67 and ZIF-8 Particles

Pristine ZIF-67 and ZIF-8 particles of approximately 500 nm diameter size were prepared in water at room temperature using a 55 ligand-to-metal ion molar ratio (mIm/Co^{2+} for ZIF67, and mIm/Zn^{2+} for ZIF-8). For the ZIF-67 particle synthesis, 3 mL of 1.32 M mIm aqueous solution were placed in a vial under stirring at 500 rpm, then 3 mL of a 24 mM aqueous solution of $Co(NO_3)_2$ were injected into the mixture. Five seconds later, 3 mL of a CTAB solution (0.5 mM) were added to the solution. The mixture was stirred 5 min more and then incubated at room temperature for 3 hours. Afterwards, the particles were washed with methanol for 2 times (5000 rpm, 10 min) and finally redispersed in 3 mL of methanol. For the ZIF-8 particles synthesis, 3 mL of 1.32 M mIm aqueous solution were placed in a vial under stirring at 500 rpm, then 3 mL of a 24 mM aqueous solution of $Zn(CH_3COO)_2{\cdot}2H_2O$ were injected into the solution. Five seconds later, 3 mL of a CTAB solution (0.5 mM) were added to the solution. The mixture was stirred 5 min more and then incubated at room temperature for 3 hours. After the incubation period, the particles were washed with water (pH 7.8) 2 times (9000 rpm, 10 min) and finally redispersed in 3 mL of basified water (pH 7.8).

2.4.7. Theoretical calculations

Simulations were performed with the BEM [41] using the metallic nanoparticles BEM (MNPBEM) toolbox [42]. Gold dielectric constant is from Johnson and Christy [43]. For the simulation we considered the MOFs as perfect dielectrics, n = 2.039 and n = 2.5 for ZIF-8 and ZIF-67 respectively [34, 44]. Volume and cross sectional area of the probe molecules were calculated with DFT at the B3LYP 6-311G (d,p) the level of theory using Gaussian 16.

2.4.8. Instrumentation

UV–Vis spectroscopy (Agilent Technologies, Cary 8454) and TEM JEOL JEM 1010 operating at an acceleration voltage of 100 kV were applied to characterize the optical response and size of the NPs. Elemental mapping analysis were carried out with TEM FEG JEOL 2010F operating at an acceleration voltage of 200 kV. The samples were prepared by drying suspensions on carbon-Formvar-coated 200-mesh copper grids. Zeta potential analysis were carried out with Malvern Zetasizer Nano ZS. N_2 sorption at 77 K was undertaken in

Micromeritics 3Flex instrument. Prior to the measurement, the samples were outgassed at room temperature for 12 h under a pressure of 0.1 Pa. The BET processing was carried out in the relative pressure range of 0.05–0.25. XRD analysis was carried out with Siemens D5000. SERS experiments were conducted using a Renishaw InVia Reflex confocal microscope equipped with a high-resolution grating consisting of 1200 grooves/cm for NIR wavelengths (785 nm), additional band-pass filter optics, and a 2D-CCD camera. Samples were prepared by adding 10 µL of probe of one (or more) analyte at 10^{-4} M to 1 mL of buffered (pH 7.8) colloidal suspensions to reach a final concentration of 10^{-6} M for each of the analytes added. Total gold concentration for all the sample was set to Au_{final}: 0.18 mM.

2.5. References

1. Ghosh Chaudhuri, R. and S. Paria, *Core/shell nanoparticles: classes, properties, synthesis mechanisms, characterization, and applications.* Chemical reviews, 2012. **112**(4): p. 2373-2433.
2. Liz-Marzán, L.M., M. Giersig, and P. Mulvaney, *Synthesis of nanosized gold− silica core− shell particles.* Langmuir, 1996. **12**(18): p. 4329-4335.
3. Sanles-Sobrido, M., et al., *Design of SERS-encoded, submicron, hollow particles through confined growth of encapsulated metal nanoparticles.* Journal of the American Chemical Society, 2009. **131**(7): p. 2699-2705.
4. Pastoriza-Santos, I., et al., *Plasmonic polymer nanocomposites.* Nature Reviews Materials, 2018. **3**(10): p. 375-391.
5. Blanco-Formoso, M., et al., *Boosting the analytical properties of gold nanostars by single particle confinement into yolk porous silica shells.* Nanoscale, 2019. **11**(45): p. 21872-21879.
6. Álvarez-Puebla, R.A., et al., *Au@ pNIPAM colloids as molecular traps for surface-enhanced, spectroscopic, ultra-sensitive analysis.* Angewandte Chemie, 2009. **121**(1): p. 144-149.
7. Bardhan, R., et al., *Theranostic nanoshells: from probe design to imaging and treatment of cancer.* Accounts of chemical research, 2011. **44**(10): p. 936-946.
8. Sousa-Castillo, A., et al., *Remote Activation of Hollow Nanoreactors for Heterogeneous Photocatalysis in Biorelevant Media.* Nano Letters, 2020. **20**(10): p. 7068-7076.
9. Furukawa, H., et al., *The chemistry and applications of metal-organic frameworks.* Science, 2013. **341**(6149): p. 1230444.
10. Li, P., et al., *Bottom-up construction of a superstructure in a porous uranium-organic crystal.* Science, 2017. **356**(6338): p. 624-627.
11. Stock, N. and S. Biswas, *Synthesis of metal-organic frameworks (MOFs): routes to various MOF topologies, morphologies, and composites.* Chemical reviews, 2012. **112**(2): p. 933-969.
12. Nguyen, L.B.T., et al., *Inducing ring complexation for efficient capture and detection of small gaseous molecules using SERS for environmental surveillance.* Angewandte Chemie, 2022. **134**(33): p. e202207447.
13. Liu, J., et al., *Applications of metal–organic frameworks in heterogeneous supramolecular catalysis.* Chemical Society Reviews, 2014. **43**(16): p. 6011-6061.
14. Carrillo-Carrión, C., et al., *Aqueous stable gold nanostar/ZIF-8 nanocomposites for light-triggered release of active cargo inside living cells.* Angewandte Chemie, 2019. **131**(21): p. 7152-7156.
15. Furukawa, H., et al., *Ultrahigh porosity in metal-organic frameworks.* Science, 2010. **329**(5990): p. 424-428.
16. He, L., et al., *Core–shell noble-metal@ metal-organic-framework nanoparticles with highly selective sensing property.* Angewandte Chemie International Edition, 2013. **52**(13): p. 3741-3745.
17. Wiktor, C., et al., *Transmission electron microscopy on metal–organic frameworks–a review.* Journal of Materials Chemistry A, 2017. **5**(29): p. 14969-14989.
18. Barbosa, S., et al., *Tuning size and sensing properties in colloidal gold nanostars.* Langmuir, 2010. **26**(18): p. 14943-14950.
19. Becerril-Castro, I.B., et al., *Gold Nanostars: Synthesis, Optical and SERS Analytical Properties.* Analysis & Sensing, 2022. **2**(3): p. e202200005.
20. Yang, J., et al., *Hollow Zn/Co ZIF particles derived from core–shell ZIF-67@ ZIF-8 as selective catalyst for the semi-hydrogenation of acetylene.* Angewandte Chemie, 2015. **127**(37): p. 11039-11043.
21. Liu, X.Y., et al., *Using a Multi-Shelled Hollow Metal–Organic Framework as a Host to Switch the Guest-to-Host and Guest-to-Guest Interactions.* Angewandte Chemie, 2018. **130**(8): p. 2132-2136.
22. Saliba, D., et al., *Crystal growth of ZIF-8, ZIF-67, and their mixed-metal derivatives.* Journal of the American Chemical Society, 2018. **140**(5): p. 1812-1823.
23. Park, K.S., et al., *Exceptional chemical and thermal stability of zeolitic imidazolate frameworks.* Proceedings of the National Academy of Sciences, 2006. **103**(27): p. 10186-10191.
24. Banerjee, R., et al., *High-throughput synthesis of zeolitic imidazolate frameworks and application to CO2 capture.* Science, 2008. **319**(5865): p. 939-943.
25. !!! INVALID CITATION !!! {}.
26. Zou, D., D. Liu, and J. Zhang, *From Zeolitic Imidazolate Framework-8 to Metal-Organic Frameworks (MOF s): Representative Substance for the General Study of Pioneering MOF Applications.* Energy & Environmental Materials, 2018. **1**(4): p. 209-220.
27. Zhao, M., et al., *Selective epitaxial growth of oriented hierarchical metal–organic framework heterostructures.* Journal of the American Chemical Society, 2020. **142**(19): p. 8953-8961.
28. Kumari, G., et al., *Temperature induced structural transformations and gas adsorption in the zeolitic imidazolate framework ZIF-8: A Raman study.* The Journal of Physical Chemistry A, 2013. **117**(43): p. 11006-11012.
29. Giannini, V., et al., *Long-range surface polaritons in ultra-thin films of silicon.* Optics express, 2008. **16**(24): p. 19674-19685.
30. Schlücker, S., *Surface-Enhanced raman spectroscopy: Concepts and chemical applications.* Angewandte Chemie International Edition, 2014. **53**(19): p. 4756-4795.

31. Alvarez-Puebla, R., D. Dos Santos Jr, and R. Aroca, *Surface-enhanced Raman scattering for ultrasensitive chemical analysis of 1 and 2-naphthalenethiols.* Analyst, 2004. **129**(12): p. 1251-1256.
32. Xie, W., et al., *Synthesis of bifunctional Au/Pt/Au core/shell nanoraspberries for in situ SERS monitoring of platinum-catalyzed reactions.* Journal of the American Chemical Society, 2011. **133**(48): p. 19302-19305.
33. Koh, C.S.L., et al., *Plasmonic nanoparticle-metal–organic framework (NP–MOF) nanohybrid platforms for emerging plasmonic applications.* ACS Materials Letters, 2021. **3**(5): p. 557-573.
34. Qiao, X., et al., *Selective surface enhanced Raman scattering for quantitative detection of lung cancer biomarkers in superparticle@ MOF structure.* Advanced materials, 2018. **30**(5): p. 1702275.
35. Pazos-Perez, N., L. Guerrini, and R.A. Alvarez-Puebla, *Fabrication of hybrid silver microstructures from vermiculite templates as SERS substrates.* Nanomaterials, 2020. **10**(3): p. 481.
36. Tripathi, A., et al., *Kinetics and reaction mechanisms of thiophenol adsorption on gold studied by surface-enhanced Raman spectroscopy.* The Journal of Physical Chemistry C, 2013. **117**(44): p. 22834-22842.
37. Álvarez-Puebla, R.n.A., *Effects of the Excitation Wavelength on the SERS Spectrum.* The journal of physical chemistry letters, 2012. **3**(7): p. 857-866.
38. Huang, Y.-F., et al., *When the signal is not from the original molecule to be detected: chemical transformation of para-aminothiophenol on Ag during the SERS measurement.* Journal of the American Chemical Society, 2010. **132**(27): p. 9244-9246.
39. Enustun, B. and J. Turkevich, *Coagulation of colloidal gold.* Journal of the American chemical society, 1963. **85**(21): p. 3317-3328.
40. Turkevich, J., P.C. Stevenson, and J. Hillier, *A study of the nucleation and growth processes in the synthesis of colloidal gold.* Discussions of the Faraday Society, 1951. **11**: p. 55-75.
41. De Abajo, F.G. and A. Howie, *Retarded field calculation of electron energy loss in inhomogeneous dielectrics.* Physical Review B, 2002. **65**(11): p. 115418.
42. Hohenester, U. and A. Trügler, *MNPBEM–A Matlab toolbox for the simulation of plasmonic nanoparticles.* Computer Physics Communications, 2012. **183**(2): p. 370-381.
43. Johnson, P.B. and R.-W. Christy, *Optical constants of the noble metals.* Physical review B, 1972. **6**(12): p. 4370.
44. Krishtab, M., et al., *Vapor-deposited zeolitic imidazolate frameworks as gap-filling ultra-low-k dielectrics.* Nature Communications, 2019. **10**(1): p. 3729.

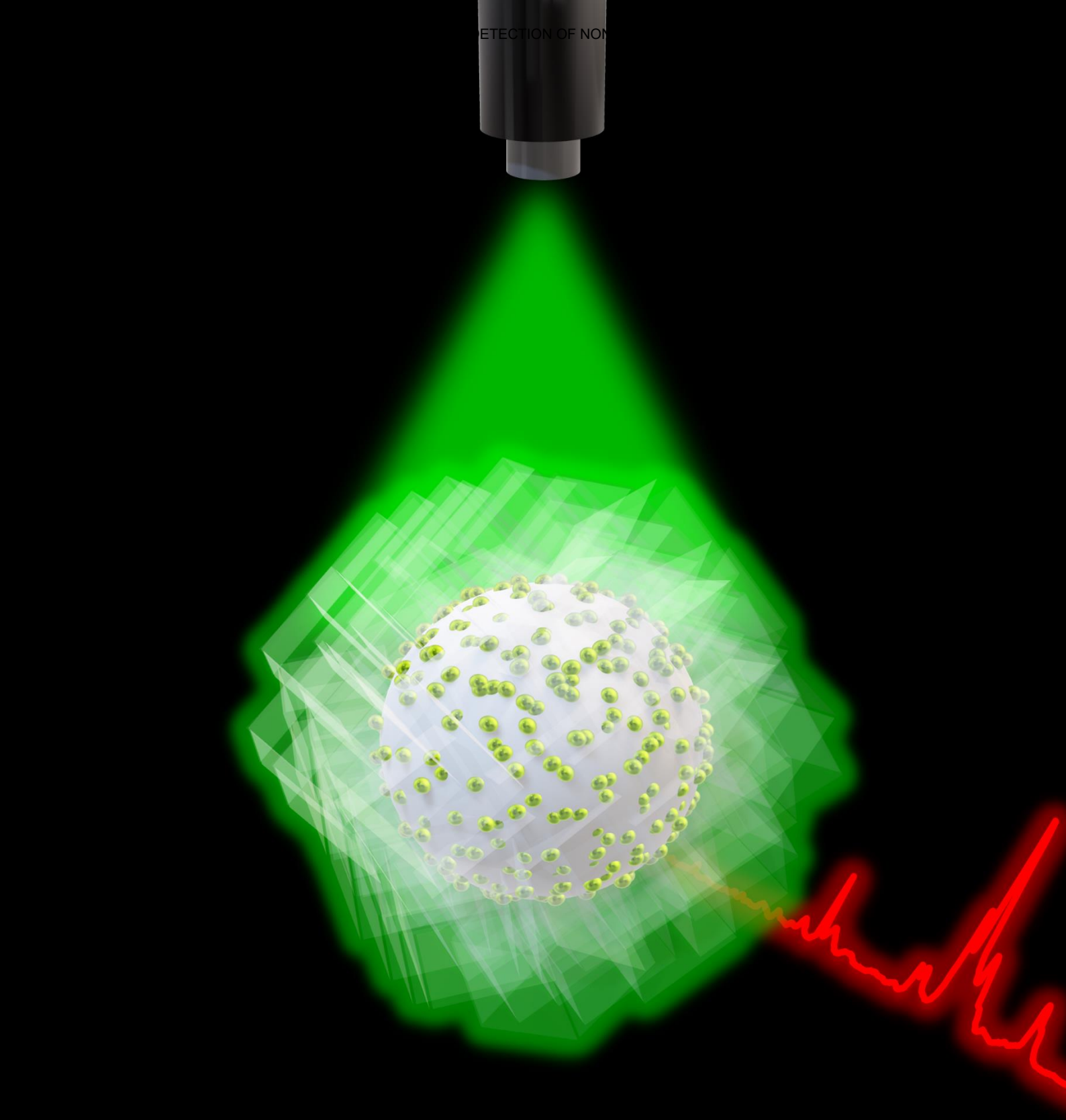

CHAPTER THREE

Optical Quantification of Metal Ions using Plasmonic Microbeads Coated with Metal-Organic Frameworks and Ion-Selective Dyes

Herein, we designed and synthesized a hybrid material comprising PS sub-microbeads coated with Ag nanospheres. This material provides a dense collection of electromagnetic hotspots upon illumination with visible light. The subsequent coating with a MOF, and the adsorption of bathocuproine (BC) on it yields an optical sensor for SERS that can detect specifically Cu(II) in a variety of aqueous samples at the ultra-trace level. Detection limits with this method are superior to those of inducted coupled plasma or atomic absorption and comparable with those obtained with inducted coupled plasma coupled with a mass detector.

3.1. Introduction

SERS is a powerful ultrasensitive technique based in the close contact of the target analyte with a plasmonic particle [1-3]. However, as a molecular spectroscopy, SERS is unable to detect atomic species [4]. These species, and specially metallic ions, represent a good portion of water and soil pollution [5] and also have key interest in the study of biological processes [6] or even the diagnosis of certain diseases [7]. Thus, to apply this sensitive analytical technique to the detection of metals (and other atomic ions) usually plasmonic surfaces are functionalized with molecules (i.e., chemosensors) that react with these species [4]. In such a case, the atomic analyte is indirectly detected through the changes that it induces on the molecular [8] or electronic [9] structure or in the orientation of the chemosensor [10]. Notably, although the classic analytical literature describing to the use of organic reagents specific for each metal ion, and sometimes to each oxidation state for the same ion, is extensive [11-14], the use of such molecules in SERS is very restricted because of the necessity of the chemosensor to be explicitly attached to the plasmonic surface. In such conditions, the most common chemosensors for atomic ion analysis relies in the use of thiolated small aromatic molecules that are functionalized metal reactive moieties such as carboxylic, amino or alcohol groups that can react with the target metals [15]. This strategy, however, shows little specificity and, while can be successfully applied to simple analytical problems, does not work for complex fluids such as those of biological or natural origin.

MOFs are porous materials with homogeneous pores formed by the coordination of organic linkers with metal ions [16, 17]. During the last two decades, MOFs have demonstrated utility in a diversity of applications ranging from catalysis, separation, drug delivery or analytical chemistry, either alone or in the form of composites with another materials [18-20]. In particular, plasmonic NPs coated with MOFs had been successfully applied to the analysis of small molecules [21, 22], drug delivery [23, 24], and pollutant separation [25-28]. Commonly, these materials are prepared by coating single particles with a thin shell of MOF or by dispersing multiple but isolated particles within a MOF matrix. Either way, due to the lack of interaction between particles to form electromagnetic hotspots [1]. Thus, to ensure the electromagnetic field enough to produce a good SERS signal, these composites usually employ single particle hotspots such NS [24, 29], a well-known plasmonic particle capable of localizing

strong electromagnetic field at their tips [30]. These composite MOF-NS materials are very useful upon near infrared illumination, but their LSPR below 700 nm is modest, with the subsequent limited optical enhancement [30].

Herein, we designed and synthesized a hybrid material comprising PS sub-microbeads coated with Ag nanospheres. This material provides a dense collection of electromagnetic hotspots upon illumination with visible light [9]. Subsequently, the plasmonic beads were coated with MOF providing a plasmonic material with the same properties, or even better, as common NS coated with MOFs, but in the visible. Finally, to probe the efficiency of this composite for ultra-trace analysis of ions, and exploiting the affinity of MOFs for nonpolar organic molecules, a selective dye for copper, BC [31], was adsorbed in the composite material. The sensing platform was the used for the analysis of copper ions in aqueous samples of different natural origin.

3.2. Results and Discussion

The schematic illustration of the preparation steps of the PS@Ag@ZIF-8 composites is given in Figure 3.1A. Accordingly, PS beads (496 ± 16 nm diameter) were coated with a layer of the positively-charged polymer, PAH. Subsequently, the material was exposed to an excess of spherical negatively-charged Ag NPs of 51 ± 6 nm size (Figure 3.1A) to promote their electrostatic retention onto the bead surfaces.

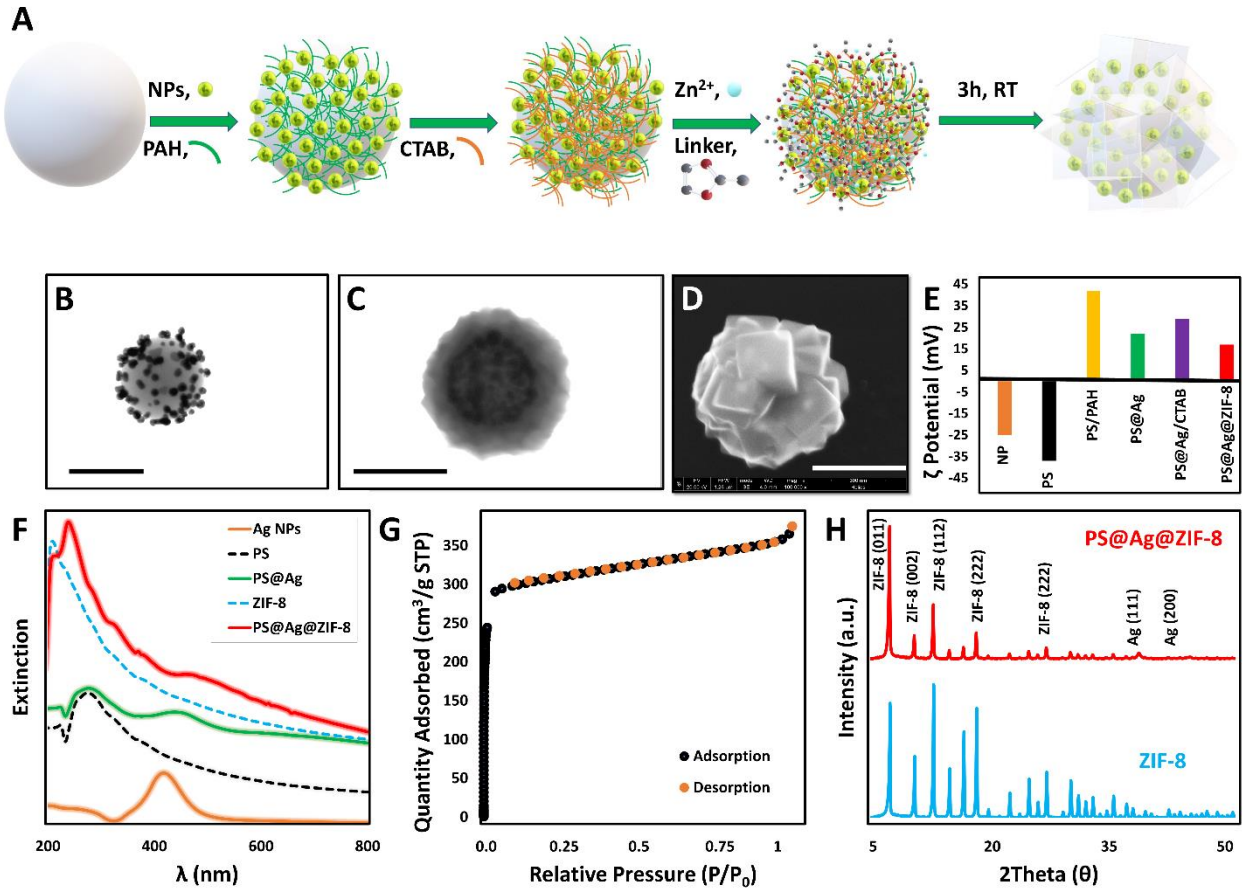

Figure 3.1. ***(A)*** *Schematic illustration of preparation stages of PS@Ag@ZIF-8 SERS substrates.* ***(B)*** *Representative TEM images of PS@Ag beads.* ***(C-D)*** *Representative TEM and SEM images of the composites, respectively. Scale bars, 500 nm.* ***(E)*** *Zeta potential at the different fabrication steps of the composite. The final particles have nearly +17 mV.* ***(F)*** *Extinction spectra of Ag NPs, PS beads, PS@Ag beads, pristine ZIF-8, and PS@Ag@ZIF-8 suspensions.* ***(G)*** *N_2 adsorption-desorption isotherm of PS@Ag@ZIF-8 composite.* ***(H)*** *XRD patterns of PS@Ag@ZIF-8 and pristine ZIF-8 crystals.*

Such colloidally stable 3D collections of closely spaced NPs onto the PS core yield highly intense SERS signals [9, 10]. The resulting PS@Ag beads (Figure 3.1B and 3.2B) were then redispersed into a CTAB aqueous solution below the critical micelle concentration (CMC) before the direct growth of the outer ZIF-8 shell. Here, CTAB molecules have two important effects. First, the molecules act as a bridge between ZIF-8 precursors and PS@Ag beads by adsorbing plasmonic Ag NPs located on the PS surface. In this way, it was ensured that the composite material is completely covered with ZIF-8 crystals. Second, CTAB concentrations added below CMC help to obtain ZIF-8 crystals in desired sizes and monodispersity. However, the natural crystal morphology of ZIF-8 changes from TRD to cubic morphology, as the hydrophobic tail of CTAB more energetically and selectively suppresses the [100] faces of growing crystals [32]. This change can be easily observed with the representative SEM image in Figure 3.1D.

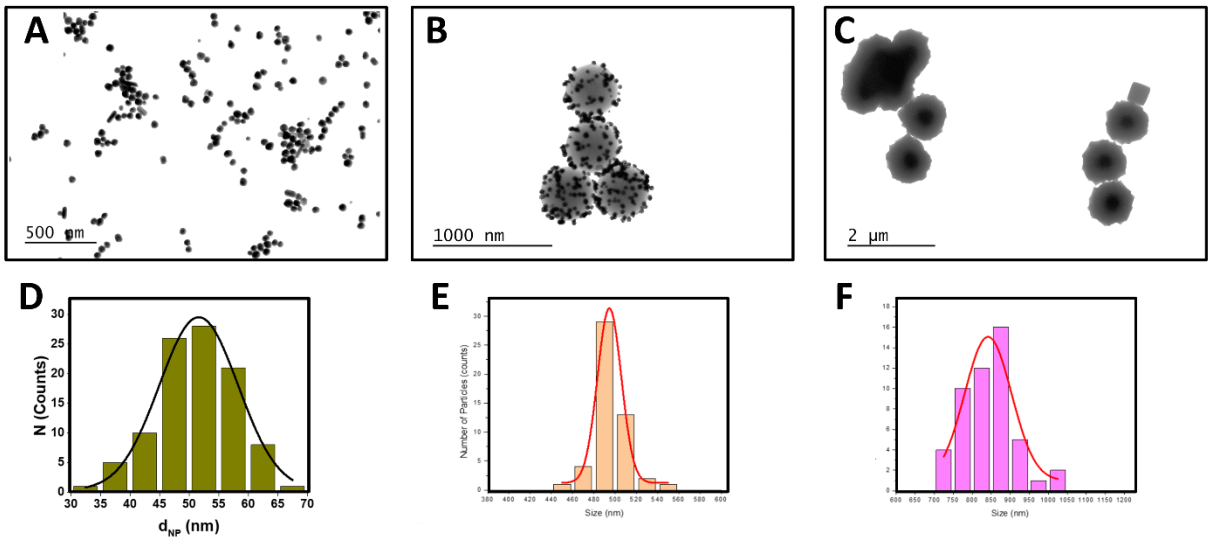

Figure 3.2. ***(A)*** *representative TEM image of Ag NPs,* ***(B)*** *PS@Ag Beads and* ***(C)*** *PS@Ag@ZIF-8 composites.* ***(D-F)*** *Histograms of Ag NPS, PS beads, and PS@Ag@ZIF-8 composite diameters, respectively.*

For the preparation of the composites, CTAB-modified PS@Ag beads were subsequently combined, under stirring, with aqueous solutions mIm and zinc acetate to yield PS@Ag@ZIF-8 particles of 847 ± 69 nm size (Figure 3.1C, D and 3.2C). Zeta potential measurements reveal that ZIF-8-coated PS@Ag beads have a highly positive surface charge,

however, there is a decrease in surface charge due to the linker, mIm, when compared to bare PS@Ag (Figure 3.1E). UV-Vis spectroscopy was also used to monitor the optical evolution of the composites during the different fabrication steps. As shown in Figure 3.1F, the accumulation of Ag NPs onto the PS surface causes a red-shift of the LSPR of the individual NPs (from ca. 418 to 446 nm) and the appearance of a new broad shoulder at longer wavelengths which is associated with the plasmon coupling of surface-bound and closely-spaced Ag NPs. Subsequent coating with ZIF-8 determines a dampening of the plasmonic contribution and its further red-shift, which is also consistent with the NP entrapment within the ZIF-8 shell. N_2 physisorption and BET analysis of the composites show the typical reversible type I isotherm (Figure 3.1G) as previously observed for pure ZIF-8 crystals. Here, the amount of adsorbed N_2 rapidly increases at low pressures, indicating the existence of micropores [33, 34]. Similarly, the obtained surface area (S_{BET} ~ 1000 m^2/g) also falls within the common range reported for pristine ZIF-8 particles (ca. 800 – 1400 m^2/g) (Figure 3.3) [34]. XRD patterns of PS@Ag@ZIF-8 feature both low angle diffractions from ZIF-8 (2θ = 7.4°, 10.41°, 12.75°) and the different diffraction from Ag (2θ = 38.4°), confirming the crystallinity of the composites (Figure 3.1H).

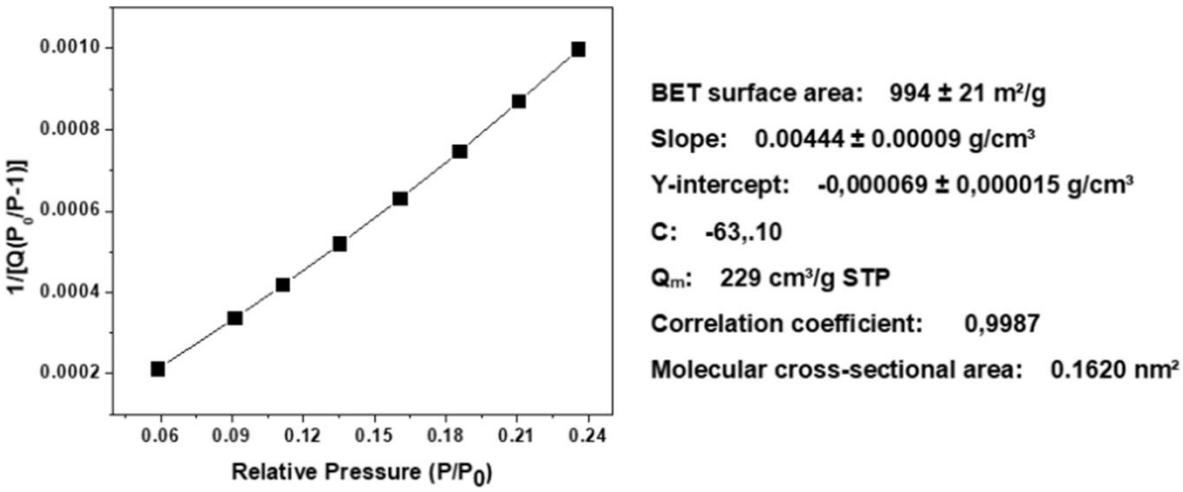

Figure 3.3. BET surface area plot of PS@Ag@ZIF-8 composites

Figure 3.4A shows the near field calculations at 532 nm for a model comprising Ag NPs on a PS bead before and after coating with ZIF-8. As expected, the higher enhancements are located at the gaps between the NPs in both samples. Overall, PS@Ag@ZIF-8 shows a higher

enhancement than the PS@Ag. This increase is ascribed to the deposition of ZIF-8 on the plasmonic structure, which increases the local refractive index and red-shifts the LSPR, thus, producing a better overlap between the excitation light and the LSPR of the material [35]. To test the SERS enhancing properties of PS@Ag and PS@Ag@ZIF-8 in aqueous suspension we used a well-known BT as molecular probe at different concentrations (Figures 3.4B-D).

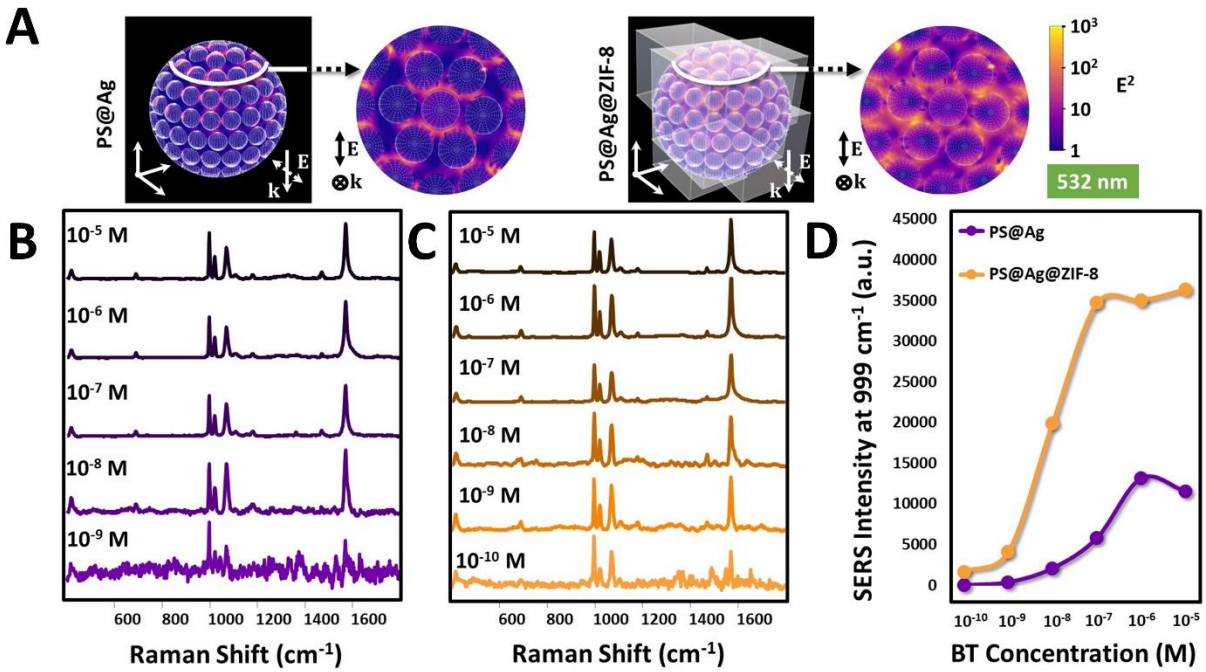

Figure 3.4. (A) Near field calculations (532 nm) of a model PS@Ag beads before and after coating with ZIF-8. Insets show a top view of the sample within the white border. (B-C) SERS spectra of different concentrations of BT on PS@Ag beads and PS@Ag@ZIF-8 composites. (D) Comparison of absolute SERS intensities at 999 cm^{-1} band for BT molecules on PS@Ag and PS@Ag@ZIF-8.

In a typical experiment, SERS measurements were carried out on equimolar particle suspensions using a 532 nm laser and adopting a macro set-up configuration to obtain quantitatively reliable SERS spectra resulting from the averaged contribution of many beads within the illuminated volume. As can be observed, PS@Ag@ZIF-8 yields detection limits down to 10^{-10} M, one order of magnitude lower than bare PS@Ag beads (Figure 3.4B and C). The absolute intensity of the narrow band at 999 cm^{-1} (ring breathing mode) [36] is plotted in Figure 3.4D as a function of BT concentration. Moreover, the absolute intensity at the plateau ([BT] > 10^{-7} M) for PS@Ag@ZIF-8 is ca. 4-fold larger than for bare PS@Ag beads. These results are due

to two factors; the better resonance laser-LSPR, in full agreement with the theoretical calculations (Figure 3.4A), and the optical accumulation effect derived by the improved affinity of ZIF-8 for the organic probe. This later increase the local concentration of the analyte close to the plasmonic surface with the subsequent increase in the SERS intensity [37].

BC has been extensively used as a highly specific ligand for Cu(I) and Cu(II) with no interferences from other cations being reported [31, 38, 39]. BC coordinates, through its nitrogen groups, with copper ions to form the BC_2-Cu complex (Figure 3.5A). This reaction induces a change in the electronic spectra generating a new band at 483 nm (Figure 3.5B-C). The characterization of BC and BC_2-Cu with Raman, exciting the samples with 785 nm laser, shows a clear change in their spectral profile (Figure 3.5D). In summary, a drop in intensity of the band at 1367 cm^{-1} (NC stretching) of BC, which is mirrored by an increase of the bands at 1425 cm^{-1} (CCH bending) and 1563 cm^{-1} (C=C stretching) for BC_2-Cu. These changes are specific for copper ions and does not appear when other metals are present in solution (Figure 3.5E).

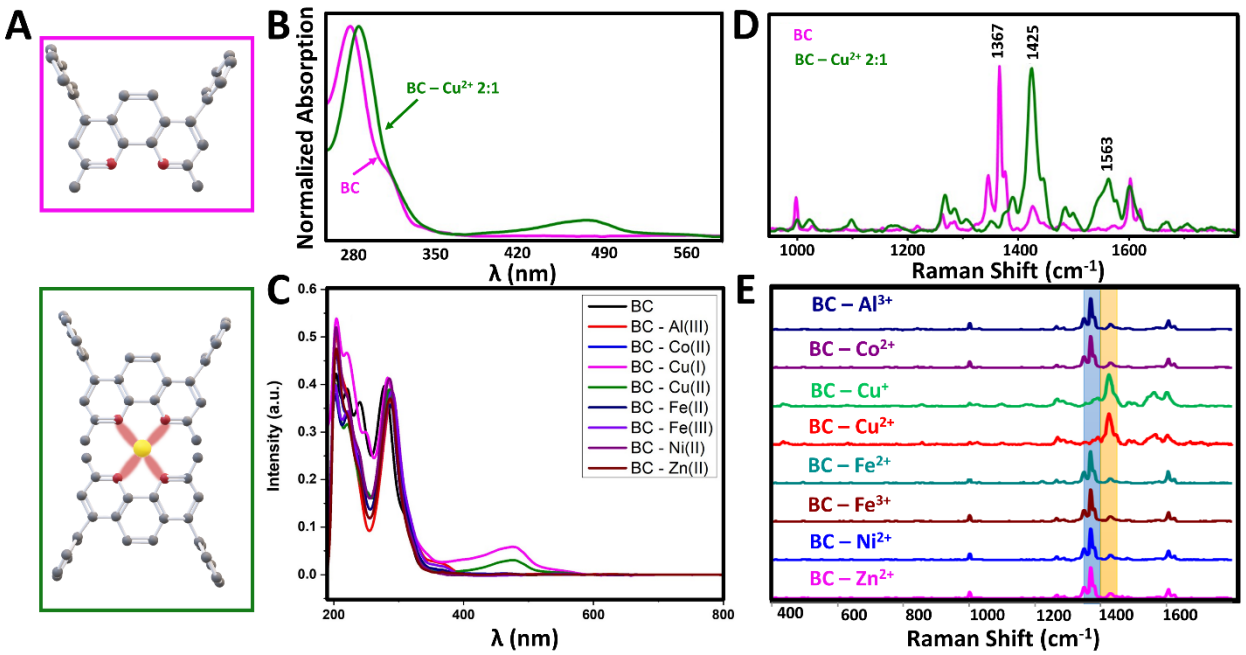

Figure 3.5. (A) *Molecular structures of BC (above), and BC_2-Cu^{2+} complex (below). Colour code: C: grey, N: red, and Cu: yellow. Reddish stripes indicate the coordination bonds between N and Cu atoms. Hydrogen atoms were omitted for clarity.* ***(B)*** *Absorption spectra of BC in ethanol (10 µM) before and after the addition of Cu^{2+} (ligand/metal molar ratio = 2:1).* ***(C)*** *Absorption spectra of BC ethanolic solutions (10 µM) upon addition of different metal ions (final concentration = 5 µM).* ***(D)*** *Raman spectra of the corresponding solids (excitation wavelength = 785 nm).* ***(E)*** *Raman spectra of the solids were*

obtained by mixing ethanolic solutions of BC and metal ions at a 2:1 molar ratio. Upon solvent evaporation, the remaining powder was collected and interrogated by Raman. Excitation wavelength = 785 nm.

Notably, the excitation of the same samples with a green laser (532 nm) yields an intense fluorescence for BC_2-Cu that saturates the detector, signal of the resonance between the green laser and the complex. To prepare the optical sensor, BC was loaded onto the PS@Ag@ZIF-8 by immersing the composite in an ethanolic solution of the dye at the desired concentration for 12 h. Notably, calculated dimensions for BC are 10.8 x 9.3 x 4.3 Å (Figure 3.6A). However, calculated dimensions for ZIF-8 pores are 0.8 and 3.4 Å (Figure 3.6B) [40-42], bellow 1.5 Å, as calculated from the N_2 sorption isotherm (Figure 3.6C). Thus, a priori, the penetration of the dye is sterically restricted. However, unlike other porous structures such as silica, carbon or clays, ZIF-8 exhibits dynamic pore properties [27] due to the swing motion of the mIm ring [43], which allows the MOF to adsorb large molecules specially when in alcohol solutions and for nonpolar adsorbents [24, 44]. Thus, to ensure the appropriate retention of the dye, the supernatants after centrifugation were studied by UV-Vis spectroscopy showing no evidence of the presence of dissolved BC. Conversely, the sediments (i.e., PS@Ag@ZIF-8 loaded samples) were studied with SERS. Figure 3.6D shows the SERS spectra of PS@Ag@ZIF-8 upload with different concentrations of BC. The characteristic dye signal can be clearly recognized until concentrations of 10^{-7} M in initial BC. To test the stability of the retained BC, the sediments were redispersed in water and centrifuged several times. After each centrifugation cycle the supernatants were monitored by UV-Vis and sediments by SERS. Neither BC molecules were detected in the supernatants nor a decrease in SERS intensity has been observed in the sediments (Figure 3.6E), demonstrating the stability in water of the sensing element. This behaviour contrast with that of the PS@Ag, which under the same conditions show no signal of BC retention (Figure 3.6F).

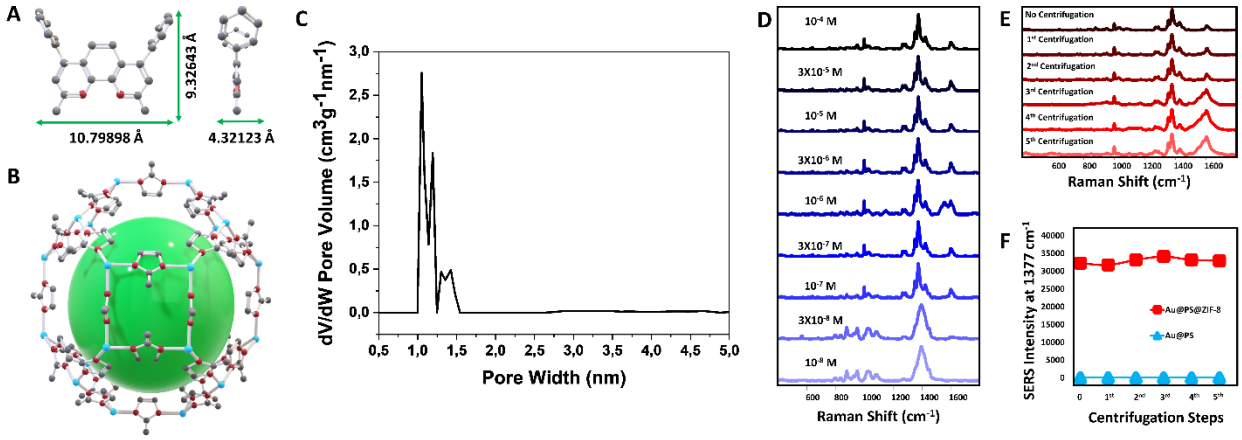

Figure 3.6. ***(A)*** *Molecular size of a BC according to DFT at B3LYP 6-311G(d, p) the level of theory.* ***(B)*** *Schematic representation of the structure of ZIF-8 crystal. The green sphere represents the pore cavity with nearly 12 Å. Four-membered rings (4MRs) and six-membered rings (6MRs) in the structure have 0.8 and 3.4 Å sizes, respectively. The 6MR can expand to accommodate larger molecules. Colour code: C: grey, N: red, and Zn: cyan. Hydrogen was omitted for clarity.* ***(C)*** *Pore size distribution of PS@Ag@ZIF-8 composites.* ***(D)*** *SERS spectra of different concentrations of BC adsorbed on PS@Ag@ZIF-8.* ***(E)*** *SERS spectrum of the sediments obtained after several washing cycles.* ***(F)*** *Comparison between the SERS intensities of BC (band at 1377 cm^{-1}) on PS@Ag@ZIF-8 and PS@Ag after the same washing samples.*

To study the performance of the sensor in the detection of metallic ions, the composite loaded with BC (PS@Ag@ZIF-8-BC) was exposed to several aqueous samples spiked with Cu(II). The modification of the SERS fingerprint of BC embedded into the composites upon exposure to a Cu(II) solution is qualitatively analogous to what was observed for the Raman measurements. Furthermore, when PS@Ag@ZIF-8-BC was combined with solutions of Ca^{2+} (1 mM), Cd^{2+} (10 µM), Fe^{3+} (20 µM), Zn^{2+} (40 µM) and Pb^{2+} (10 µM), no distinguishable spectral alterations were detected (Figure 3.7).

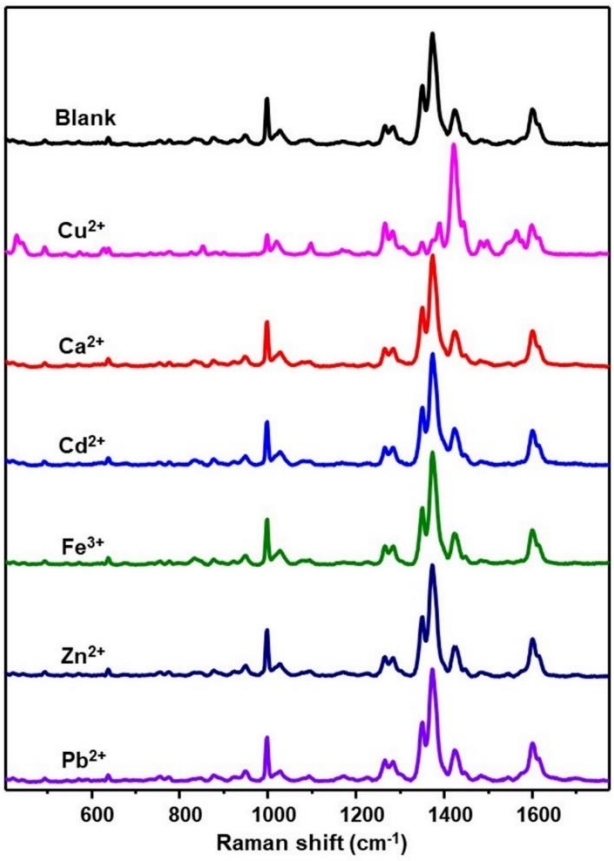

Figure 3.7. SERS spectra of BC 1 µM on PS@Ag@ZIF-8 (blank) and in the presence of Cu^{2+} (2 µM), Ca^{2+} (1 mM), Cd^{2+} (10 µM), Fe^{3+} (20 µM), Zn^{2+} (40 µM) and Pb^{2+} (10 µM). Excitation wavelength = 532 nm.

It is worth noting that the characteristic vibrational pattern of the BC_2-Cu^{2+} complex is obtained immediately after the dispersion of the hybrid particles in the sample, indicating the extremely fast diffusion of Cu^{2+} across the ZIF-8 shell to reach the proximity of the inner Ag NP surfaces (i.e., no incubation is required). The Cu^{2+} concentration response of PS@Ag@ZIF-8-BC dispersed in PBS (pH 7.4) is shown in Figure 3.8A.

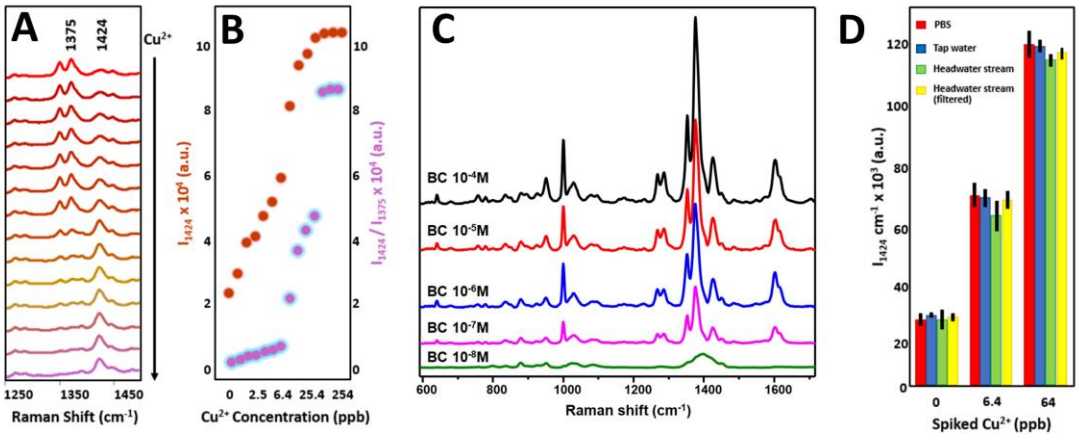

Figure 3.8. *(A) SERS spectra of BC (1 µM) on PS@Ag@ZIF-8 upon immersion into Cu(II) solutions in PBS buffer (pH 7.4) at different copper concentrations (from top to bottom: 0, 0.65, 1.3, 2.5, 3.8, 5.1, 6.4, 12.7, 25.4, 38.1, 50.8, 63.5, 127, and 254 ppb). (B) SERS intensity (I_{1424}) and intensities ratio (I_{1424}/I_{1375}) vs. Cu^{2+} concentration in PBS (N = 3). (C) SERS spectra of different concentrations of BC on PS@Ag@ZIF-8 in PBS buffer (pH 7.4) (excitation wavelength = 532 nm). (D) SERS intensity I_{1424} in pristine PBS, tap water and headwater stream (unfiltered and filtered) and in the same matrices spiked with Cu(II) at a final concentration of 6.4 and 64 ppb (N = 3).*

The data highlight the progressive reshaping of the SERS spectrum to which extent can be quantitatively correlated with the metal ion content. For instance, the bands at 1424 and 1375 cm^{-1}, selected as markers of the Cu^{2+} chelation vs free BC, respectively, undergo an intensity increase (1424 cm^{-1}) and decrease (1375 cm^{-1}) with the increase in copper concentration. Among these two parameters, the intensity of the 1424 cm^{-1} band vs metal ion concentration provides the best outcome, exhibiting an excellent linear response over two orders of magnitude (from ca. 250 to 2.5 ppb, which corresponds to ca. 4 µM to 40 nM; r^2 = 0.99) and a limit of detection of ca. 0.6 ppb (10 nM, corresponding to an I_{1424} value larger than the blank sample plus 2 times standard deviation). This level is competitive with techniques such as ICP-MS (0.1 ppb) and far superior to other methods such as ICP (0.3 ppm) or FAAS (0.5 ppm) [45]. On the other hand, the intensity ratio I_{1424}/I_{1375} (Figure 3.8B) displays a linear response in a narrower Cu^{2+} concentration range (ca. 4 µM-100 nM, r^2 = 0.970) and a limit of detection of ca. 1.2 ppb (20 nM). It must be stressed that the BC content on PS@Ag@ZIF-8 has been approximately optimized to yield intense SERS signals with a high signal-to-noise ratio, which improves the accuracy and robustness of the SERS response while maintaining the ligand

concentration sufficiently low to meet the specific requirements of sensitivity and dynamic linear response for Cu^{2+} detection (Figure 3.8C). Besides, to demonstrate that the composites are fully functional in different environments, we used tap water and freshwater samples, the latter collected at a headwater stream site located in Campus Lagoas Marcosende, Universidade de Vigo (Spain). Figure 3.8D shows the SERS intensities of the 1424 cm^{-1} BC marker band in pristine waters as well as samples spiked with $CuCl_2$ solution to a final concentration of 6.4 or 64 ppb. Remarkably, no significant changes were detected when compared with the response observed in Cu^{2+} buffer solutions.

3.3. Conclusions

In conclusion, we have demonstrated that a nonfunctionalized ion-selective dye such as BC can be absorbed onto a composite material comprising a plasmonic sub-microbead coated with ZIF-8. The resulting optical sensor can detect Cu(II) at the ultra-trace level without further processing by means of SERS. Detection limits with this method are superior to those of inducted coupled plasma or atomic absorption and comparable with those obtained with inducted coupled plasma coupled with a mass detector.

3.4. Experimental Section

3.4.1. Materials

$AgNO_3$ (99%), *L*-ascorbic acid (99%), sodium citrate tribasic dihydrate (≥98%), $MgSO_4$ (≥97%), zinc acetate dihydrate (98%, $Zn(CH_3COO)_2{\cdot}2H_2O$), mIm (99%), PAH (MW = 15000 Da), NaCl (≥99.5%), KCl (≥99%), Na_2HPO_4 (≥99%), NaH_2PO_4 (≥99%,), aluminum nitrate nonahydrate (≥98%, $Al(NO_3)_3{\cdot}9H_2O$), cobalt(II) nitrate hexahydrate (98%, $Co(NO_3)_2{\cdot}6H_2O$), copper(I) iodide (99.9%, CuI), copper(II) chloride dihydrate (≥99%, $CuCl_2{\cdot}2H_2O$), iron(II) chloride (98%, $FeCl_2$), iron(III) chloride hexahydrate (≥99%, $FeCl_3{\cdot}6H_2O$), nickel(II) nitrate hexahydrate (≥98.5%, $Ni(NO_3)2{\cdot}6H_2O$), BT (95%) and ethanol (99.5%) were purchased from Sigma-Aldrich (Germany). BC (98%) was purchased from Fisher Scientific. PS bead solution (ca. 500 nm, AJ50) was purchased from Ikerlat Polymers (Spain). CTAB (≥99%) was purchased from Acros Organics (Germany). All reactants were used without further purification. Milli-Q water (18 MΩ cm−1) was used in all aqueous solutions, and all the glassware was cleaned with aqua regia before the experiments

3.4.2. Synthesis of Ag Nanospheres

Synthesis of Ag colloids was carried out as previously reported [46]. Briefly, 100 mL of H_2O were heated until boiling. Then, an aqueous mixture of 100 µL of ascorbic acid (0.1 M) and 1.364 mL of citric acid (0.1 M) was added under strong magnetic stirring. 1 min later, another aqueous mixture of 298 µL of $AgNO_3$ (0.1 M) and 224 µL of $MgSO_4$ (0.1 M) was added (such mixture was previously incubated for 5 min). The solution was left boiling under stirring for another 30 min and let to cool down at room temperature before being centrifuged once (6500 rpm, 15 min). The pellet was redispersed with Milli-Q water to yield a final Ag^0 concentration of 1.4 mM.

3.4.3. Deposition of Ag NPs on PS Beads (PS@Ag)

PS of ca. 500 nm diameter were initially coated with positively charge PAH. To this end, 10 mg of PAH were added to 10 mL of NaCl aqueous solution (0.5 M) and sonicated for 30 min. Then, 100 µL of PS bead dispersion (100 mg/mL) were added to 9.9 mL of aqueous PAH solution and stirred at 500 rpm for 30 min. The sample was then submitted to three centrifugation-

washing cycles (9000 rpm, 30 min) with Milli-Q water to remove unbound PAH. Finally, the PS@PAH beads were redispersed in 50 mL of Milli-Q water (PS concentration = 0.2 mg/mL). To this sample, 10 mL of the Ag colloids ([Ag^0] = 1.4 mM) were added dropwise under sonication. Immediately after, the mixture was stirred (300 rpm) for another 30 min. Finally, the mixture was submitted to three centrifugation-washing cycles (4500 rpm, 15 min) with Milli-Q water to remove unbound Ag NPs. The resulting PS@Ag beads were redispersed in 10 mL of Milli-Q water (PS@Ag concentration = 1 mg/mL).

3.4.4. Preparation of ZIF-8 Coated PS@Ag Beads (PS@Ag@ZIF-8)

157.9 µL of CTAB aqueous solution (10 mM) were added to 3 mL of PS@Ag suspension (1 mg/mL) and stirred for 30 min for adsorption of CTAB to the plasmonic surface. Then, 3 mL of mIm aqueous solution (1.32 M) were added under stirring (500 rpm) followed, 10 minutes later, by 3 mL of $Zn(CH_3COO)_2$ aqueous solution (24 mM). The mixture was kept under stirring for 5 more minutes and, subsequently, incubated at room temperature for 3 hours. Afterwards, the sedimented PS@Ag@ZIF-8 particles were separated from the whitish supernatant and were submitted to two centrifugation-washing cycles (4500 rpm, 5 min) to remove residual ZIF-8 particles in the supernatant. The PS@Ag@ZIF-8 pellet was finally redispersed in 15 mL of Milli-Q water (PS concentration = 0.2 mg/mL).

3.4.5. Sample Preparation for Raman Analysis

Two aliquots of 500 µL of equimolar ethanolic solutions (2×10^{-3} M) of BC and metal cation solutions were combined. Immediately after, the color changed from transparent to vermilion. The solvent was removed by evaporation at 60-65°C. The residual solids were collected and characterized by Raman spectroscopy.

3.4.6. Sample Preparation for SERS Analysis

500 µL of PS@Ag@ZIF-8 (0.2 mg/mL) were added to 10 mL of ethanolic solutions of BT or BC at the desired concentration. The mixtures were incubated overnight and then submitted to two centrifugation-washing cycles (4500 rpm, 5 min) with Milli-Q water. BC-loaded PS@Ag@ZIF-8 were finally redispersed in 1 mL of Milli-Q water. An identical protocol was applied for PS@Ag particles. For metal ion detection, the 100 µL of BC-loaded PS@Ag@ZIF-8

particles were combined with 1 mL of metal ion solution, at different Cu(II) concentrations, prepared directly in PBS buffer (pH 7.8) or by spiking tap water and freshwater with appropriate aliquots of a $CuCl_2$ solution. Similar protocols were applied for the detection of other metal cations. Filtration of the samples, when applied, was performed using a 0.45 µm pore diameter filter paper.

3.4.7. Theoretical Calculations

Simulations were performed with the BEM [47] using the MNPBEM toolbox [48]. Silver dielectric constant is from Palik's Handbook [49]. For the simulation we considered the MOF as a perfect dielectric, n = 2.039. Volume and cross sectional area of the probe molecules were calculated with DFT at the B3LYP 6-311G(d,p) the level of theory using Gaussian 16.

3.4.8. Instrumentation

UV–Vis spectroscopy (Agilent Technologies, Cary 8454), TEM (JEOL JEM 1010) and FIB-SEM (Helios NanoLab 600) operating at an acceleration voltage of 100 kV were applied to characterize the optical response and size of the particles. The samples were prepared by drying suspensions on carbon-Formvar-coated 200-mesh copper grids. Zeta potential studies were carried out with Malvern Zetasizer Nano ZS. Physisorption studies were carried out with N_2 at 77 K using a Belsorp-max apparatus from MicrotracBEL Corporation (Osaka, Japan). Before being analyzed, the samples were outgassed at room temperature for 12 h under a pressure of 0.1 Pa. The BET processing was carried out in the relative pressure range of 0.05–0.25. XRD analysis was carried out with Siemens D5000. Raman and SERS spectra were collected in backscattering geometry with a Renishaw inVia Reflex system equipped with a 2D-CCD detector, a Leica confocal microscope and two excitation sources: a 532 nm frequency doubled Nd:YAG/Nd:YVO4 diode, and a 785 nm NIR diode laser. The 532 nm laser was focused on the colloidal suspension using a macro lens (10 s exposure, 3 accumulations) with power at the sample of 17.1 mW (100%, PBS, tap water and freshwater samples) and 2.19 mW (10%, urine samples). Normal Raman spectra of BC/metal cation powders were obtained using a 785 nm laser to remove background fluorescence.

3.5. References

1. Langer, J., et al., *Present and future of surface-enhanced Raman scattering.* ACS nano, 2019. **14**(1): p. 28-117.
2. Schlücker, S., *Surface-Enhanced raman spectroscopy: Concepts and chemical applications.* Angewandte Chemie International Edition, 2014. **53**(19): p. 4756-4795.
3. Álvarez-Puebla, R.n.A., *Effects of the Excitation Wavelength on the SERS Spectrum.* The journal of physical chemistry letters, 2012. **3**(7): p. 857-866.
4. Alvarez-Puebla, R.A. and L.M. Liz-Marzán, *SERS detection of small inorganic molecules and ions.* Angewandte Chemie International Edition, 2012. **51**(45): p. 11214-11223.
5. Fu, F. and Q. Wang, *Removal of heavy metal ions from wastewaters: a review.* Journal of environmental management, 2011. **92**(3): p. 407-418.
6. Finney, L.A. and T.V. O'Halloran, *Transition metal speciation in the cell: insights from the chemistry of metal ion receptors.* Science, 2003. **300**(5621): p. 931-936.
7. Halliwell, B. and J.M. Gutteridge, *[1] Role of free radicals and catalytic metal ions in human disease: an overview.* Methods in enzymology, 1990. **186**: p. 1-85.
8. Tsoutsi, D., et al., *Simultaneous SERS detection of copper and cobalt at ultratrace levels.* Nanoscale, 2013. **5**(13): p. 5841-5846.
9. Tsoutsi, D., et al., *Quantitative surface-enhanced Raman scattering ultradetection of atomic inorganic ions: the case of chloride.* Acs Nano, 2011. **5**(9): p. 7539-7546.
10. Pazos, E., et al., *Surface-enhanced Raman scattering surface selection rules for the proteomic liquid biopsy in real samples: efficient detection of the oncoprotein c-MYC.* Journal of the American Chemical Society, 2016. **138**(43): p. 14206-14209.
11. Lehrman, L., E.A. Kabat, and H. Weisberg, *Organic Reagents1 in Qualitative Analysis. I. The Separation of Iron, Chromium and Aluminum.* Journal of the American Chemical Society, 1933. **55**(9): p. 3509-3511.
12. Lehrman, L., H. Weisberg, and E.A. Kabat, *Organic Reagents1 in Qualitative Analysis. II. The Analysis of the Common Metals of the Ammonium Sulfide Group.* Journal of the American Chemical Society, 1934. **56**(9): p. 1836-1838.
13. Lehrman, L., M. Manes, and J. Kramer, *Organic Reagents1 in Qualitative Analysis. III. The Analysis of the Common Metals of the Alkaline Earth Group and Magnesium Using 8-Hydroxyquinoline.* Journal of the American Chemical Society, 1937. **59**(5): p. 941-942.
14. West, P.W., *Organic Reagents in Inorganic Analysis.* Analytical Chemistry, 1949. **21**(11): p. 1342-1344.
15. Guerrini, L. and R.A. Alvarez-Puebla, *Surface-enhanced Raman scattering sensing of transition metal ions in waters.* ACS omega, 2021. **6**(2): p. 1054-1063.
16. Furukawa, H., et al., *Ultrahigh porosity in metal-organic frameworks.* Science, 2010. **329**(5990): p. 424-428.
17. Stock, N. and S. Biswas, *Synthesis of metal-organic frameworks (MOFs): routes to various MOF topologies, morphologies, and composites.* Chemical reviews, 2012. **112**(2): p. 933-969.
18. He, L., et al., *Core–shell noble-metal@ metal-organic-framework nanoparticles with highly selective sensing property.* Angewandte Chemie International Edition, 2013. **52**(13): p. 3741-3745.
19. Zheng, G., et al., *Encapsulation of single plasmonic nanoparticles within ZIF-8 and SERS analysis of the MOF flexibility.* Small, 2016. **12**(29): p. 3935-3943.
20. Koh, C.S.L., et al., *Plasmonic nanoparticle-metal–organic framework (NP–MOF) nanohybrid platforms for emerging plasmonic applications.* ACS Materials Letters, 2021. **3**(5): p. 557-573.
21. Koh, C.S.L., et al., *Plasmonic nose: integrating the MOF-enabled molecular preconcentration effect with a plasmonic array for recognition of molecular-level volatile organic compounds.* Chemical Communications, 2018. **54**(20): p. 2546-2549.
22. Lee, H.K., et al., *Applying a nanoparticle@ MOF interface to activate an unconventional regioselectivity of an inert reaction at ambient conditions.* Journal of the American Chemical Society, 2020. **142**(26): p. 11521-11527.
23. Horcajada, P., et al., *Porous metal–organic-framework nanoscale carriers as a potential platform for drug delivery and imaging.* Nature materials, 2010. **9**(2): p. 172-178.
24. Carrillo-Carrión, C., et al., *Aqueous stable gold nanostar/ZIF-8 nanocomposites for light-triggered release of active cargo inside living cells.* Angewandte Chemie, 2019. **131**(21): p. 7152-7156.
25. Peralta, D., et al., *Comparison of the behavior of metal–organic frameworks and zeolites for hydrocarbon separations.* Journal of the American Chemical Society, 2012. **134**(19): p. 8115-8126.
26. Peralta, D., et al., *The separation of xylene isomers by ZIF-8: A demonstration of the extraordinary flexibility of the ZIF-8 framework.* Microporous and mesoporous materials, 2013. **173**: p. 1-5.
27. Qian, Q., et al., *MOF-based membranes for gas separations.* Chemical reviews, 2020. **120**(16): p. 8161-8266.
28. Nguyen, L.B.T., et al., *Inducing ring complexation for efficient capture and detection of small gaseous molecules using SERS for environmental surveillance.* Angewandte Chemie, 2022. **134**(33): p. e202207447.
29. Deng, X., et al., *Yolk–shell structured Au nanostar@ metal–organic framework for synergistic chemo-photothermal therapy in the second near-infrared window.* Nano Letters, 2019. **19**(10): p. 6772-6780.

30. Becerril-Castro, I.B., et al., *Gold Nanostars: Synthesis, Optical and SERS Analytical Properties.* Analysis & Sensing, 2022. **2**(3): p. e202200005.
31. Moffett, J.W., R.G. Zika, and R.G. Petasne, *Evaluation of bathocuproine for the spectro-photometric determination of copper (I) in copper redox studies with applications in studies of natural waters.* Analytica Chimica Acta, 1985. **175**: p. 171-179.
32. Pan, Y., et al., *Tuning the crystal morphology and size of zeolitic imidazolate framework-8 in aqueous solution by surfactants.* CrystEngComm, 2011. **13**(23): p. 6937-6940.
33. He, M., et al., *Facile synthesis of zeolitic imidazolate framework-8 from a concentrated aqueous solution.* Microporous and Mesoporous Materials, 2014. **184**: p. 55-60.
34. Zou, D., D. Liu, and J. Zhang, *From Zeolitic Imidazolate Framework-8 to Metal-Organic Frameworks (MOF s): Representative Substance for the General Study of Pioneering MOF Applications.* Energy & Environmental Materials, 2018. **1**(4): p. 209-220.
35. Qiao, X., et al., *Selective surface enhanced Raman scattering for quantitative detection of lung cancer biomarkers in superparticle@ MOF structure.* Advanced materials, 2018. **30**(5): p. 1702275.
36. Carron, K.T. and L.G. Hurley, *Axial and azimuthal angle determination with surface-enhanced Raman spectroscopy: thiophenol on copper, silver, and gold metal surfaces.* The Journal of Physical Chemistry, 1991. **95**(24): p. 9979-9984.
37. Álvarez-Puebla, R.A., et al., *Au@ pNIPAM colloids as molecular traps for surface-enhanced, spectroscopic, ultra-sensitive analysis.* Angewandte Chemie, 2009. **121**(1): p. 144-149.
38. Sayre, L.M. and G. Multhaup, *Alzheimer's precursor protein and the use of bathocuproine for determining reduction of copper (II).* Science, 1996. **274**(5294): p. 1933-1934.
39. Diehl, H. and G.F. Smith, *The copper reagents: cuproine, neocuproine, bathocuproine*. 1958: GF Smith Chemical Company.
40. Hobday, C.L., et al., *Understanding the adsorption process in ZIF-8 using high pressure crystallography and computational modelling.* Nature communications, 2018. **9**(1): p. 1429.
41. Song, Q., et al., *Zeolitic imidazolate framework (ZIF-8) based polymer nanocomposite membranes for gas separation.* Energy & Environmental Science, 2012. **5**(8): p. 8359-8369.
42. Park, K.S., et al., *Exceptional chemical and thermal stability of zeolitic imidazolate frameworks.* Proceedings of the National Academy of Sciences, 2006. **103**(27): p. 10186-10191.
43. Ueda, T., T. Yamatani, and M. Okumura, *Dynamic Gate Opening of ZIF-8 for Bulky Molecule Adsorption as Studied by Vapor Adsorption Measurements and Computational Approach.* The Journal of Physical Chemistry C, 2019. **123**(45): p. 27542-27553.
44. Zhang, K., et al., *Exploring the framework hydrophobicity and flexibility of ZIF-8: from biofuel recovery to hydrocarbon separations.* The Journal of Physical Chemistry Letters, 2013. **4**(21): p. 3618-3622.
45. Organization, W.H., *Guidelines for drinking-water quality: second addendum. Vol. 1, Recommendations*. 2008: World Health Organization.
46. Pazos-Perez, N., et al., *Modular assembly of plasmonic core–satellite structures as highly brilliant SERS-encoded nanoparticles.* Nanoscale Advances, 2019. **1**(1): p. 122-131.
47. De Abajo, F.G. and A. Howie, *Retarded field calculation of electron energy loss in inhomogeneous dielectrics.* Physical Review B, 2002. **65**(11): p. 115418.
48. Hohenester, U. and A. Trügler, *MNPBEM–A Matlab toolbox for the simulation of plasmonic nanoparticles.* Computer Physics Communications, 2012. **183**(2): p. 370-381.
49. !!! INVALID CITATION !!! {}.

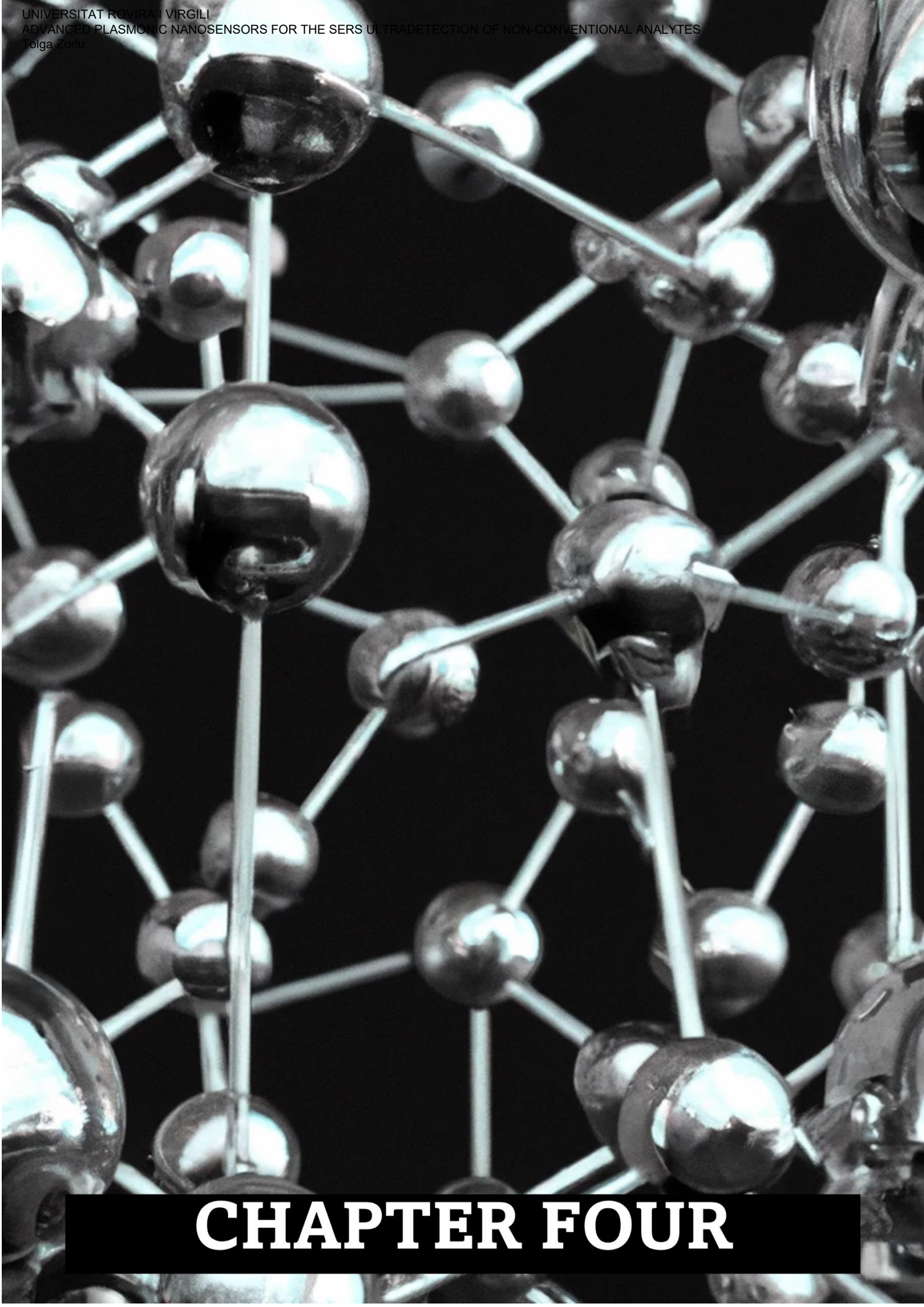

CHAPTER FOUR

General Conclusions

In general, this thesis enlightens us on the efficiency of innovative ZIF-based substrates that can be used for different SERS applications.

For this, first, yolk-shell NS@ZIF-8 particles with star-shaped gold nanoparticles at their heart were produced. At this stage, the production of hollow MOF particles is made possible, which is quite simple and does not require any organic solvent or acid treatment. In this way, the reshaping process, which is frequently encountered in synthesis stages and causes deterioration of anisotropic nanoparticle morphologies such as star-shaped, is also prevented. While obtaining yolk-shell materials, ZIF-8's sister structure, ZIF-67, was used as a sacrificial template. This is because ZIF-67 is highly unstable in water and easily hydrolyzed. On the other hand, since this is not the case for ZIF-8 produced within the scope of the thesis, the inner shell consisting of ZIF-67 surrounding the star-shape gold nanoparticles was removed with the help of water, and only ZIF-8, which formed the outer shell, remained stable. As a result of the experiments carried out, basically three different situations were observed: (1) the electromagnetic response of isolated Au NS even in concentrated solution or even cast on surface; (2) the homogeneous porous distribution characteristic of MOF materials; and (3) the availability of a large volume between the plasmonic core and the sieving shell that can be exploited for optical accumulation, catalysis, or drug storage. These materials are more colloidally stable than their counterparts without coating, can sieve different molecules based on their size or charge, seems to show some interesting synergy with gold for their application in photocatalysis and present strong optical activity to be used as SERS sensors. Further, the dependence of the SERS signal with time can be also used to design advanced analytical applications based in the adsorption time (kinetic control) or the stability (thermodynamic stability).

Secondly, novel hybrid SERS substrates were obtained by coating sub-micro polystyrene beads enriched with silver nanoparticles with ZIF-8. Here, the tightly packed silver nanoparticles on the polystyrene surface enable the material to produce highly intense electromagnetic hotspots. On the other hand, ZIF-8, which forms the shell, also allowed capturing of a metal chelating agent such as bathocuproine and load into the hybrid substrate.

Thus, bathocuproine-specific copper metal ions were easily detected at ultra-trace levels, and the novel substrate was shown to be a good alternative for in-direct SERS detection of metals.

In summary, this doctoral thesis contributes to the use of metal-organic frameworks in the field of plasmonics and thus to the advancement of novel SERS substrate designs. It also reveals that these designs show better SERS performances than bare plasmonic nanoparticles or uncoated plasmonic composites. Besides, it provides an innovative and easy experimental protocol for fabricating ZIF-8-based plasmonic yolk-shell materials. Finally, it shows that metal-chelating agents can be easily captured with the aid of a metal-organic framework shell, thus enabling metal ion detections in different environments.

Appendix I – List of Figures

background. On the other hand, yellow and red spectra indicate that SERS fingerprint of 1-NAT at time 0 and 1470 s, respectively

Appendix II – List of Tables

Appendix III – List of Publications

Zorlu, T., Guerrini, L., & Alvarez-Puebla, R. A. (2021). The sensing applications of metal-organic frameworks and their basic features affecting the fate of detection. In Metal-Organic Frameworks for Chemical Reactions (pp. 271-293). Elsevier.

Zorlu, T., Puértolas, B., Becerril-Castro, I. B., Giannini, V., Correa-Duarte, M. A., & Alvarez-Puebla, R. A. (2023). Optical Quantification of Metal Ions Using Plasmonic Nanostructured Microbeads Coated with Metal–Organic Frameworks and Ion-Selective Dyes. ACS Nanoscience Au.

UNIVERSITAT
ROVIRA i VIRGILI